POLITECNICO DI MILANO

Scuola di Ingegneria Industriale e dell'Informazione

Dipartimento di Fisica

STATISTICS OF PHOTON PENETRATION DEPTH IN A TWO-LAYER DIFFUSIVE MEDIUM

Dissertation of:

Michael Pascucci 838227

Supervisor: Prof. Alessandro Torricelli

Master of science degree in Engineering Physics

Track: Nanophysics and Nanotechnology

Academic year 2015-2016

Ringraziamenti

Al termine di questo lavoro di tesi desidero ringraziare tutte le persone che mi hanno aiutato in questi otto mesi.
In particolare desidero ringraziare il prof. Alessandro Torricelli per avermi offerto l'opportunità di lavorare a questo progetto e per aver reso questa esperienza molto costruttiva e piacevole.
Inoltre voglio ringraziare il proff. Lorenzo Spinelli per avermi aiutato nell'implementazione del metodo sviluppato in questa tesi dimostrandomi sempre una grande disponibilità. Un doveroso ringraziamento va anche al proff. Fabrizio Martelli che ha chiarito diversi miei dubbi aiutandomi nell'analisi dei dati. Ringrazio per l'attenzione rivoltami anche il prof. Antonio Pifferi e il prof. Andrea Farina.

Infine un'immensa gratitudine va ai miei genitori, per il sostegno e i consigli che hanno sempre saputo offrirmi e la libertà che mi hanno concesso in tutti questi anni. Molta parte del mio merito è vostra.

Abstract

The following dissertation examines the statistics of photon penetration depth in a two-layer diffusive medium.
The study starts from the presentation of the theories which describes light propagation through diffusive media and light penetration depth. In the homogeneous slab geometry, it is possible to obtain an analytical formula for the mean maximum depth reached by photons in a reflectance measure.
For the two-layer slab geometry a numerical method is developed for the calculation of photon penetration depth in both TD and CW domain. The method is also validated comparing the results with the analytical formulae for the homogeneous slab geometry.
Then, several simulations have been done using the method developed. Results give us a picture of the dependence of photon penetration depth on the parameters that characterize the two-layer slab geometry. Moreover, this study reveals some features which can be used to obtain a greater penetration depth of photons or an inspection of one specific layer. This knowledge may be useful for many research applications such as functional near infrared spectroscopy in order to improve the technique and the data analysis.
In the near future, the same approach can be also applied to a multilayer geometry.

Sommario

Nel seguente elaborato di laurea viene studiata la statistica della profondità di penetrazione dei fotoni all'interno di un mezzo diffondente formato da due strati.
La tesi inizia con una panoramica delle teorie che descrivono la propagazione della luce all'interno di mezzi diffondenti e la corrispondente profondità di penetrazione. Se si considera come geometria del problema una barra omogenea, sono disponibili formule analitiche per il calcolo della profondità massima media raggiunta dai fotoni in una misura di riflettanza.
Se, invece, si considera una geometria a due strati, non sono disponibili simili formule analitiche. Per questo motivo in questa tesi è stato sviluppato un metodo numerico per il calcolo della profondità di penetrazione dei fotoni nel dominio del tempo (TD) e in continua (CW). Il metodo è stato validato confrontando i risultati con la formula analitica relativa alla geometria della barra omogenea.
Successivamente sono state condotte numerose simulazioni numeriche utilizzando il metodo sviluppato e i risultati ottenuti evidenziano la dipendenza della profondità di penetrazione dai parametri che caratterizzano la barra a due strati. Inoltre, lo studio rivela che in determinate configurazioni è possibile ottenere ad esempio una maggiore profondità di penetrazione dei fotoni o è possibile sondare soltanto uno dei due strati. Tutto ciò può essere utilizzato per migliorare molte applicazioni biomediche come la spettroscopia nel vicino infrarosso.
Infine, lo stesso approccio numerico può essere applicato in futuro a una geometria formata da più di due strati.

Table of contents

Introduction **10**

Light propagation through biological tissues: principles and theory **14**
1.1 The radiative transport equation **15**
1.2 The diffusion approximation **17**
1.3 Solutions of the Diffusion Equation **19**
1.3.1 Slab geometry 19
1.3.2 Two-layer Cylinder geometry 22
Bibliography Chapter 1 ..... **25**

Penetration depth of photons **26**
2.1 Previous works on penetration depth **27**
2.2 Statistics of photon penetration depth **27**
2.2.1 Probability density function 27
2.2.2 Mean maximum depth 28
2.2.3 Mean average depth 29
2.3 Homogeneous slab in the diffusion approximation **30**
2.3.1 Expressions for f and $\langle z_{max} \rangle$ 30
2.3.2 Relevant examples for f and $\langle z_{max} \rangle$ 32
Bibliography Chapter 2 ..... **34**

Implementation and validation of a numerical method for the analysis of photon penetration depth in the bilayer geometry **36**
3.1 Implementation of the numerical method in TD **37**
3.1.1 Calculation of reflectance curves 38
3.1.2 Calculation of the probability density function 40
3.1.2 Calculation of the mean maximum penetration depth 40
3.2 Validation of the numerical method in TD **40**
3.3 Implementation of the numerical method in CW domain **42**
3.4 Validation of the numerical method in CW domain **43**
Bibliography Chapter 3 ..... **46**

Bilayer geometry simulations in TD **47**
4.1 Simulations varying the absorption coefficient **48**
4.1.1 Variation of μ_{a1} 49
4.1.2 Variation of μ_{a2} 50
4.1.3 Extreme cases 52
4.2 Simulations varying the reduced scattering coefficient **54**
4.2.1 Variation of μ'_{s1} 55
4.2.2 Variation of μ'_{s2} 56
4.2.3 Extreme cases 58
4.3 Simulations varying the interfiber distance **59**
4.4 Simulations varying the thicknesses **60**
4.4.1 Simulations with reduced scattering coefficient mismatch 60
4.4.1 Simulations with absorption coefficient mismatch 64
4.5 Simulations varying the refractive indexes **67**
4.5.1 Simulations with small refractive index mismatch 68
4.5.2 Simulations with large refractive index mismatch 69
Bibliography Chapter 4 ..... **71**

Bilayer geometry simulations in CW 72
5.1 Simulations varying the absorption coefficient 73
5.1.1 Variation of μ_{a1} 74
5.1.2 Variation of μ_{a2} 75
5.1.3 Extreme cases 76
5.2 Simulations varying the reduced scattering coefficient 77
5.2.1 Variation of μ'_{s1} 78
5.2.2 Variation of μ'_{s2} 79
5.2.3 Variation of μ'_{s1} with μ_a=0.15 cm^{-1} 81
5.2.4 Variation of μ'_{s2} with μ_a=0.15 cm^{-1} 82
5.2.5 Extreme cases 84
5.3 Conclusions 85
Bibliography Chapter 5 87

Table of figures

Fig. 1.1: Relationship between the power *dP* and the radiance *I*.....15
Fig. 1.2: Physical meaning of terms in Eq. 1.2 representing the balance of energy.....16
Fig. 1.3: Slab geometry and model of image sources.....19
Fig. 1.4: Examples of TD reflectance curves for a slab.....21
Fig. 1.5: Examples of CW reflectance curves for a slab.....22
Fig. 1.6: Graphic of two-layer cylinder geometry with symbols.....22
Fig. 1.7: Examples of reflectance curves for a two-layer cylinder.....24
Fig. 2.1: Schematic for a 2D projection of a detected photon trajectory from a diffusive slab.....27
Fig. 2.2: Probability density functions f versus depth z, calculated exploiting DE for a homogeneous slab.....33
Fig. 2.3: $\langle z_{max} \mid t \rangle$ versus time and $\langle z_{max} \mid \rho \rangle$ versus ρ for a homogeneous slab.....33
Fig. 3.1: Section of a bilayer slab.....37
Fig. 3.2: Block diagram of the method used.....38
Fig. 3.3: Sections of a given bilayer slab.....39
Fig. 3.4: Graphic of two-layer cylinder geometry with symbols.....39
Fig. 3.5: $\langle z_{max} \mid t \rangle$ and $f(z \mid t)$ for a homogeneous slab of thickness 20 mm.....41
Fig. 3.6: $\langle z_{max} \mid t \rangle$ and $f(z \mid t)$ for a homogeneous slab of thickness 40 mm.....41
Fig. 3.7: Reflectance curves calculated with improved solution or with Fick's law solution for a homogeneous slab of thickness 20 mm.....43
Fig. 3.8: $f(z \mid \rho)$ and $\langle z_{max} \mid \rho \rangle$ for a homogeneous slab of thickness 20 mm.....44
Fig. 3.9: $f(z \mid \rho)$ and $\langle z_{max} \mid \rho \rangle$ for a homogeneous slab of thickness 40 mm.....45
Fig. 4.1: Two possible photon path inside a homogeneous slab of thickness s0.....48
Fig. 4.2: Bilayer geometry used in the simulations.....49
Fig. 4.3: $\langle z_{max} \mid t \rangle$ for different values of μ_{a1}.....49
Fig. 4.4: $f(z|t)$ relative to different μ_{a1} are reported as a function of z.....50
Fig. 4.5: $\langle z_{max} \mid t \rangle$ and $f(z|t)$ for different values of μ_{a2}. μ_{a1} is fixed at 0.15 cm^{-1}.....51
Fig. 4.6: Two possible photon path inside a bilayer slab of thickness s_0.....52
Fig. 4.7: $f(z|t)$ and $\langle z_{max} \mid t \rangle$ calculated in the two extreme situation.....53
Fig. 4.8: $\langle z_{max} \mid t \rangle$ and $f(z|t)$ for a homogeneous slab of thickness 40 mm.....54
Fig. 4.9: Two homogeneous slabs with reduced scattering coefficient $\mu'_{s,i}$ and $\mu'_{s,j}$ are displayed together with two possible photon path inside them.....55
Fig. 4.10: Bilayer geometry used in the simulations.....55
Fig. 4.11: $f(z|t)$ and $\langle z_{max} \mid t \rangle$ are reported for different values of μ'_{s1}.....56

Fig. 4.12: $f(z|t)$ and $\langle z_{max} | t \rangle$ are reported for different values of μ'_{s2}.....57
Fig. 4.13: $f(z|t)$ calculated for μ'_{s2}=10 cm^{-1}, μ'_{s2}=100 cm^{-1} and μ'_{s2}=1000 cm^{-1} while μ'_{s1} is fixed to 10 cm^{-1}.....58
Fig. 4.14: $\langle z_{max} | t \rangle$ calculated for μ'_{s2}=10 cm^{-1}, μ'_{s2}=100 cm^{-1} and μ'_{s2}=1000 cm^{-1}, with μ'_{s1}=10 cm^{-1}..58
Fig. 4.15: Bilayer geometry used in the simulations.....59
Fig. 4.16: $f(z|t)$ for the considered geometry (Fig.4.15) with ρ=10 mm, ρ =20 mm and ρ =30 mm.....59
Fig. 4.17: $\langle z_{max} | t \rangle$ for the considered geometry (Fig.4.15) with ρ=10 mm, ρ =20 mm and ρ =30 mm.....60
Fig. 4.18: Bilayer geometry used in the simulations.....61
Fig. 4.19: $f(z|t)$ and $\langle z_{max} | t \rangle$ are reported for different values of s_1 with μ'_{s1}=5 cm^{-1}, μ'_{s2}=10 cm^{-1} and μ_{a1}=μ_{a2}=0.10 cm^{-1} 62
Fig. 4.20: $f(z|t)$ and $\langle z_{max} | t \rangle$ are reported for different values of s_1, with μ'_{s1}=10 cm^{-1}, μ'_{s2}=5 cm^{-1} and μ_{a1}=μ_{a2}=0.10 cm^{-1} 63
Fig. 4.21: Bilayer geometry used in the simulations.....64
Fig. 4.22: $f(z|t)$ and $\langle z_{max} | t \rangle$ are reported for different values of s_1, with μ_{a1}=0.1 cm^{-1} μ_{a2}=0.2 cm^{-1} and μ'_{s1}=μ'_{s2}=10 cm^{-1} 64
Fig. 4.23: Time-dependent mean partial pathlength are reported for layer 1 (L_1) and layer 2 (L_2).....65
Fig. 4.24: $f(z|t)$ and $\langle z_{max} | t \rangle$ are reported for different values of s_1, with μ_{a1}=0.2 cm^{-1}, μ_{a2}=0.1 cm^{-1} and μ'_{s1}=μ'_{s2}=10 cm^{-1} 66
Fig. 4.25: Time-dependent mean partial pathlength are reported for layer 1 (L_1) and layer 2 (L_2).....66
Fig. 4.26: Time-dependent mean partial pathlength of layer 1 are reported for s_1=5 mm, s_1=10 mm and s_1=15 mm.....67
Fig. 4.27: Bilayer geometry used in the simulations.....67
Fig. 4.28: $f(z|t)$ and $\langle z_{max} | t \rangle$ calculated for the bilayer slab geometry of Fig. 4.27 with n_2=1.40.....68
Fig. 4.29: $f(z|t)$ and $\langle z_{max} | t \rangle$ calculated for the bilayer slab geometry of Fig. 4.27 with n_1=1.40.....68
Fig. 4.30: $f(z|t)$ calculated for the bilayer slab geometry of Fig. 4.27 with high refractive index mismatch.....69
Fig. 4.31: $\langle z_{max} | t \rangle$ calculated for the bilayer slab geometry of Fig. 4.27 with high refractive index mismatch.....69
Fig. 5.1: $f(z|\rho)$ and $\langle z_{max} | \rho \rangle$ calculated for a homogeneous slab of thickness 40 mm.....73
Fig. 5.2: Bilayer geometry used in the simulations.....73
Fig. 5.3: $f(z|\rho)$ and $\langle z_{max} | \rho \rangle$ are reported for different values of μ_{a1}, μ_{a2} is fixed at 0.15 cm^{-1}.....74
Fig. 5.4: $f(z|\rho)$ and $\langle z_{max} | \rho \rangle$ are reported for different values of μ_{a2}, μ_{a1} is fixed at 0.15 cm^{-1}.....75
Fig. 5.5: $f(z|\rho)$ and $\langle z_{max} | \rho \rangle$ calculated in the two extreme situation.....76
Fig. 5.6: $f(z|\rho)$ and $\langle z_{max} | \rho \rangle$ calculated in the case with μ_{a1}=1 cm^{-1} and μ_{a2}=0 cm^{-1}.....77

Fig. 5.7: $f(z|\rho)$ and $\langle z_{max}|\rho\rangle$ calculated for a homogeneous slab of thickness 40 mm, $n_{int}=n_{out}=1.4$, $\mu_a=0$ cm^{-1} 77
Fig. 5.8: Bilayer geometry used in the simulations 78
Fig. 5.9: $\langle z_{max}|\rho\rangle$ are reported for different values of μ'_{s1} 78
Fig. 5.10: $f(z|\rho)$ reported for different values of μ'_{s1}, $\mu'_{s2}=10$ cm^{-1} 79
Fig. 5.11: $f(z|\rho)$ reported for different values of μ'_{s2}, $\mu'_{s1}=10$ cm^{-1} 80
Fig. 5.12: $\langle z_{max}|\rho\rangle$ are reported for different values of μ'_{s1} 81
Fig. 5.13: $\langle z_{max}|\rho\rangle$ are reported for different values of μ'_{s1}, $\mu'_{s2}=10$ cm^{-1}. In panel a) $\mu_{a1}=\mu_{a2}=0.15$ cm^{-1} while in panel b) $\mu_{a1}=\mu_{a2}=0$ cm^{-1} 81
Fig.5.14: $f(z|\rho)$ reported for different values of μ'_{s1}, $\mu'_{s2}=10$ cm^{-1}, $\mu_{a1}=\mu_{a2}=0.15$ cm^{-1} 82
Fig. 5.15: $f(z|\rho)$ reported for different values of μ'_{s2}, $\mu'_{s1}=10$ cm^{-1}, $\mu_{a1}=\mu_{a2}=0.15$ cm^{-1} 83
Fig. 5.16: $\langle z_{max}|\rho\rangle$ are reported for different values of μ'_{s2}, $\mu'_{s1}=10$ cm^{-1}. In panel a) $\mu_{a1}=\mu_{a2}=0.15$ cm^{-1} while in panel b) $\mu_{a1}=\mu_{a2}=0$ cm^{-1} 84
Fig. 5.17: $f(z|\rho)$ calculated for $\mu'_{s2}=10$ cm^{-1}, $\mu'_{s2}=100$ cm^{-1} and $\mu'_{s2}=1000$ cm^{-1}, μ'_{s1} is fixed to 10 cm^{-1} 84
Fig. 5.18: $\langle z_{max}|\rho\rangle$ calculated for $\mu'_{s2}=10$ cm^{-1}, $\mu'_{s2}=100$ cm^{-1} and $\mu'_{s2}=1000$ cm^{-1}, μ'_{s1} is fixed to 10 cm^{-1} 85

Introduction

Photon migration through diffusive media looks like a random walk (zigzag trajectory). This occurs because photons undergo a sufficiently high number of scattering events that their trajectories become randomized. The study of light propagation through diffusive media is very interesting in many fields since there is a huge list of highly scattering media common in daily life (e.g., biological tissues, agricultural products, wood, paper, plastic materials and milk) [1].

Light propagation through turbid media can be accurately described with the radiative transport equation (RTE), i.e., an integro-differential equation which represents the balance of energy for light propagation through a volume element dV of an absorbing and scattering medium [1, 2]. Since no general analytical (closed-form) solutions for the RTE are available, simpler models are usually employed. When propagation is dominated by multiple scattering (strongly diffusive media), the most widely used model is based on the diffusion approximation. Using this approximation, it is possible to obtain a simpler equation, i.e., the diffusion equation (DE) for which analytical solutions are available in many geometries, but it is necessary to stress that these solutions are approximate.

In many research fields light is employed as a tool to extract information on what is below the surface of a diffusive medium. Usually, the medium is addressed in reflectance geometry, where light, injected and collected from the same side of its external surface, carries information on the medium optical properties encoded along photons random paths. One possible application is Neurophotonics. In particular, functional near infrared spectroscopy (fNIRS) uses red and near infrared light (e.g. 600-900 nm) to noninvasively investigate brain structures and brain functions. Indeed, it allows the estimate of the typical hemodynamic parameters from the optical properties of a biological tissue. The two most used fNIRS modalities are continuous wave (CW) and time-domain (TD). In the former light with a constant intensity is injected into the tissue. In the latter pulses of light (hundreds of picoseconds) are injected into the medium, and after travelling inside it, are recollected. Information about photon penetration depth is crucial in both these modalities since a key challenge is the extraction of specific brain-cortex signals out of the superficial contamination generated by scalp, skull and cerebrospinal fluid. Depth information is important also for other emerging applications such as cancer screening in thyroid or prostate, or for non-clinical fields, such as internal quality assessment of agricultural produce, non-destructive monitoring of wood materials, or for pharmaceuticals and highly scattering plastics [3]. For these reasons, the study of photon penetration depth in diffusive

media is really interesting and it can play an active role in the improvement of these applications.

Photon penetration depth in random media has been studied by many research groups. The quantity of interest are the mean average depth $\langle \bar{z} \rangle$ or the mean maximum depth $\langle z_{max} \rangle$ reached by photons detected at the surface of the medium. The first works on this subject used a simple random walk model of light propagation to provide expressions for the continuous wave (CW) probability density of $\langle z_{max} \rangle$ for photons that emerge at a distance ρ from the injection point of light [4, 5]. A recent work on this subject is written by Martelli et al. [3] and gives a general description of the statistics behind the penetration depth of light in a turbid medium within the framework of the RTE for both TD and CW domain. In the work by Martelli et al. analytical formulae of the penetration depth have been presented in the case of a homogeneous slab geometry that is often used as a model for biological tissues neglecting their inhomogeneities.

Layered model geometries are also employed in tissue optics, motivated by the fact that some biological tissues have a layered architecture. This is the case of muscle underneath a superficial fat layer or of the head with compartments such as scalp, skull, and brain. Thus, the study of photon penetration depth in these layered geometries can be very interesting for biomedical applications such as fNIRS. Since until now no paper takes into account the case of multilayer geometry, the aim of the following work is to study the statistics of photon penetration depth in the bilayer geometry.

Thus, in this thesis work a numerical method is developed to calculate the mean maximum penetration depth for the bilayer slab geometry. The method is made up of three stages. The first stage consists in the numerical evaluation of reflectance curves which are used in the second stage to calculate the probability density function, $f(z)$, i.e., the probability density for the maximum depth reached by photons detected. In the last stage the mean maximum penetration depth is numerically evaluated. The method is implemented in both TD and CW domain and then it is validated comparing the results with the analytical formulae for the homogeneous slab geometry.

Then, several simulations have been done using the method developed. We tested many different configurations of bilayer slab geometry in order to make a picture of the dependence of the mean maximum penetration depth on the physical parameters that characterize a bilayer slab in both TD and CW domain. Results prove that in many cases the behavior of the mean maximum penetration depth is quite different from that in case of homogeneous slab geometry.

In TD an absorption coefficient mismatch between the two layers significantly changes the statistics of photon penetration depth with respect to the homogeneous case. It turns out that the mean maximum penetration depth increases if the absorption coefficient of the deeper layer is lower than that of the superficial layer. Indeed, photons which travel a longer distance inside the less absorbing layer have a higher probability of being detected. This can be very interesting for applications. For example, in a multilayer geometry the inspection of one specific layer can be done by inducing a much greater absorption coefficient on the others. Besides, a reduced scattering coefficients mismatch affects the statistics as well. In particular, when the reduced scattering coefficient of the first layer

changes, the effect on $\langle z_{max} \rangle$ is large. For low values of the reduced scattering coefficient, $\langle z_{max} \rangle$ increases since photons are more likely to reach a greater depth. On the other hand, for high values of the reduced scattering coefficient, $\langle z_{max} \rangle$ decreases. Furthermore, the interfiber distance does not affect the mean maximum penetration depth as in the homogeneous case. Moreover, since biological tissue layers do not have a fixed thickness, we have also studied the effects induced by changing the thicknesses of the first and the second layer. The effects are significant when there is a reduced scattering coefficient mismatch or an absorption coefficient mismatch between the layers. Finally, we have shown that a refractive index mismatch in the typical range for biological tissues does not change the statistics of photon penetration depth.
In CW the results are quite different from TD. The absorption coefficient significantly affects the statistics. The effect of a variation of μ_{a1} is large since each photon detected has to pass through the first layer. On the other hand, a variation of reduced scattering coefficients significantly influences photon penetration depth only in the case with an absorption coefficient different from zero. In the ideal case with μ_a=0 cm^{-1}, no significant differences are obtained. This means that interaction between absorption and scattering coefficients plays an important role in the statistics of photon penetration depth in CW domain.
In the future it can be interesting to study in a more detailed way the interplay between absorption and scattering coefficient in both TD and CW domain in particular focusing on specific realistic case (e.g. neonate's head). Moreover, a numerical method for a multilayer geometry can be developed in order to better analyze biological media with more than two layers.

In Chapter 1 of this thesis a review is presented of the theories and the formulae based on the DE that have been widely used for biomedical applications. Thus, the RTE and the DE are described and DE solutions are presented for the homogeneous slab and for the bilayer slab geometry.
In Chapter 2 the general formulation of the penetration depth statistics is presented following the method developed in previous literature on this subject. Then, the analytical formulae of photon penetration depth are reported for homogeneous slab geometry.
In Chapter 3 a methodology is presented to obtain in a numerical way the mean maximum penetration depth in the case of bilayer slab geometry. The first part of the chapter is dedicated to the implementation and validation of the method used for TD measures, while the second part is dedicated to the CW domain.
In Chapter 4 some numerical simulations are done using the method developed and validated in Chapter 3 for TD. The chapter is divided into five sections which describe the dependence of the TD photon penetration depth on each parameter of interest, i.e., absorption coefficient, reduced scattering coefficient, interfiber distance, thickness and refractive index.
In Chapter 5 numerical simulations are done using the method developed and validated in Chapter 3 for CW domain. The chapter is divided into two sections which describe the dependence of the CW photon penetration depth on absorption coefficient and reduced scattering coefficient.

Bibliography Introduction

[1] F.Martelli, S. Del Bianco, A. Ismaelli, G. Zaccanti, "Light propagation through biological tissue and other diffusive media", SPIE, Bellingham (2010).

[2] A. Ishimaru, Wave Propagation and Scattering in Random Media, Vol. 1, Academic Press, New York (1978).

[3] F. Martelli, T. Binzoni, A. Pifferi, L. Spinelli, A. Farina, and A.Torricelli, "There's plenty of light at the bottom: statistics of photon penetration depth in random media", Scientific Reports 6:27057 (2016).

[4] R.F.Bonner, R.Nossal, S.Havlin, and G.H.Weiss, "Model for photon migration in turbid biological media,"J.Opt.Soc. Am. A 4, 423-432 (1987).

[5] G. Weiss, "Statistical Properties of the Penetration of Photons into a Semi-Infinite Turbid Medium: A Random-Walk Analysis," Appl. Opt. 37, 3558-3563 (1998).

CHAPTER 1

Light propagation through biological tissues: principles and theory

The interaction between light and biological tissues is a complex matter because of the really heterogeneous composition of the latter. The two main interactions which affect light propagation through a tissue are absorption and scattering. In a broad range of wavelengths, from red to infrared, the main biological tissue components (e.g. hemoglobin, lipid, water...) are little absorbing and light propagation is characterized by a diffusive regime. This means that the propagation is dominated by multiple scattering events causing the medium to appear turbid. For this reasons biological tissues are considered diffusive media. As noted by Ishimaru [1], there are two ways to deal with multiple-scattering propagation. The former is the analytical theory or multiple-scattering theory and is based on Maxwell's equations. This theory is mathematically rigorous but also really complex and so it has not yet produced practical models of general use. The latter is the radiative transport theory which is a phenomenological and heuristic theory describing the transport of energy through a scattering medium and it is the most widely used approach. Even though this theory does not rigorously represent the real physics of light propagation, it permits the derivation of useful models for many practical problems [1]. This approach will be presented in this chapter.

1.1 The radiative transport equation

The basis of the radiative transport equation (RTE) is to evaluate energy transportation due to photon propagation neglecting the wave nature of light. Indeed, the RTE is an integro-differential equation which represents the balance of energy for light propagation through a volume element *dV* of an absorbing and scattering medium [1, 2]. One of the basic quantities used to describe energy propagation is radiance $I(\vec{r}, \hat{s}, t)$, i.e., the average power that at position $\vec{r}$ and time t flows through the unit area oriented in the direction of the unit vector $\hat{s}$, due to photons moving within the unit solid angle around $\hat{s}$. With Eq. 1.1 it is possible to relate radiance with the power *dP* that at time t flows within the solid angle $d\Omega$ through the elementary area $d\Sigma$, oriented along the direction $\hat{n}$ and placed at $\vec{r}$ (Fig. 1.1):

$$dP = I(\vec{r}, \hat{s}, t)\, |\hat{n} \cdot \hat{s}| d\Sigma d\Omega \tag{1.1}$$

Thus radiance $I(\vec{r}, \hat{s}, t)$ is proportional to the number of photons in the unit volume that at time t are moving along the direction $\hat{s}$.

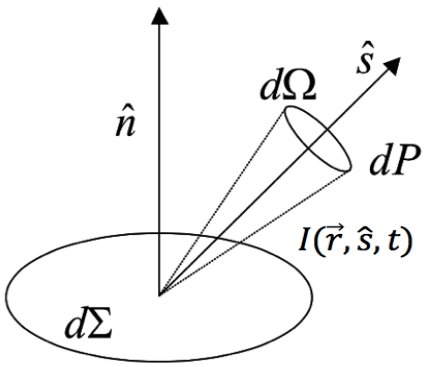

Figure 1.1: Relationship between the power dP and the radiance I.

Since total energy must be conserved, the RTE can be obtained by balancing the different mechanisms by which the radiance, $I(\vec{r}, \hat{s}, t)$, can increase or decrease inside the volume element *dV*. In the general case of time-dependent sources, the RTE can be written as [2]:

$$\frac{1}{v}\frac{\partial I(\vec{r}, \hat{s}, t)}{\partial t} = -\nabla \cdot [\hat{s} I(\vec{r}, \hat{s}, t)] - \mu_a\, I(\vec{r}, \hat{s}, t) - \mu_s\, I(\vec{r}, \hat{s}, t) + \mu_s \int_{4\pi} p(\hat{s}, \widehat{s'})\, I(\vec{r}, \widehat{s'}, t)\, d\Omega' + \varepsilon(\vec{r}, \hat{s}, t)\,, \tag{1.2}$$

where *v* is the light speed inside the medium, $\varepsilon(\vec{r}, \hat{s}, t)$ is the source term i.e. the power emitted at time t per unit volume and unit solid angle along $\hat{s}$, and $d\Omega'$ is the elementary solid angle in the direction $\widehat{s'}$. Considering the volume element *dV* identified by the position vector $\vec{r}$, the term on the left side of Eq. 1.2 represents the following:

- $\frac{1}{v}\frac{\partial I(\vec{r},\hat{s},t)}{\partial t} dV d\Omega dt$ is the total temporal change of energy that is propagating along $\hat{s}$ within dV, $d\Omega$ and dt.

On the right side of the Eq. 1.2, the terms are described respectively as follow:

1. $-\nabla \cdot [\hat{s} I(\vec{r},\hat{s},t)]\, dV d\Omega dt$ represents the net flux of energy that is propagating along $\hat{s}$ through the volume dV , within $d\Omega$, and dt;

2. $-\mu_a\, I(\vec{r},\hat{s},t)$ is the fraction of energy that is propagating along $\hat{s}$ within dV, $d\Omega$ and dt lost for absorption events;

3. $-\mu_s\, I(\vec{r},\hat{s},t)$ is the fraction of energy that is propagating along $\hat{s}$ within dV, $d\Omega$ and dt lost for scattering events;

4. $\mu_s \int_{4\pi} p(\hat{s},\widehat{s'})\, I(\vec{r},\widehat{s'},t)\, d\Omega' dV d\Omega dt$ represents the energy coming from any direction $\widehat{s'}$ that, within dV, $d\Omega$ and dt, is scattered in direction $\hat{s}$;

5. $\varepsilon(\vec{r},\hat{s},t) dV d\Omega dt$ represents the energy generated along $\hat{s}$ in $d\Omega$ and dt by sources inside dV.

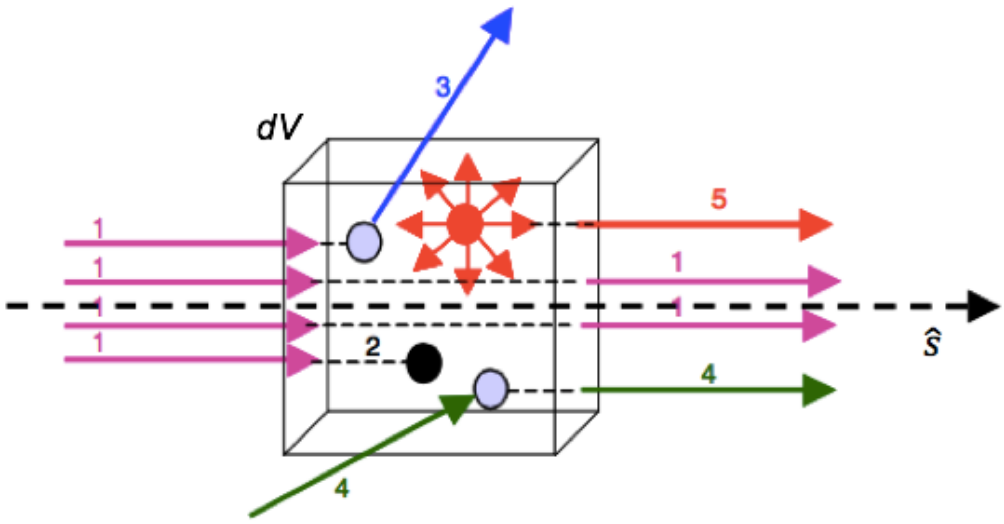

Figure 1.2: Physical meaning of terms in Eq. 1.2 representing the balance of energy.

In Fig. 1.2 a graphical explanation of all RTE terms is given.
As already said, this method lacks a rigorous mathematical formulation able to account for all the physical effects involved in light propagation. Indeed, phenomena as interference and polarization status of photons are neglected.
The RTE is an integro-differential equation and the retrieval of solutions is an extremely expensive computational process, in terms of time and resources. Its solutions are usually based on numerical methods like the finite element method [3] or the discrete ordinates

method [4, 5]. Among the numerical procedures there are also stochastic methods like MonteCarlo method [3].

1.2 The diffusion approximation

Since no general analytical (closed-form) solutions for RTE are available, simpler models are usually employed. When propagation is dominated by multiple scattering (strongly diffusive media), the most widely used model is based on the diffusion approximation [2, 6]. In the general case of time-dependent sources it consists of two simplifying assumptions shown below.

1. The radiance is considered almost isotropic and can be approximated by the first two terms (isotropic and linearly anisotropic terms) of a series expansion in spherical harmonics [1, 2]:

$$I(\vec{r},\hat{s},t) = \frac{1}{4\pi}\Phi(\vec{r},t) + \frac{3}{4\pi}\vec{J}(\vec{r},t)\cdot\hat{s} \tag{1.3}$$

   where $\Phi(\vec{r},t)$ is the fluence rate and it is obtained integrating the radiance over the entire solid angle while $\vec{J}(\vec{r},t)$ is the flux vector which represents the amount and the direction of the net flux of power. Eq. 1.3 is a good approximation for the radiance if the contribution of the higher-order spherical harmonics is negligible. This is usually true if the second term of the expansion is small with respect to the first, i.e., $\Phi(\vec{r},t) \gg 3\vec{J}(\vec{r},t)\cdot\hat{s}$.

2. Time variation of the diffusive flux vector $\vec{J}(\vec{r},t)$ over a time range $\Delta t = 1/(v\mu_s')$ is negligible with respect to the vector itself and can be expressed as [2]:

$$\frac{1}{v\mu_s'}\left|\frac{\partial\vec{J}(\vec{r},t)}{\partial t}\right| \ll \left|\vec{J}(\vec{r},t)\right| \tag{1.4}$$

   where $\mu_s' = \mu_s(1-g)$ is the reduced scattering coefficient (g is the anisotropy factor for the scattering function).

In general, Eq. 1.3 and Eq. 1.4 are well fulfilled when photons have undergone many scattering events, since scattering tends to randomize the direction of light propagation. Conversely, absorption obstructs the diffusive regime since in a strongly absorbing medium only photons that undergo few scattering events will not be absorbed. Therefore, the diffusive regime of light propagation can be established when scattering effects are predominant in absorption ($\mu_s' \gg \mu_a$).
In order to obtain the diffusion equation, the RTE is integrated over all directions and the continuity equation is found [2]:

$$\frac{\partial}{v\partial t}\Phi(\vec{r},t) + \nabla\cdot\vec{J}(\vec{r},t) + \mu_t\Phi(\vec{r},t) = \int_{4\pi}\varepsilon(\vec{r},\hat{s},t)d\Omega \qquad (1.5)$$

where $\mu_t = \mu_s + \mu_a$.
Then expressing the flux vector as a function of the fluence rate and making use of the simplifying conditions, Fick's law is obtained [2]:

$$\vec{J}(\vec{r},t) = -D\left[\nabla\Phi(\vec{r},t) - 3\int_{4\pi}\varepsilon(\vec{r},\hat{s},t)\,\hat{s}d\Omega\right], \qquad (1.6)$$

where D = 1 / ($3\mu_s'$) due to the scaling property of the RTE [2].
If the medium has no sources or the sources are isotropic, Fick's law becomes [3]

$$\vec{J}(\vec{r},t) = -D\nabla\Phi(\vec{r},t) \qquad (1.7)$$

The physical meaning of the Fick's law is that photons tend to migrate toward those regions of the medium where the photon density is smaller. Substituting Eq. 1.6 in Eq.1.5, the time-dependent diffusion equation (DE) is obtained [2]:

$$\left[\frac{\partial}{v\partial t} - D\nabla^2 + \mu_a\right]\Phi(\vec{r},t) = q_0(\vec{r},t) \qquad (1.8)$$

where

$$q_0(\vec{r},t) = \int_{4\pi}\varepsilon(\vec{r},\hat{s},t)d\Omega - 3\nabla\cdot\left[D\int_{4\pi}\varepsilon(\vec{r},\hat{s},t)\hat{s}d\Omega\right] \qquad (1.9)$$

It must be noted that DE is a partial-differential equation for the fluence rate and several analytical solutions are available. Furthermore, Eq. 1.8 shows that photon migration in the diffusive regime is fully described by the knowledge of the absorption coefficient and of the reduced scattering coefficient.
The DE is a partial-differential equation, and any general solution will contain unknown constants that need to be determined by using proper boundary conditions originated from the physics of the problem investigated. In the following paragraph, some solutions for geometries of interest will be presented.

1.3 Solutions of the Diffusion Equation

1.3.1 Slab geometry

The first geometry we are interested in is the slab geometry since many physical problems are likely to be represented in this way [1, 7]. The geometry is shown in Fig. 1.3. In order to obtain the solutions for this geometry we follow the method of images (or mirror images) [8]. The method makes use of the extrapolated boundary conditions (EBC) [9, 10] that assume the fluence equal to zero on the extrapolated surface at distance $z_e = 2AD$ from the physical boundary (where A is a term that take into account the refractive index mismatch on the media interfaces). The method of images allows us to reconstruct the solution for the fluence inside the medium as a superposition of solutions for the infinite medium.

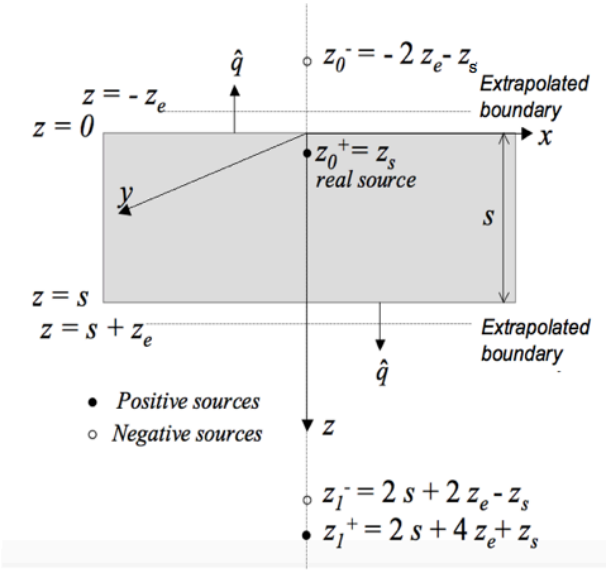

Figure 1.3: Slab geometry and model of image sources.

In our scheme a narrow collimated pulsed light beam (pencil beam) is incident upon the surface of a diffusing slab. Assuming that all incident photons are initially scattered (isotropically) at a depth $z_s=1/\mu'_s$ below the surface, the pulse is supposed to be mathematically described by an isotropic point source of unitary strength, i.e., a spatial and temporal Dirac delta source located at $z=z_s$ into the medium [10]. Applying the method of images, the correct boundary conditions (EBC) are obtained by using, in addition to the source in z_0, an infinite number of pairs of positive and negative sources in an infinite diffusive medium having the same optical properties of the slab. The positive and negative sources are placed at [2, 10]:

$$\begin{cases} z_m^+ = 2m(s + 2z_e) + z_s \\ z_m^- = 2m(s + 2z_e) - 2z_e - z_s \\ m = 0, \pm 1, \pm 2, \ldots\ldots \pm \infty . \end{cases} \tag{1.10}$$

By applying Fick's law (Eq. 1.7) at the boundary of the medium it is possible to obtain the flux exiting the diffusive medium from the upside, i.e., the TD reflectance of a slab of thickness s [2, 10]:

$$R(\rho,t) = -\frac{\exp\left(-\frac{\rho^2}{4Dvt}-\mu_a vt\right)}{2(4\pi Dv)^{3/2}t^{5/2}} \times \sum_{m=-\infty}^{m=+\infty}\left[z_{3m}\exp\left(-\frac{z_{3m}^2}{4Dvt}\right) - z_{4m}\exp\left(-\frac{z_{4m}^2}{4Dvt}\right)\right], \tag{1.11}$$

where:

$$\begin{aligned} z_{3m} &= -2ms - 4mz_e - z_e \\ z_{4m} &= -2ms - (4m-2)z_e + z_s \end{aligned} \tag{1.12}$$

with $\rho = \sqrt{x^2+y^2}$ (interfiber distance).

Reflectance curve represents the power crossing the surface per unit area and at a certain interfiber distance ρ. It can also represent the probability that a photon, entering in the medium at the origin of the coordinate system, exits after a time t and at a distance ρ from the incident point, per unit time and area [10]. Eq. 1.11 is an infinite series and should be truncated for practical applications.

It is important to stress that Eq. 1.11 also predict energy for $t < t_0 = \rho/v$, which is the ballistic time necessary to propagate from the source to the receiver, following a straight path. Therefore, the simplifying assumptions necessary to obtain the DE imply an infinite speed for the propagation of energy so that a local variation in photon density instantaneously spreads over the medium. This aspect of the DE is physically incorrect since it violates the causality principle. The violation of this principle also originates from the requirement that the two assumptions of the DE are instantaneously valid after the light source is injected inside the medium, whilst they actually become valid only after a detected photon has undergone several scattering events. In fact, the diffusion approximation correctly describes the asymptotical behavior of light propagation, i.e., when the elapsed time is much longer than the ballistic time [2].

Solutions of the DE in case of steady-state source (CW) are obtained by integrating Eq. 1.11 over time [2]:

$$\begin{aligned} R(\rho) &= \int_0^{+\infty} R(\rho,t)dt \\ &= -\frac{1}{4\pi}\sum_{m=-\infty}^{m=+\infty}\left(z_{3m}\left(\rho^2+z_{3m}^2\right)^{-3/2} \times \left\{1+\left[\frac{\mu_a\left(\rho^2+z_{3m}^2\right)}{D}\right]^{1/2}\right\}\right. \\ &\quad \times \exp\left\{-\left[\frac{\mu_a\left(\rho^2+z_{3m}^2\right)}{D}\right]^{1/2}\right\} - z_{4m}\left(\rho^2+z_{4m}^2\right)^{-3/2} \\ &\quad \left. \times \left\{1+\left[\frac{\mu_a\left(\rho^2+z_{4m}^2\right)}{D}\right]^{1/2}\right\} \times \exp\left\{-\left[\frac{\mu_a\left(\rho^2+z_{4m}^2\right)}{D}\right]^{1/2}\right\}\right) \end{aligned} \tag{1.13}$$

The quantity R(ρ) represents the probability that a photon emitted by the source exits from the surface element *dS* at z=0 at distance ρ regardless of the length of its trajectory.
In Fig. 1.4 and 1.5 some examples of reflectance curves are shown. They are calculated implementing the analytical formulae in MATLAB. In Fig. 1.4 we can see how the time-resolved reflectance is affected by a change in ρ, μ_a and μ'_s. If ρ increases the peak of $R(\rho,t)$ decreases and it moves toward greater times (Fig. 1.4a). An increase of the absorption coefficient determines a faster decrease of the reflectance tale (Fig. 1.4b) while an increase of the reduced scattering coefficient determines a delay of the reflectance peak and a broadening of the curve (Fig. 1.4c). In Fig. 1.4 we can see how the CW reflectance is affected by a change in μ'_s and μ_a. We can see that the reflectance decreases faster as μ'_s and μ_a increases.

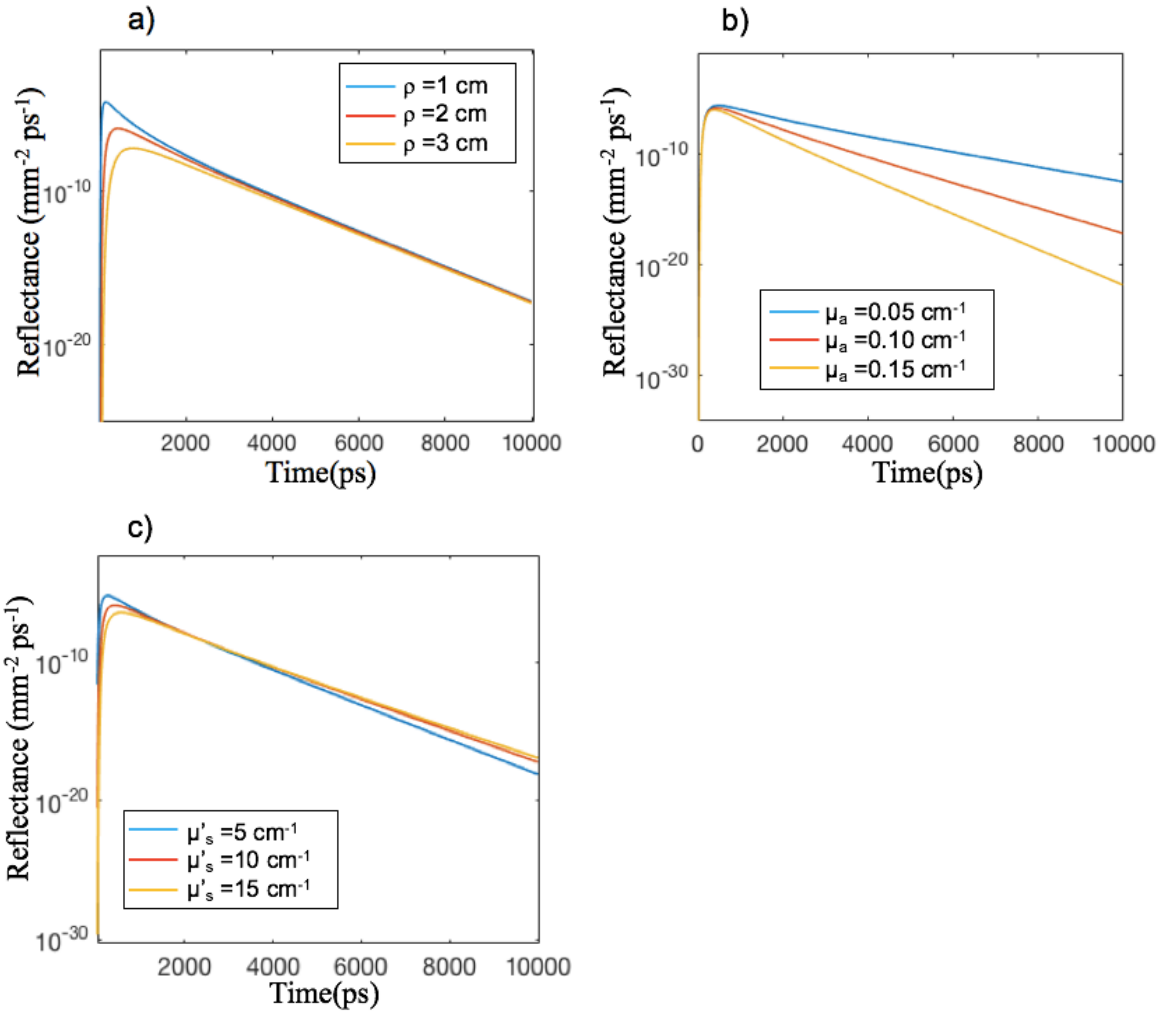

Figure 1.4: Examples of TD reflectance curves for a slab of thickness s=40 mm, n_e=1.0 (refractive index of the surrounding medium), n_i=1.4 (refractive index of the medium). In panel a), ρ varies while μ_a=0.1 cm^{-1}, μ'_s=10 cm^{-1}. In panel b), μ_a varies while ρ=2 cm, μ_s=10 cm^{-1}. In panel c), μ'_s varies while ρ=2 cm, μ_a=0.1 cm^{-1}.

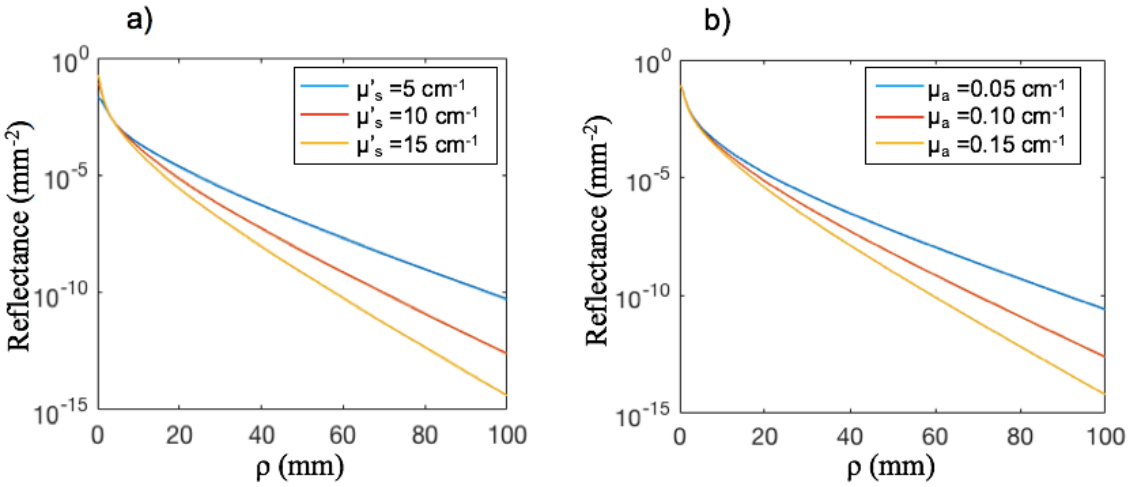

Figure 1.5: Examples of CW reflectance curves for a slab of thickness s=40 mm, n_e=1.0 (refractive index of the surrounding medium), n_i=1.4 (refractive index of the medium). In panel a) μ_a varies while μ_s=10 cm^{-1}. In panel b) μ'_s varies while μ_a=0.1 cm^{-1}.

1.3.2 Two-layer Cylinder geometry

In recent years there has been an enhanced interest in studying the problem of light propagation in layered diffusive media. One reason for this is its applications in the field of tissue optics. In fact, many diffusive media, and in particular several biological tissues, can be described by a sequence of diffusive layers having different optical properties [11]. Thus, several approaches have been proposed to study photon migration through layered diffusive media. We take into account the case of the two-layer cylinder geometry (Fig. 1.6). The medium V is composed of two regions: $V = V_1 \cup V_2$. s_1 and s_2 are the thickness, μ_{a1} and μ_{a2} are the absorption coefficients, D_1 and D_2 are the diffusion coefficients, and n_1 and n_2 are the refractive indices of the first and second layer, respectively. n_e is the refractive index of the surrounding medium that can be different at the two sides of the cylinder $z < 0$ and $z > s_1 + s_2$. The radius of the cylinder is denoted by L. An isotropic point source is located at $\vec{r_s} = (0,0,z_s)$, i.e., $q(\vec{r},t) = \delta(\vec{r} - \vec{r_s})\delta(t)$.

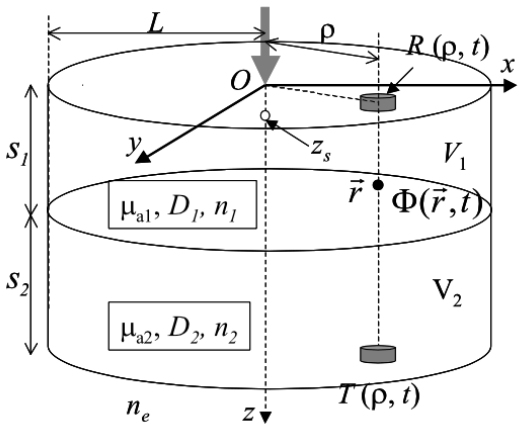

Figure 1.6: Graphic of two-layer cylinder geometry with symbols

The DE for the inhomogeneous medium is written as [2]:

$$\left\{\frac{1}{v}\frac{\partial}{\partial t}-\nabla[D(\vec{r})\nabla]+\mu_a\right\}\Phi(\vec{r},t)=\delta(\vec{r}-\overrightarrow{r_s})\delta(t). \qquad (1.14)$$

To solve this parabolic equation the initial and boundary value conditions are given in both layers introducing two functions for the fluence, $\Phi_1(\vec{r}, t)$ for the first layer and $\Phi_2(\vec{r},t)$ for the second layer, as follows [2]:

$$\begin{cases}\left(\frac{\partial}{v_1\partial t}-D_1\nabla^2+\mu_{a1}\right)\Phi_1(\vec{r},t)=0 & t>0,\quad 0\le z<s_1\\ \left(\frac{\partial}{v_2\partial t}-D_2\nabla^2+\mu_{a2}\right)\Phi_2(\vec{r},t)=0 & t>0,\quad s_1\le z\le s_1+s_2\,,\end{cases} \qquad (1.15)$$

and the initial and boundary value conditions are

$$\begin{aligned}\Phi_1(\rho=L,z,t)=\Phi_1(\rho,z=-z_{1e},t)=0\,,\\ \Phi_2(\rho=L,z,t)=\Phi_2(\rho,z=s_1+s_2+z_{2e},t)=0\,,\\ \Phi_1(\vec{r},t=0)=v_1\delta(\vec{r}-\overrightarrow{r_s})\,,\end{aligned} \qquad (1.16)$$

where z_{1e} and z_{2e} are the extrapolated distances at the surfaces z = 0 and z = s_1+s_2 respectively and the source is assumed in the first layer. We used the EBC at the surfaces z = 0 and z = s_1 + s_2 and the zero boundary conditions (ZBC) on the lateral surface of the cylinder.

A solution of the problem is then obtained with an eigenfuction expansion for the fluence rate [2]:

$$\begin{cases}\Phi_1(\vec{r},t)=\sum_{l,n=1}^{\infty}\alpha_{ln}\xi_{1ln}(\vec{r})\exp(-\lambda_{ln}t) & t>0,\quad 0\le z<s_1\\ \Phi_2(\vec{r},t)=\sum_{l,n=1}^{\infty}\alpha_{ln}\xi_{2ln}(\vec{r})\exp(-\lambda_{ln}t) & t>0,\quad s_1\le z\le s_1+s_2\,,\end{cases} \qquad (1.17)$$

where the same temporal evolution of Φ_1 and Φ_2 has been assumed (same coefficients α_{ln} and λ_{ln}) because the boundary condition at the interface of the layers requires this condition. The series depend on two indexes (l and n) because the problem investigated depends on the variables ρ and z. The solution of our initial and boundary value problem can be written as [2]

$$\Phi(\vec{r},t)=\begin{cases}\sum_{l,n=1}^{\infty}v_1^2J_0(K_{\rho l}\rho)\sin(K_{z1ln}z+\gamma_{1ln})\\ \times\sin^*(K_{z1ln}z_s+\gamma_{1ln})\exp[-(K_{1ln}^2D_1+\mu_{a1})v_1t]/N_{ln}^2\\ 0\le z<s_1\\ \\ \sum_{l,n=1}^{\infty}v_1^2J_0(K_{\rho l}\rho)b_{2ln}\sin(K_{z2ln}z+\gamma_{2ln})\\ \times\sin^*(K_{z1ln}z_s+\gamma_{1ln})\exp[-(K_{2ln}^2D_2+\mu_{a2})v_2t]/N_{ln}^2\\ s_1\le z\le s_1+s_2,\end{cases} \qquad (1.18)$$

where J_0 is the Bessel function of the first kind of order zero and with:

$$b_{2ln} = a_{2n} = \frac{\sin(K_{z1ln}s_1 + \gamma_{1ln})}{\sin(K_{z2ln}s_1 + \gamma_{2ln})}(n_2/n_1)^2 = -\frac{\sin[K_{z1ln}(s_1 + z_{1e})]}{\sin[K_{z2ln}(s_2 + z_{2e})]}(n_2/n_1)^2. \quad (1.19)$$

The coefficients $K_{\rho l}$, K_{z1ln}, K_{z2ln}, K_{1ln}, K_{2ln} are obtained imposing the boundary conditions, while N_{ln} is defined as:

$$N_{ln}^2 = v_1 \int_{V_{1e}} \xi_{1ln}(\vec{r})\xi_{1ln}^*(\vec{r})d\vec{r} + v_2 \int_{V_{2e}} \xi_{2ln}(\vec{r})\xi_{2ln}^*(\vec{r})d\vec{r}. \quad (1.20)$$

In order to obtain the expression of the reflectance, the extrapolated boundary partial current approach (EBPC) is used, i.e., the partial current boundary condition (PCBC) applied to the solution for the fluence obtained using EBC. The explicit expression for the reflectance results as [2]:

$$R(\rho, t) = \frac{\Phi(\rho, z=0, t)}{2A} \quad (1.21)$$

Solutions of the DE in case of steady-state source (CW) are obtained by integrating time-resolved reflectance over time.

In Fig. 1.7 some examples of reflectance curves for the two-layer cylinder geometry calculated with MATLAB are shown.

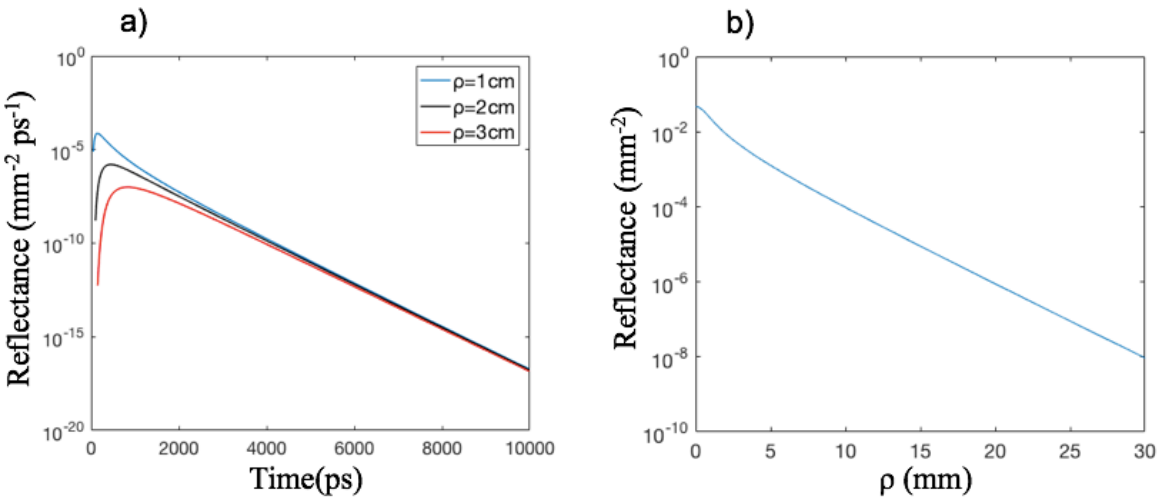

Figure 1.7: examples of reflectance curves for a two-layer cylinder with s_1=s_2=20 mm, μ_{a1}=0.075 cm^{-1}, μ_{a2}=0.15 cm^{-1}, μ_{s1}=10 cm^{-1}, μ_{s2}=5 cm^{-1}, n_e=1.0 (refractive index of the surrounding medium), n_1=n_2=1.4 (refractive index of the medium). Time-resolved curves and CW curves are respectively shown in panel a) and panel b).

Bibliography Chapter 1

[1] A. Ishimaru, Wave Propagation and Scattering in Random Media, Vol. 1, Academic Press, New York (1978).

[2] F. Martelli, S. Del Bianco, A. Ismaelli, G. Zaccanti, "Light propagation through biological tissue and other diffusive media", SPIE, Bellingham (2010), Chap. 2, 3, 4, 6.

[3] J. J. Duderstadt and W. R. Martin, "Transport Theory″, John Wiley & Sons, New York (1979).

[4] B. Yang and M. S. Li, "The discrete ordinates method for anisotropic scattering in the neutron transport theory: The critical sphere problem," J. Quant. Spectrosc. Radiat. Transf. 98, 116–121 (2006).

[5] T. Feng, P. Edström, and M. Gulliksson, "Levenberg-Marquardt methods for parameter estimation problems in the radiative transfer equation," Inverse Probl. 23, 879–891 (2007).

[6] L. V. Wang and H. Wu, "Biomedical Optics, Principles and Imaging", John Wiley & Sons, New York, (2007).

[7] S. Chandrasekhar, "Radiative Transfer", Oxford University Press, London/Dover, New York (1960).

[8] E. Zauderer, "Partial Differential Equations of Applied Mathematics″, John Wiley & Sons, New York (1989).

[9] R. C. Haskell, L.O. Svaasand, T.T. Tsay, T.C. Feng, M.S. McAdams and B.J. Tromberg, J. Opt. Soc. Am. A, 11, 2727-2741, 1994.

[10] D. Contini, F. Martelli, and G. Zaccanti, "Photon migration through a turbid slab described by a model based on diffusion approximation. I. Theory," *Appl. Opt.* 36, 4587–4599 (1997).

[11] V. Tuchin, "Tissue Optics", SPIE Press, Bellingham, WA (2000).

CHAPTER 2

Penetration depth of photons

In many research fields such as biomedical optics [1], advanced microscopy [2], or disordered photonics[3], light is used as a tool to noninvasively extract useful information on what is below the surface of the related random media. Usually, the medium is addressed in reflectance geometry, where light, injected and collected from the same side of its external surface, carries information on the medium optical properties encoded along photons random paths. In these applications the information on the penetration depth of photons injected in the media is crucial. For example, in brain functional imaging or in neuro-monitoring [4] a key challenge is the extraction of specific brain-cortex signals out of the superficial contamination generated, e.g., by scalp, skull and cerebrospinal fluid. Thus, it is essential to know whether or not light penetrates deep enough to reach the cortex area to be examined. Depth information is important also for other emerging applications such as cancer screening in thyroid or prostate [5], or for non-clinical fields, such as internal quality assessment of agricultural produce [6], or for pharmaceuticals and highly scattering plastics [7].
In this chapter the general formulation of the statistics of the photon penetration depth will be presented together with its application to the homogeneous slab geometry.

2.1 Previous works on penetration depth

The penetration depth of photons migrating in random media has been studied by several research groups. The mean average depth $\langle \bar{z} \rangle$ or the mean maximum depth $\langle z_{max} \rangle$ reached by photons detected at the surface of the medium are the main quantities investigated.
The paper written by Bonner et al. [8] was a pioneering work on this subject. It used a simple random walk model of light propagation to provide expressions for the continuous wave (CW) probability density of $\langle z_{max} \rangle$ for photons that emerge at a distance ρ from the injection point of light. In other papers [9,10] the continuous time random walk model was used to derive analytical expressions for $\langle \bar{z} \rangle$ and $\langle z_{max} \rangle$ in the approximation of large ρ. $\langle \bar{z} \rangle$ appeared to be proportional to $\rho^{1/2}$. The first expression for $\langle z_{max} \rangle$ in time domain was presented by Weiss et al. [9] in which $\langle z_{max} \rangle$ is found to depend on $t^{1/2}$. The last work on this subject is written by Martelli et al. [11] and gives a general description of the statistics behind the penetration depth of light in a turbid medium within the framework of the Radiative Transfer Equation (RTE) for both TD and CW domain. In Martelli's paper also the results for $\langle z_{max} \rangle$ and $\langle \bar{z} \rangle$ for an infinite slab in the diffusion approximation (DA) are presented and systematically validated by "gold standard" MC simulations.
In the next paragraph the general formulation of the penetration depth statistics will be presented following the method used in Martelli et al. [11].

2.2 Statistics of photon penetration depth

2.2.1 Probability density function

The theory presented in this section holds within the framework of the RTE. Let's consider a slab of finite thickness s_0 and infinite width, reduced scattering coefficient μ_s', absorption coefficient μ_a. A pencil beam impinges perpendicularly to the entrance surface of the slab and a detector is located on the surface at a distance ρ from the source (Fig. 2.1).

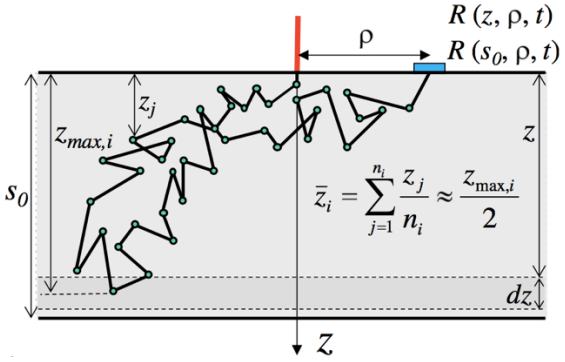

Figure 2.1: Schematic for a 2D projection of a detected photon trajectory from a diffusive slab: z_j is the value of the z coordinate (depth) when photon experiences a scattering event along the detected trajectory i. n_i is the number of scattering events in the detected trajectory i.

Our aim is to define the probability density function that the emerging photons from the medium have a z_{max} between z and z + dz. This function can be derived comparing the signal detected on two slabs with thicknesses z and z + dz respectively and located inside the original slab. Thus the difference between the two signals detected is given by the photons which have gone beyond z but not beyond z + dz. For a slab of thickness s_0, the fraction of photons detected at distance ρ and time t with the maximum penetration depth z_{max} between z and z + dz (with the z axis along the incident pencil beam as in Fig. 2.1) is given by the ratio [11]:

$$\frac{R(s=z+dz,\rho,t)-R(s=z,\rho,t)}{R(s=s_0,\rho,t)}, \tag{2.1}$$

with $R(s,\rho,t)$ the TD reflectance at ρ from a slab of thickness s.
In the TD, the probability density function, $f(z \mid \rho,t)$, for the slab of thickness s_0 in the range $0 \leq z \leq s_0$ is defined as [11]

$$f(z \mid \rho,t) = \frac{1}{R(s_0,\rho,t)} \frac{R(s=z+dz,\rho,t)-R(s=z,\rho,t)}{dz} = \frac{1}{R(s_0,\rho,t)} \frac{\partial R(z,\rho,t)}{\partial z} \tag{2.2}$$

The meaning of the probability density function is the following: $f(z \mid \rho,t)dz$ represents the probability that the emerging photons from the slab at time t and interfiber distance ρ had a z_{max} between z and z+dz. Thus $f(z \mid \rho,t)$ provides a detailed description of the distribution of z_{max} for the photons emerging from the medium. The above definition of the probability density function is general and can be used without any restriction within the framework of the RTE. Thus, $f(z \mid \rho,t)$ can be practically calculated for homogeneous and inhomogeneous geometries with analytical solutions of the Diffusion Equation (DE) or of the RTE for the reflectance $R(s,\rho,t)$.
In the CW domain, we can define a probability density function, $f(z \mid \rho)$, as [11]

$$f(z \mid \rho) = \frac{1}{R(s_0,\rho)} \frac{\partial R(z,\rho)}{\partial z}, \tag{2.3}$$

with $R(s_0,\rho) = \int_0^\infty R(s_0,\rho,t)\,dt$ reflectance for the CW source. It is worth noting that $f(z/\rho)$ can also be obtained by averaging $f(z \mid \rho,t)$ over time using the function $R(s,\rho,t)$ as weigh factor, i.e, [11]

$$f(z \mid \rho) = \frac{\int_0^\infty R(s_0,\rho,t) f(z \mid \rho,t) dt}{\int_0^\infty R(s_0,\rho,t) dt}. \tag{2.4}$$

2.2.2 Mean maximum depth

The mean value of the maximum penetration depth, $\langle z_{max} \mid \rho,t \rangle$, of the photons emerging from the medium at distance ρ and at time t can be calculated using $f(z \mid \rho,t)$ in the following way [11]:

$$\langle z_{max} \mid \rho, t \rangle = \int_0^{s_0} z f(z \mid \rho, t) dz. \tag{2.5}$$

In the same we can express the mean maximum penetration depth for CW source of light, $\langle z_{max} \mid \rho \rangle$, using the probability density function $f(z \mid \rho)$ of Eq. 2.3 [11]:

$$\langle z_{max} \mid \rho \rangle = \int_0^{s_0} z f(z \mid \rho) dz. \tag{2.6}$$

The above theoretical approach is completely consistent within the framework of the RTE when Fresnel reflections do not occur at the external boundaries of the slab. Conversely, when there is a refractive index mismatch between the medium and the external space ($n_{rel} \neq 1$), we need to provide a correction to the above theory. In the definition of $f(z \mid \rho, t)$ we need to consider that for the slab of thickness z, having its upper surface coincident with that of the slab s_0 and its lower surface internal to it, no Fresnel reflections occur at its lower boundary. Thus in this case the reflectance $R(s = z, \rho, t)$ has to be replaced by a reflectance term $R'(s = z, \rho, t)$ free of Fresnel reflections at depth z [11].

2.2.3 Mean average depth

To know the mean value $\langle \bar{z} \mid \rho, t \rangle$ at which detected photons have undergone scattering events, i.e., the average value of the coordinates z of all the scattering events of the detected trajectories, an intuitive heuristic relation can be given as follow [8]:

$$\langle \bar{z} \mid \rho, t \rangle \approx \frac{\langle z_{max} \mid \rho, t \rangle}{2}. \tag{2.7}$$

And the same for the CW domain:

$$\langle \bar{z} \mid \rho \rangle \approx \frac{\langle z_{max} \mid \rho \rangle}{2}. \tag{2.8}$$

In fact, Eqs. 2.7 and 2.8 can be heuristically justified by representing a single trajectory i in a chaotic diffusive regime of photon migration (see Fig. 2.1). Given the maximum penetration $z_{max,i}$ of this trajectory we have roughly that [11]

$$\bar{z}_i = \sum_{j=1}^{n_i} \frac{z_j}{n_i} \approx \frac{z_{max,i}}{2}, \tag{2.9}$$

where z_j is the value of the z coordinate (depth) when photon experiences a scattering event along the detected trajectory i, and n_i is the number of scattering events in the detected trajectory i. In the following two paragraph these formula will be applied in the case of a homogeneous slab.

2.3 Homogeneous slab in the diffusion approximation

2.3.1 Expressions for *f* and ⟨z_{max}⟩

In this section the expressions for *f* and ⟨z_{max}⟩ for a homogeneous slab of infinite width in the diffusion approximation are provided for both TD and CW domain respectively.
If we consider the analytical solution of the DE for an infinite homogeneous slab in the TD, $R(s,\rho,t)$, the dependence on ρ is only the multiplicative factor $exp(-\rho\text{^}2/4Dvt)$, with $D=1/(3\mu_s')$ and v speed of light in the medium [12,13]. Thus, the dependence on ρ vanishes in $f_{DE}(z \mid \rho,t)$ and therefore also in $\langle z_{max} \mid \rho,t\rangle_{DE}$. This implies that $f_{DE}(z \mid \rho,t) = f_{DE}(z \mid t)$.
Taking into account the possible refractive index mismatch between the medium and the external space ($n_{rel}\neq 1$), $R'(z,\rho,t)$ is found by substituting the parameters z_{3m} and z_{4m} in Eq. 1.11 with z'_{3m} and z'_{4m} defined in this way [11]:

$$\begin{aligned} M &= -2mz_e - 2mz'_e - z_s \\ N &= -2mz'_e - (2m-2)z_e + z_s \\ z'_{3m} &= -2mz + M \\ z'_{4m} &= -2mz + N, \end{aligned} \tag{2.10}$$

with $z_s = 1/\mu_s'$ position of an isotropic source of unitary strength used to model an external pencil beam of unitary strength impinging onto the slab, $z_e = 2AD$ extrapolated distance obtained in accordance to the extrapolated boundary condition (A coefficient for the Fresnel reflection), and $z'_e=2D$ extrapolated distance in absence of Fresnel reflections.
By using Eq. 2.2 we find the expression for the probability density function in the TD [11]:

$$f_{DE}(z \mid t) = \frac{\sum_{m=-\infty}^{m=+\infty}\left[a_{3m}\exp\left(-\frac{z'^{2}_{3m}}{4Dvt}\right) - a_{4m}\exp\left(-\frac{z'^{2}_{4m}}{4Dvt}\right)\right]}{\sum_{m=-\infty}^{m=+\infty}\left[z_{3m0}\exp\left(-\frac{z_{3m0}^{2}}{4Dvt}\right) - z_{4m0}\exp\left(-\frac{z_{4m0}^{2}}{4Dvt}\right)\right]}, \tag{2.11}$$

where

$$\begin{aligned} a_{3m} &= -2m + 4mz'^{2}_{3m}/(4Dvt) \\ a_{4m} &= -2m + 4mz'^{2}_{4m}/(4Dvt) \\ z_{3m0} &= -2ms_0 - 4mz_e - z_s \\ z_{4m0} &= -2ms_0 - (4m-2)z_e + z_s, \end{aligned} \tag{2.12}$$

Making use of Eq. 2.5, where we replace $f(z \mid t)$ with $f_{DE}(z \mid t)$ (Eq. 2.11), and after solving the integral in z, we obtain the analytical solution for $\langle z_{max} \mid t\rangle_{DE}$ that is [11]:

$$\langle z_{max} \mid t\rangle_{DE} = \int_0^{s_0} z f_{DE}(z \mid t) dz = \left\{ \sum_{m=-\infty}^{m=\infty} \left[z_{3m0} \exp\left(-\frac{z_{3m0}^2}{4Dtv}\right) - z_{4m0} \exp\left(-\frac{z_{4m0}^2}{4Dtv}\right) \right] \right\}^{-1}$$
$$\times \sum_{\substack{m=-\infty \\ m\neq 0}}^{m=\infty} \left\{ \frac{Dtv}{m} \left[\exp\left(-\frac{M^2}{4Dtv}\right) - \exp\left(-\frac{N^2}{4Dtv}\right) \right] - \frac{2m^2 s_0^2 + Dtv - Mms_0}{m} \exp\left(-\frac{(2ms_0 - M)^2}{4Dtv}\right) \right.$$
$$\left. + \frac{2m^2 s_0^2 + Dtv - Nms_0}{m} \exp\left(-\frac{(2ms_0 - N)^2}{4Dtv}\right) \right\}. \tag{2.13}$$

It is worth noting that, thanks to the RTE properties for homogeneous media, $f(z \mid t)$ and $\langle z_{max} \mid t\rangle$ are also independent of μ_a, but they still depend on μ_s' [11].

For the CW domain we act similarly to the TD starting from the analytical solution for the reflectance, $R'(z,\rho)$ (Eq.1.13) substituting z_{3m} and z_{4m} with z'_{3m} and z'_{4m} respectively (2.10). By using Eq. 2.3 we have that $f_{DE}(z \mid \rho)$ is [11]

$$f_{DE}(z \mid \rho) = \frac{1}{4\pi R_{DE}(s_0, \rho)} \sum_{m=-\infty}^{m=+\infty} \left\{ m \right.$$
$$\times \left[e^{-\mu_{eff}\sqrt{Z_m^-}} \left(\frac{6\mu_{eff} z_m^{-2}}{Z_m^{-2}} - \frac{2\mu_{eff}}{Z_m^-} + \frac{2(\mu_{eff}^2 z_m^{-2} - 1)}{Z_m^{-3/2}} + \frac{6 z_m^{-2}}{Z_m^{-5/2}} \right) \right.$$
$$\left. \left. - e^{-\mu_{eff}\sqrt{Z_m^+}} \left(\frac{6\mu_{eff} z_m^{+2}}{Z_m^{+2}} - \frac{2\mu_{eff}}{Z_m^+} + \frac{2(\mu_{eff}^2 z_m^{+2} - 1)}{Z_m^{+3/2}} + \frac{6 z_m^{+2}}{Z_m^{+5/2}} \right) \right] \right\}, \tag{2.14}$$

where

$$z_m^+ = 2mz - M$$
$$z_m^- = 2mz - N$$
$$Z_m^+ = \rho^2 + z_m^+$$
$$Z_m^- = \rho^2 + z_m^-$$
$$\mu_{eff} = \sqrt{\mu_a / D} \tag{2.15}$$

By using Eqs. 2.6 and 2.14 we obtain $\langle z_{max} \mid \rho\rangle_{DE}$ [11]

$$\langle z_{max} | \rho \rangle_{DE} = s_0 + \frac{1}{4\pi R_{DE}(s_0,\rho)} \sum_{\substack{m=-\infty \\ m\neq 0}}^{m=\infty} \left\{ \frac{\exp\left[-\mu_{eff}\sqrt{\rho^2 + z_{m0}'^{+2}}\right]}{2m\sqrt{\rho^2 + z_{m0}'^{+2}}} - \frac{\exp\left[-\mu_{eff}\sqrt{\rho^2 + z_{m0}'^{-2}}\right]}{2m\sqrt{\rho^2 + z_{m0}'^{-2}}} \right.$$
$$\left. - \frac{\exp\left[-\mu_{eff}\sqrt{\rho^2 + M^2}\right]}{2m\sqrt{\rho^2 + M^2}} + \frac{\exp\left[-\mu_{eff}\sqrt{\rho^2 + N^2}\right]}{2m\sqrt{\rho^2 + N^2}} \right\} +$$
$$- \frac{s_0}{4\pi R(s_0,\rho)} \left\{ \frac{z_{00}'^{+}\mu_{eff}\exp\left[-\mu_{eff}\sqrt{\rho^2 + z_{00}'^{+2}}\right]}{\rho^2 + z_{00}'^{+2}} + \frac{z_{00}'^{+}\exp\left[-\mu_{eff}\sqrt{\rho^2 + z_{00}'^{+2}}\right]}{[\rho^2 + z_{00}'^{+2}]^{3/2}} \right.$$
$$\left. - \frac{z_{00}'^{-}\mu_{eff}\exp\left[-\mu_{eff}\sqrt{\rho^2 + z_{00}'^{-2}}\right]}{\rho^2 + z_{00}'^{-2}} - \frac{z_{00}'^{-}\exp\left[-\mu_{eff}\sqrt{\rho^2 + z_{00}'^{-2}}\right]}{[\rho^2 + z_{00}'^{-2}]^{3/2}} \right\}, \tag{2.16}$$

where

$$\begin{aligned} z'^{+}_{m0} &= 2m s_0 - M \\ z'^{-}_{m0} &= 2m s_0 - N \\ z'^{+}_{00} &= z_s \\ z'^{-}_{00} &= -2z_e - z_s \,. \end{aligned} \tag{2.17}$$

We note that, in contrast to the TD, in the CW domain both $f\,(z \mid \rho)$ and $\langle z_{max} \mid \rho \rangle$ depend also on μ_a.

At this point, it must be stressed that the normalization of the probability density functions $f_{DE}\,(z \mid t)$ and $f_{DE}\,(z \mid \rho)$ is subjected to the conditions $R_{DE}\,(z=0,\rho,t) = 0$ and $R_{DE}\,(z=0,\rho) = 0$ whose validity is expected for obvious physical reasons. Within the framework of the diffusion approximation (DA) these conditions are usually well verified. However, for high values of μ_a and small values of s_0, when the DA is expected to fail, the above probability density functions may be affected by normalization deficiencies [11].

All the above definitions can be extended to a semi-infinite medium by considering a slab with a sufficiently large thickness.

2.3.2 Relevant examples for f and $\langle z_{max} \rangle$

In this paragraph some significant curves representing f and $\langle z_{max} \rangle$ for a homogeneous slab will be shown both in TC and CW domain. The curves are obtained implementing in MATLAB the formula presented in the previous paragraph.

In Fig. 2.2, the probability density functions $f_{DE}\,(z \mid t)$ and $f_{DE}\,(z \mid \rho)$ are reported for different values of t and ρ respectively for a homogeneous slab with μ_a=0.1 cm^{-1}, μ_s' =10 cm^{-1}. In Fig. 2.2a we can see how the probability distribution for the maximum penetration depth z_{max} moves towards deeper values of z by increasing the time. This is due to the fact that increasing the time means selecting photons with a greater time of flight, i.e., the time passed inside the medium by photons. If time of flight increases, photons have a higher probability to be scattered deeply in the medium and so to experience a greater z_{max}. Moreover, the width of the curve becomes larger as the time increases since the variance of z_{max} increases. In the CW domain, the probability density function $f\,(z \mid \rho)$ depends on ρ, as we can see in Fig. 2.2b. It is worth noting that the peak of $f\,(z \mid \rho)$ goes toward larger values of z as the interfiber distance increases since photons detected at a larger ρ experience a greater pathlength inside the medium and so they have a greater z_{max} on average.

Figure 2.3 shows the mean maximum penetration depth according to Eqs. 2.13 and 2.15. The results pertain to a homogeneous slab with μ_s' = 10 cm^{-1} and $n_{int} = n_{ext}$= 1.4. In Fig 2.3a $\langle z_{max} \mid t \rangle$ is reported for different values of thickness s_0 and with μ_a=0.1 cm^{-1}. $\langle z_{max} \mid t \rangle$ grows rapidly for early times and more slowly for late times. This behavior is similar to that predicted by Weiss [9] for which $\langle z_{max} \rangle$ is found to depend on $t^{1/2}$. Fig 2.3b shows $\langle z_{max} \mid \rho \rangle$ as a function of ρ for values of $\mu_a \in [10^{-3}, 1]$ cm^{-1} which are typical to the absorption of biological tissues in the near infrared spectral region. As μ_a increases, a larger interfiber

distance ρ have to be used to reach the same depth.
The agreement with MonteCarlo simulations is very good except for very early times (t<100 ps) and large value of μ_a (μ_a ~10 cm^{-1}) since in these two cases the diffusion approximation is no more valid [11].

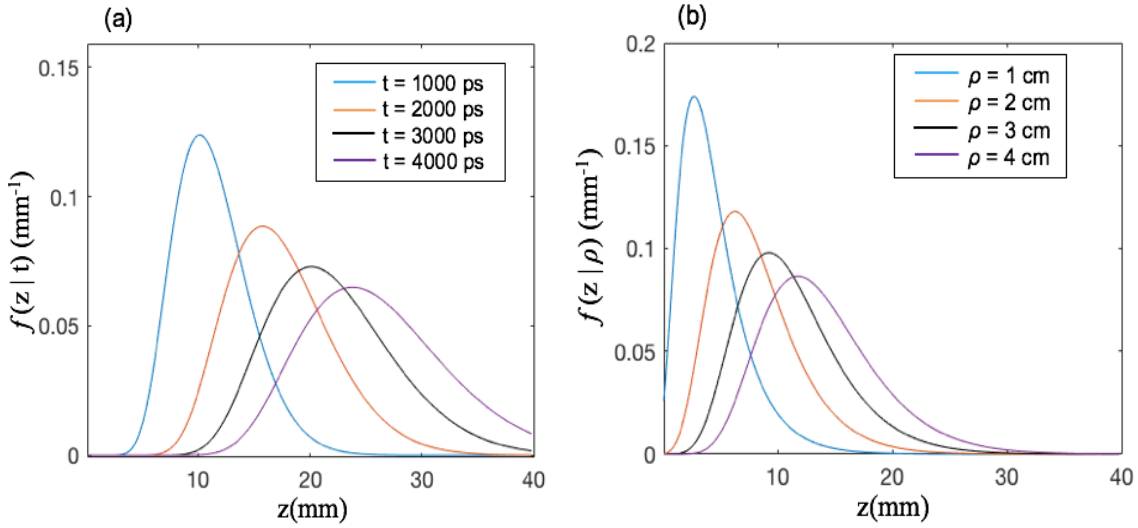

Figure 2.2: Probability density functions f versus depth z, calculated exploiting DE for a homogeneous slab with s_0=4 cm, μ_a=0.1 cm^{-1}, μ_s' =10 cm^{-1}, n_{int}=1.4, n_{ext}=1.0. In panel (a) f (z | t) is shown for different times t, ρ=20 mm. In panel (b) f (z | ρ) for different interfiber distances ρ.

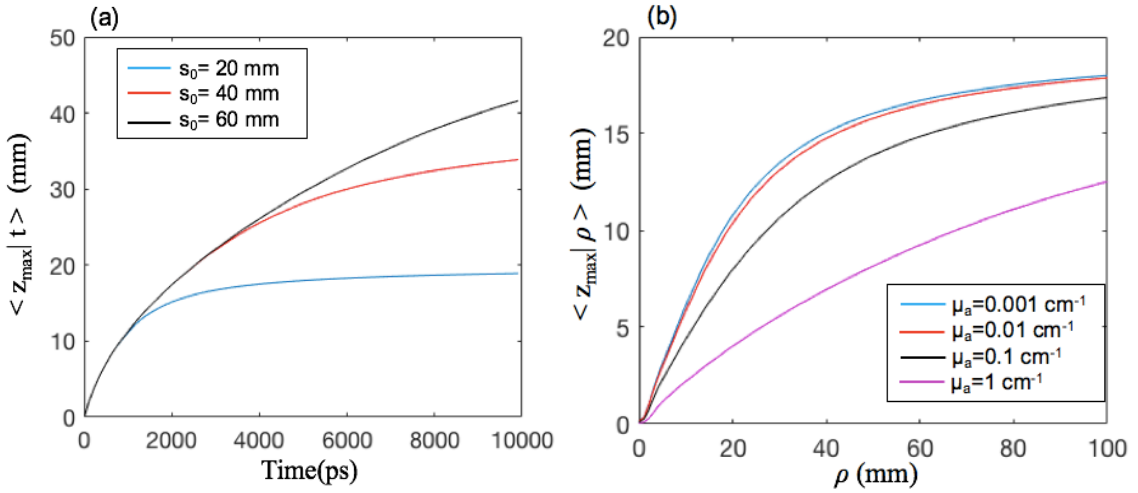

Figure 2.3: In panel a) $\langle z_{max} | t \rangle$ versus time for different values of s_0, a) pertains to a homogenous slab with μ_a=0.1 cm^{-1} . In panel b) $\langle z_{max} | \rho \rangle$ versus ρ for different values of μ_a. b) pertains to a homogenous slab with s_0=2 cm. For both panel a) and b) we have μ_s' = 1 mm and n_{int} = n_{ext}= 1.4.

As already said the statistical approach proposed is general within the RTE and it can be applied to inhomogeneous geometries with analytical solutions of DE or RTE. Since until now no paper takes into account the case of multilayer geometry, the aim of the following chapters is to apply the statistics here presented to the bilayer geometry and to make a picture of the dependence of $\langle z_{max} \rangle$ from the physical parameters that characterize the medium. To begin with, we have to develop a methodology to obtain in a numerical way the mean maximum penetration depth because no closed-form solutions are available for it in the bilayer case. This methodology will be explained in detail in the next chapter together with its validation.

Bibliography Chapter 2

[1] T. Durduran, R. Choe, W. B. Baker, and A. G. Yodh, "Diffuse optics for tissue monitoring and tomography," Rep. Prog. Phys. 73, 076701 (2010).

[2] O. Katz, E. Small, Y. Bromberg, and Y. Silberberg, "Focusing and compression of ultrashort pulses through scattering media," Nature Photonics 5, 372–377 (2011).

[3] D. S. Wiersma, "Disordered photonics," Nat. Photonics 7, 188-196 (2013).

[4] A. Torricelli, D. Contini, A. Pifferi, M. Caffini, R. Re, L. Zucchelli, and L. Spinelli, "Time domain functional NIRS imaging for human brain mapping," Neuroimage 85, 28-50 (2014).

[5] K. K.-H. Wang and T. C. Zhu, "Reconstruction of in-vivo optical properties for human prostate using interstitial diffuse optical tomography," Opt. Express 17, 11665-11672 (2009).

[6] R.Cubeddu, C.Andrea, A.Pifferi, P.Taroni, A.Torricelli, G.Valentini, C. Dover, D. Johnson, M.Ruizaltisent, and C.Valero, "Nondestructive quantification of chemical and physical properties of fruits by time-resolved reflectance spectroscopy in the wavelength range 650 - 1000 nm," Appl. Opt. 40, 538-543 (2001).

[7] D. Khoptyar, A. A. Subash, S. Johansson, M. Saleem, A. Spare´n, J. Johansson, and S. Andersson-Engels, "Broadband photon time-of-flight spectroscopy of pharmaceuticals and highly scattering plastics in the VIS and close NIR spectral ranges," Opt. Express 21, 20941–20953 (2013).

[8] R.F.Bonner, R.Nossal, S.Havlin, and G.H.Weiss, "Model for photon migration in turbid biological media,"J.Opt.Soc. Am. A 4, 423-432 (1987).

[9] G. Weiss, "Statistical Properties of the Penetration of Photons into a Semi-Infinite Turbid Medium: A Random-Walk Analysis," Appl. Opt. 37, 3558-3563 (1998).

[10] G. Weiss, J. Porrà, and J. Masoliver, "Statistics of the depth probed by cw measurements of photons in a turbid medium," Phys. Rev. E 58, 6431-6439 (1998).

[11] F. Martelli, T. Binzoni, A. Pifferi, L. Spinelli, A. Farina, and A.Torricelli, "There's plenty of light at the bottom: statistics of photon penetration depth in random media", Scientific Reports 6:27057 (2016).

[12] D. Contini, F. Martelli, and G. Zaccanti, "Photon migration through a turbid slab described by a model based on diffusion approximation. I. Theory," Appl. opt. 36, 4588-4599 (1997).

[13] F. Martelli, S. Del Bianco, A. Ismaelli, and G. Zaccanti, "Light Propagation through Biological Tissue and Other Diffusive Media: Theory, Solutions and Software", SPIE Press, Washington, USA, (2010), Chap. 4.

CHAPTER 3

Implementation and validation of a numerical method for the analysis of photon penetration depth in the bilayer geometry

Layered model geometries are employed in tissue optics, motivated by the fact that some biological tissues have a layered architecture. This is the case of muscle underneath a superficial fat layer or of the head with compartments such as scalp, skull, and brain. Thus, the study of photon penetration depth in these layered geometries can be very interesting in many fields. Optical reflectance spectroscopy is an example of biomedical application in which the information about the penetration depth of light is crucial for the non-invasive tissue analysis and investigation. One reason for this is because pathologic conditions and tissue alterations are localized at specific morphological structures and the study of the penetration depth permits to determine the exact tissue layers being interrogated by optical spectroscopy [1].

In Chapter 2 analytical formulae of the penetration depth have been presented for homogeneous geometries. The same approach can be applied, in all generality, to inhomogeneous media. In particular, making use of analytical solutions of the DE in layered geometries, numerical evaluations of the relative $\langle z_{max} \mid t \rangle_{DE}$ and $\langle z_{max} \mid \rho \rangle_{DE}$ can be obtained [2].

In this chapter a methodology to obtain in a numerical way the mean maximum penetration depth for the bilayer geometry is presented. The first part of the chapter is dedicated to the implementation and validation of the method used for TD measures, while the second part is dedicated to the CW domain.

3.1 Implementation of the numerical method in TD

The numerical method used in TD consists of three stages summarized in the following. Let's consider a bilayer slab with the two layers having different optical properties and thicknesses s_1 and s_2 respectively, with a collimated light beam impinging on it (Fig. 3.1).

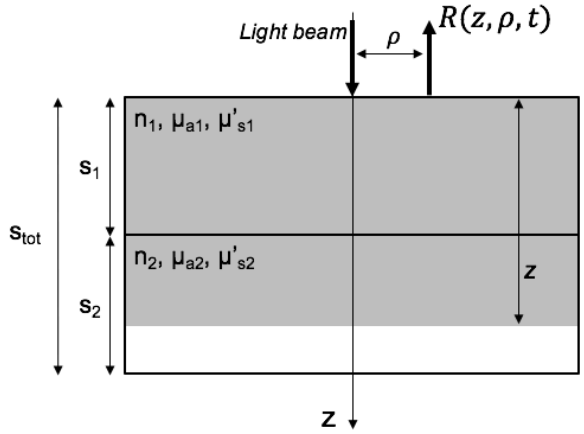

Figure 3.1: Section of a bilayer slab with n_1, μ_{a1} and μ'_{s1} optical parameters of the first layer of thickness s_1 and n_2, μ_{a2} and μ'_{s2} optical parameters of the second layer of thickness s_2. $s_{tot}= s_1 + s_2$. Reflectance $R(z,\rho,t)$ refers to a slab of thickness z placed inside the bilayer structure.

The first stage consists in the numerical evaluation of the reflectance $\tilde{R}(z,\rho,t)$ discretized in time, with interfiber distance ρ and from a slab of thickness z placed inside the bilayer structure, as we can see in Fig. 3.1.
The second stage consists in the calculation of the probability density function, *f (z | ρ,t)*, using Eq. 2.2 [2]. The numerical evaluation of *f (z | ρ,t)* is made by considering the incremental ratio instead of the derivative of $R(z,\rho,t)$:

$$f(z \mid \rho,t) = \frac{1}{R(s_{tot},\rho,t)}\frac{\partial R(z,\rho,t)}{\partial z} \cong \frac{1}{\tilde{R}(s_{tot},\rho,t)}\frac{\tilde{R}(z,\rho,t)-\tilde{R}(z-\Delta z,\rho,t)}{\Delta z} \qquad (3.1)$$

Thus, to calculate *f* (z_i | *ρ,t*) at a specific depth z_i inside the medium and at interfiber distance ρ, three reflectance curves numerically evaluated are taken into account which are $\tilde{R}(z_i,\rho,t)$, $\tilde{R}(z_i-\Delta z,\rho,t)$ and $\tilde{R}(s_{tot},\rho,t)$, with $s_{tot}= s_1 + s_2$. Repeating this stage with z sampled at regular steps, i.e., $z_i - z_{i-1} = \Delta z'$, and in the interval $0 < z < s_{tot}$, we obtain a probability density function discretized in time *t* and thickness *z*.
The last stage is the evaluation of the time-resolved mean maximum penetration depth, $\langle z_{max} \mid \rho,t\rangle$, making use of Eq. 2.5 with the integral numerically calculated:

$$< z_{max}|\,\rho,t >= \int_0^{s_{tot}} z\, f(z|\,\rho,t)\, dz \cong \sum_{i=1}^{numz} z_i f(z_i|\,\rho,t)\Delta z'. \qquad (3.2)$$

where the sum is over all the steps z_i (*numz* is the number of steps along z).
In Fig. 3.2 the block diagram gives an overview of the method used. The implementation of these three stages will be explained in detail in next paragraphs.

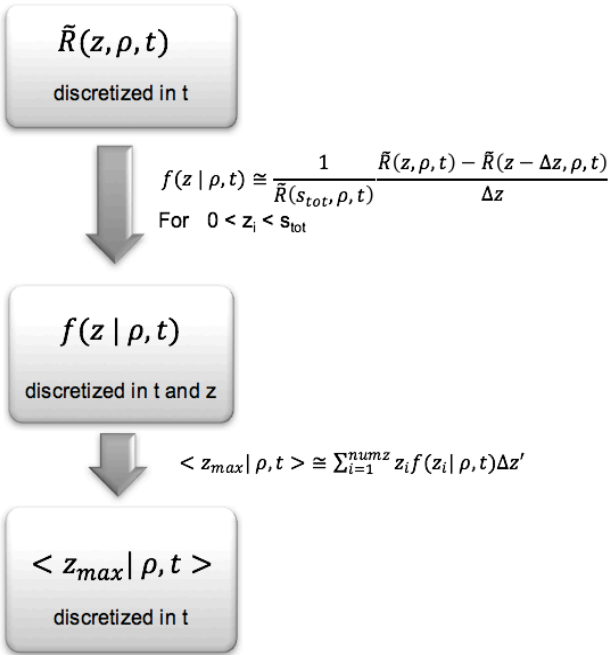

Figure 3.2: Block diagram of the method used.

3.1.1 Calculation of reflectance curves

Reflectance curves are numerical calculated by a software which implements the solution of the DE found with EPBC boundary condition [3] (see Chapter 1).
In order to get the probability density function, $f\ (z_i \mid \rho,t)$, we have to consider the reflectance by two slabs with thicknesses z_i and $z_i - \Delta z$ respectively and located inside the original bilayer slab. These two slabs are considered homogeneous if $0 < z_i \leq s_1$ and they have the same optical properties of the first layer of the given bilayer slab (Fig. 3.3a). If $s_1 < z_i \leq s_{tot}$ the two slabs of thicknesses z_i and $z_i - \Delta z$ are made up of two layers with the same optical properties of the given bilayer slab as we can see in Fig. 3.3b. In the first case the software evaluates $\tilde{R}(z_i, \rho, t)$ applying EBPC to the DE for the homogeneous slab. In the second case, the software applies EBPC to the DE for the two-layer cylinder geometry [3] (Fig. 3.4, see Chapter 1). We put the radius L large enough (L=10 cm) so that the boundary effects are negligible and the structure is equal to a bilayer slab of infinite width. In Eq. 3.1 we use the backward incremental ratio since in this way the two slabs of thicknesses z_i and $z_i - \Delta z$ are both homogeneous also when $z_i = s_1$. This helps a lot the calculations with the software used. Furthermore, in our simulations $\Delta z = 0.001$ mm since with this value the difference between the incremental ratio and the real derivative is negligible (see Eq. 3.1).
Another point that must be stressed is that when there is a refractive index mismatch between the medium and the external space ($n_{rel} \neq 1$), we need to ensure that for the slab of thickness z_i no Fresnel reflections occur at its lower boundary [2] (see Chapter 2). This is done by implementing in the software the possibility to choose different refractive indexes, n_e and n_e', respectively above and under the slab. Thus, when $z_i < s_{tot}$, n_e' is equal to internal refractive index of the bilayer slab (n_1 or n_2 depending on z_i, Fig. 3.3).

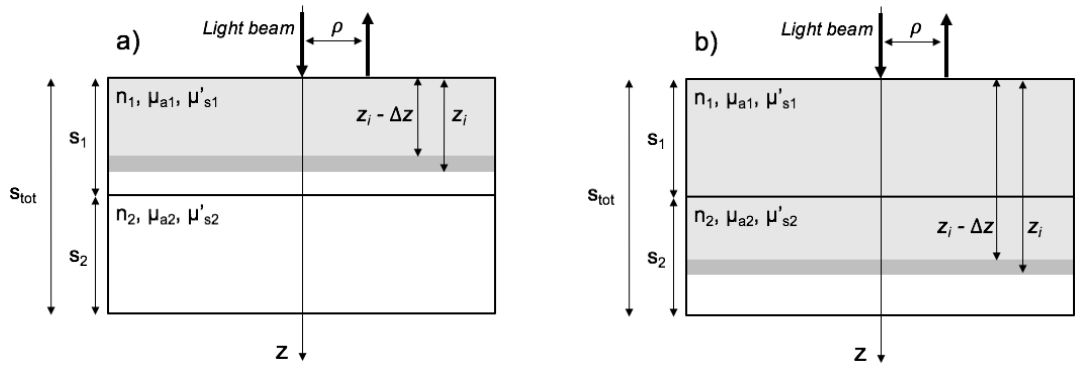

Figure 3.3: Sections of a given bilayer slab. n_1, μ_{a1} and μ'_{s1} are the optical parameters of the first layer of thickness s_1 while n_2, μ_{a2} and μ'_{s2} are the optical parameters of the second layer of thickness s_2. $s_{tot} = s_1 + s_2$. In fig. 3.3a the two grey slabs for which the reflectance is calculated are considered homogeneous since $z_i < s_1$. In fig. 3.3b the two grey slabs for which the reflectance is calculated are considered bilayer slabs since $z_i > s_1$.

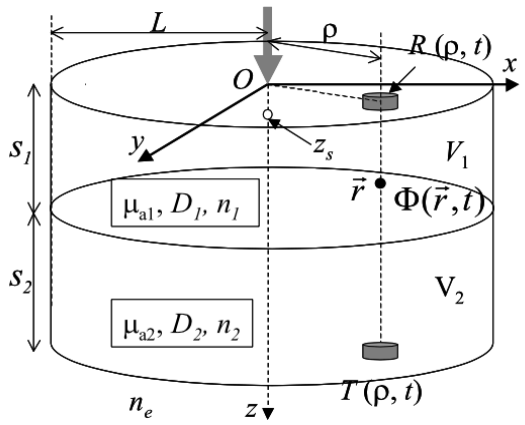

Figure 3.4: Graphic of two-layer cylinder geometry with symbols.

Once we fix z_i, the software returns an array of values which correspond to the reflectance at different times. We choose a step in time $\Delta t = 10$ ps and the time range goes from 0 ps to 10000 ps, so for each reflectance curve we have 1000 points. However, for $t_0 < \rho/v$ (ballistic time), the diffusion approximation does not hold anymore [3] (see Chapter 1), so the first points (early times) are not considered in the following calculations. For example, for $\rho = 2\ cm$ and n_{int}=1.4 we have $t_0 \cong 100$ ps, so the first ten points of reflectance curves are neglected in this case.

With two for-loops the software calculates $\tilde{R}(z_i, \rho, t)$ and $\tilde{R}_1(z_i - \Delta z, \rho, t)$ with $z_{in} < z_i < s_{tot}$ and $\Delta z' = z_i - z_{i-1} = 0.2$ mm. It is worth noting that $z_{in} \neq 0$ since for $z_{in} < 1/\mu'_s$ the single isotropic source approximation does not hold anymore [2]. For this reason in our simulations we choose $z_{in} = 1/\mu'_s$. For example, when $\mu'_s = 1$ mm^{-1} we have $z_{in} = 1$ mm.

3.1.2 Calculation of the probability density function

Once we have the reflectance curves $\tilde{R}(z_i, \rho, t)$ and $\tilde{R}_1(z_i - \Delta z, \rho, t)$ for all z_i, they are collected using MATLAB in two matrixes, $\underline{\underline{\tilde{R}}}(z_i, \rho, t)$ and $\underline{\underline{\tilde{R}_1}}(z_i - \Delta z, \rho, t)$ respectively. In each matrix one dimension represents the different times while the other represents the different thicknesses z_i.
It is worth noting that for small values of z_i and for great times the reflectance is really low and oscillates between positive and negative values. This is obviously unphysical so to overcome this computational error this part of the reflectance curve is replaced by zeros.
Then, the probability density function, f (z | ρ,t), is easily obtained by implementing on MATLAB the following matrix formula:

$$\underline{\underline{f}}(z_i \mid \rho, t) = \frac{1}{\tilde{R}(s_{tot}, \rho, t)} \frac{\underline{\underline{\tilde{R}}}(z_i, \rho, t) - \underline{\underline{\tilde{R}}}(z_i - \Delta z, \rho, t)}{\Delta z} \quad . \tag{3.3}$$

Thus, the probability density function numerically obtained is discretized in time and thickness.

3.1.2 Calculation of the mean maximum penetration depth

The mean maximum penetration depth is calculated implementing on MATLAB Eq. 3.2. Before the calculation of $\langle z_{max} \mid \rho,t \rangle$ is made, we impose the normalization on $f(z_i \mid \rho, t)$, i.e.,

$$\sum_{i=1}^{numz} f(z_i \mid \rho, t) \Delta z' = 1 \quad . \tag{3.4}$$

The normalization deficiencies affect the probability density function for high values of μ_a and small values of s_{tot} [2], when the diffusion approximation is expected to fail.
We obtain in this way a discrete function of time which gives us an idea of how much deep a photon goes inside a medium. It must be remembered that $\langle z_{max} \mid \rho,t \rangle$ is a statistical mean, so there may be photons with z_{max} much greater or lower than $\langle z_{max} \rangle$.

3.2 Validation of the numerical method in TD

Since there is no analytical formula available for $f(z \mid \rho,t)$ and $\langle z_{max} \mid \rho,t \rangle$ in the bilayer geometry, the validation of our model is done by comparing the results of our numerical method with the analytical formulae for the homogeneous slab geometry (Eqs. 2.11 and 2.13). These formulae have been already verified with MC simulations by the work of Martelli et al. [2] and the agreement found was really good.
The functions f (z | ρ,t) and $\langle z_{max} \mid \rho,t \rangle$ are numerically simulated for homogeneous slabs with different optical properties and thicknesses. Given a homogeneous slab of thickness

s_0, our model is applied in two ways. We start considering our bilayer geometry as made up with the only first layer ($s_1=s_0$ and $s_2=0$ in Fig. 3.1). In this way all the reflectance curves are calculated with the DE solution for the homogeneous slab. Then, we also calculate $f(z \mid t)$ and $\langle z_{max} \mid t \rangle$ considering the given homogeneous slab as composed of two identical slabs. This configuration is equal to Fig. 3.1 when the two layers have the same parameters and $s_1=s_2=s_0/2$. In this way we can check that the numerical method works well also with the DE solution of bilayer geometry (Fig. 3.6).

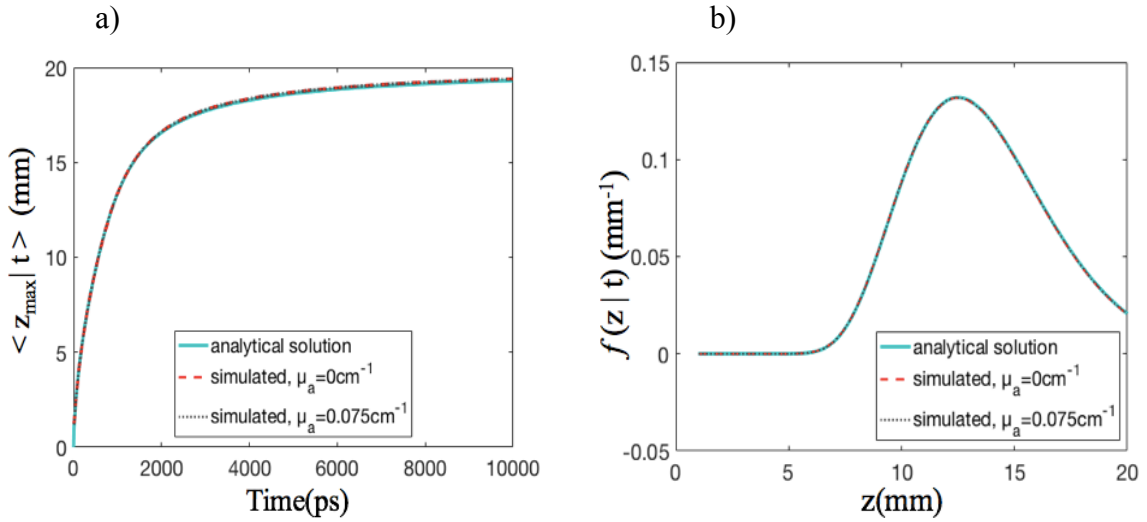

Figure 3.5: $\langle z_{max} \mid t \rangle$ and $f(z \mid t)$ for a homogeneous slab of thickness 20 mm, with $n_{int}=n_{out}=1.4$, $\mu'_s=10\ cm^{-1}$. The numerical solutions are reported for two different values of μ_a and in both cases the agreement with the analytical solution is very good since the curves are superimposed. Panel a) reports $\langle z_{max} \mid t \rangle$ as a function of t. Panel b) reports $f(z \mid t)$ as a function of z for t=1000 ps.

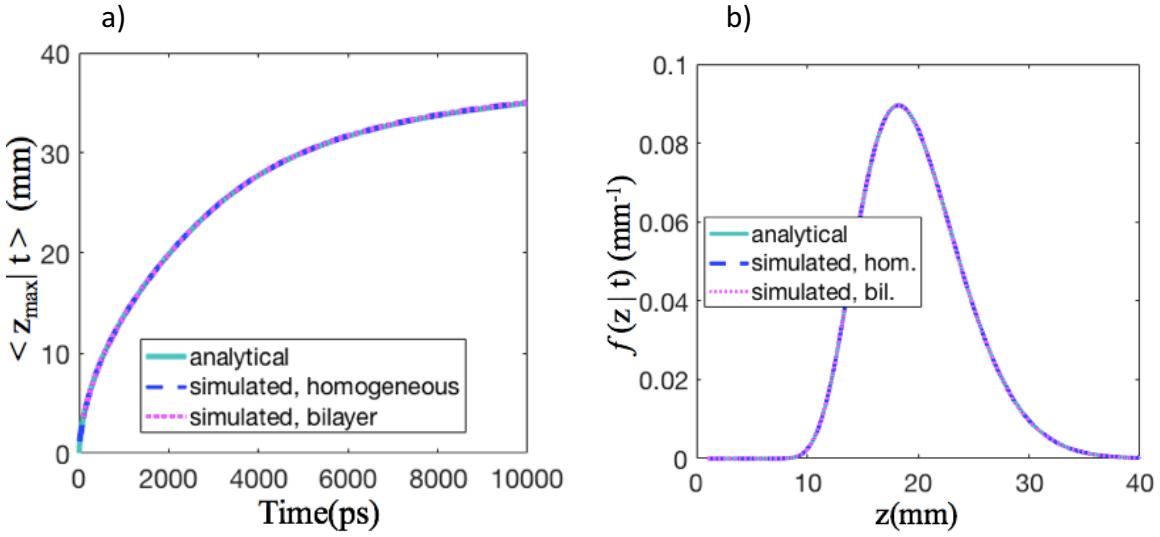

Figure 3.6: $\langle z_{max} \mid t \rangle$ and $f(z \mid t)$ for a homogeneous slab of thickness 40 mm, with $n_{int}=n_{out}=1.4$, $\mu'_s=10\ cm^{-1}$ and $\mu_a=0\ cm^{-1}$. The numerical solutions are calculated using only the homogeneous DE solution (simulated, homogeneous) or considering also bilayer DE solution (simulated, bilayer) and in both cases the agreement with the analytical solution is very good since the curves are superimposed. Panel a) reports $\langle z_{max} \mid t \rangle$ as a function of t. Panel b) reports $f(z \mid t)$ as a function of z for t=2000 ps.

The agreement between the numerical simulated functions and the analytical ones is very good for each configuration tested. In Fig. 3.5 and 3.6 two different configurations used in the simulations are reported. In both cases the accordance with the analytical formulae is really good for both *f (z | t)* and $\langle z_{max} \mid t \rangle$. For the slab of thickness 20 mm (Fig 3.5) the agreement is verified for two different values of the absorption coefficient. It must be remembered that in TD *f (z | t)* does not depend on μ_a in the homogeneous slab geometry and the same holds for $\langle z_{max} \mid t \rangle$ [2]. Also for the slab of thickness 40 mm the agreement with the analytical solution is very good as we can see in Fig. 3.6. We point out that $\langle z_{max} \mid t \rangle$ is always a monotonically increasing function of time. Indeed, when photons remain more time in the medium the probability to reach a deep z_{max} is higher. Moreover, *f (z | t)* is always a bell-shaped function of depth and it is peaked on the most probable *z*.
In the next two paragraphs the CW domain will be taken into account.

3.3 Implementation of the numerical method in CW domain

The approach followed to obtain the mean maximum penetration depth in CW domain, $\langle z_{max} \mid \rho \rangle$, is the same proposed in TD but starting from the reflectance $R(z,\rho)$ solution of the the DE in CW domain.
Numerically evaluated reflectance curves $\tilde{R}(z,\rho)$ are discrete functions of ρ sampled with a step of 0.1 mm in the interval 0 mm < ρ < 60 mm. The formula used for the calculation of $f(z \mid \rho)$ is:

$$f(z \mid \rho,) \cong \frac{1}{\tilde{R}(s_{tot},\rho)} \frac{\tilde{R}(z,\rho) - \tilde{R}(z-\Delta z,\rho)}{\Delta z} \ . \tag{3.5}$$

Thus, the probability density function obtained is a discrete function of ρ and z. Same values of the parameters Δz, z_{in} and $\Delta z'$ used in TD are chosen. Finally, $\langle z_{max} \mid \rho \rangle$ is numerically found:

$$< z_{max} \mid \rho > \cong \sum_{i=1}^{numz} z_i f(z_i \mid \rho) \Delta z'. \tag{3.6}$$

A important note must be mentioned for the calculation of $\tilde{R}(z,\rho)$. To calculate the analytical expressions for f and z_{max} in both TD and CW domain, the reflectance is obtained from the solution for the fluence based on the EBC and making use of Fick's law (Eq. 1.7). Solutions of the diffusion equation that use EBC can be significantly improved for steady-state spatially resolved reflectance by application of an approach used by Haskell et al. [4]. This approach calculates the outgoing flux as the integral of the radiance transmitted at the interface. The CW reflectance from the slab can be written as [4, 5]:

$$R(z,\rho) = \int_{2\pi} d\Omega [1 - R_F(cos\Theta)] \frac{1}{4\pi} [\Phi(\rho, z=0) + 3D \frac{\partial \Phi(\rho, z=0)}{\partial z} cos\Theta] cos\Theta \tag{3.7}$$

where Φ is the radiance, Θ is the angle relative to the normal to the boundary and R_F is the Fresnel reflection coefficient. Computing the integral an expression significantly different with respect to the solution obtained using only Fick's law is obtained [3, 5]:

$$R(z,\rho) = a\,\Phi(\rho, z=0) + bD\frac{\partial\Phi(\rho, z=0)}{\partial z}, \tag{3.8}$$

where a and b are numerical coefficients depending on the refractive index mismatch. As an example, for n_{int}/n_{out} = 1.4, a = 0.118 and b = 0.306 [6]. In Eq. 3.8 both the fluence and the flux are involved, and comparisons with MC results have shown that it gives a more accurate solution with respect to the solution based only on Fick's law [5]. For this reason, in the CW domain Eq. 3.8 is numerically implemented for both homogeneous slab geometry and bilayer slab geometry [6]. In Fig. 3.7 an example of reflectance curve calculated with both methods. It can be noticed that the differences between the two curves is significant at low ρ (ρ<10 mm).

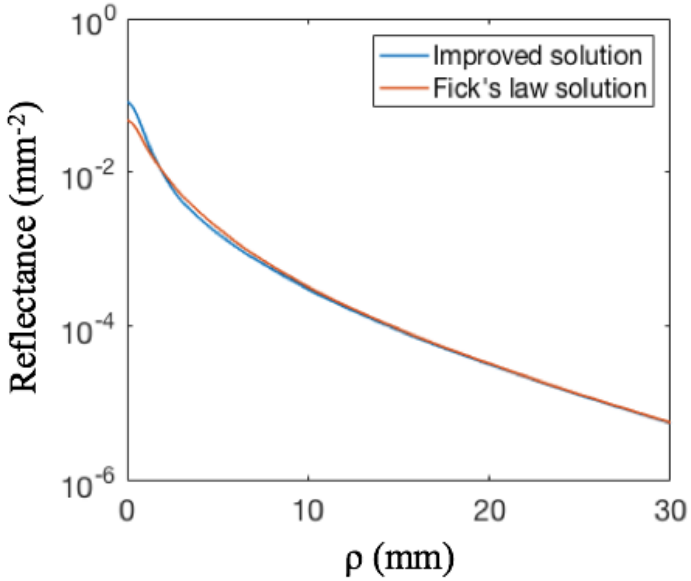

Figure 3.7: Reflectance curves calculated with improved solution or with Fick's law solution for a homogeneous slab of thickness 20 mm, with n_{int}=1.4, n_{out}=1.0, μ'_s =10 cm^{-1}, μ_a =0.01 cm^{-1}.

3.4 Validation of the numerical method in CW domain

The validation in CW domain follows the same approach used in TD and consists in comparing the results of our numerical method with the analytical formulae of $f(z \mid \rho)$ and $\langle z_{max} \mid \rho \rangle$ for the homogeneous slab geometry (Eqs. 2.14 and 2.16). These formulae have been already verified with MC simulations by the work of Martelli et al. [2], as for the case of TD. Test simulations with different thicknesses and optical parameters are done and the agreement with the analytical solutions is good for each configuration.
In Fig 3.8 we can see $f(z \mid \rho)$ and $\langle z_{max} \mid \rho \rangle$ calculated with the analytical formula (solid lines) and with the numerical method (dashed lines) in the case of a homogeneous slab of thickness s_0=20 mm. In Fig. 3.8a and 3.8b we can see that for each value of absorption

coefficient μ_a the two lines (dashed and solid) are superimposed except for very small interfiber distances (0 mm < ρ < 5 mm). In this interval the analytical solution presents a minimum at roughly 1 mm. However, it must be noted that for low interfiber distances the diffusion approximation may fall since photons do not undergo a sufficient number of scattering event before being detected [3]. For this reason, interfiber distances lower than 5 mm are not considered in the following dissertation.

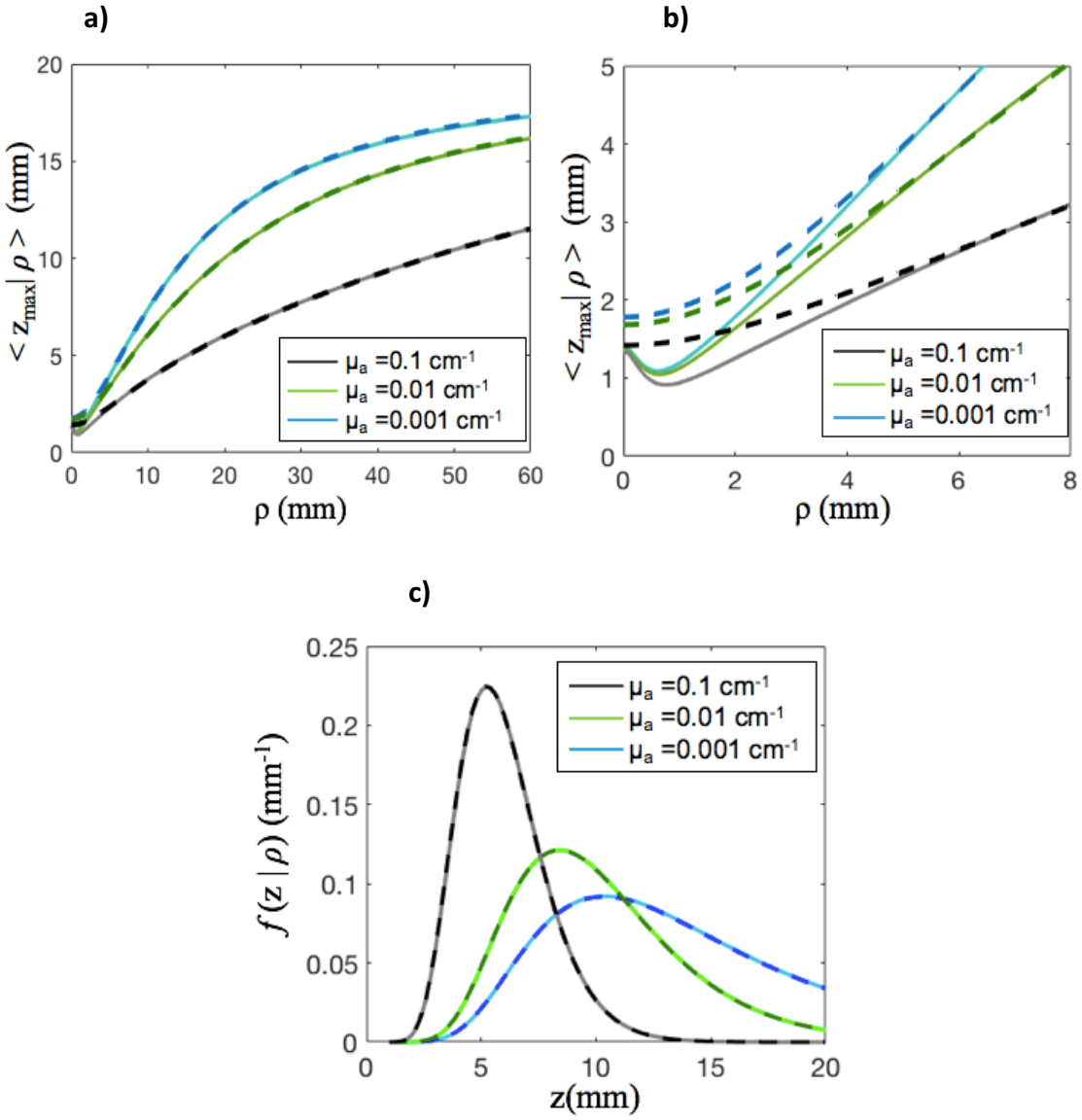

Figure 3.8: f (z | ρ) and ⟨z_{max} | ρ ⟩ for a homogeneous slab of thickness 20 mm, with μ'_s =10 cm^{-1}, n_{int}=n_{out}=1.4. The numerical solutions (dashed lines) are reported for three different values of μ_a and in all cases the agreement with the analytical solution (solid lines) is very good since the curves are superimposed. Panel a) reports ⟨z_{max} | ρ⟩ as a function of ρ. Pane b) is a zoom of panel a) for 0<ρ<8 mm which highlights the differences between numerical and analytical solutions in this range. Panel c) reports f (z | ρ) as a function of z for ρ=10 mm.

We check the validity of the bilayer formula by considering the homogeneous slab of thickness s_0 as composed of two identical slabs each one with thickness s_1=s_2=s_0/2, as we

did in the TD. In Fig. 3.9 we can see the convergence of the two numerical numerical evaluations with the analytical formula for a slab of 40 mm.

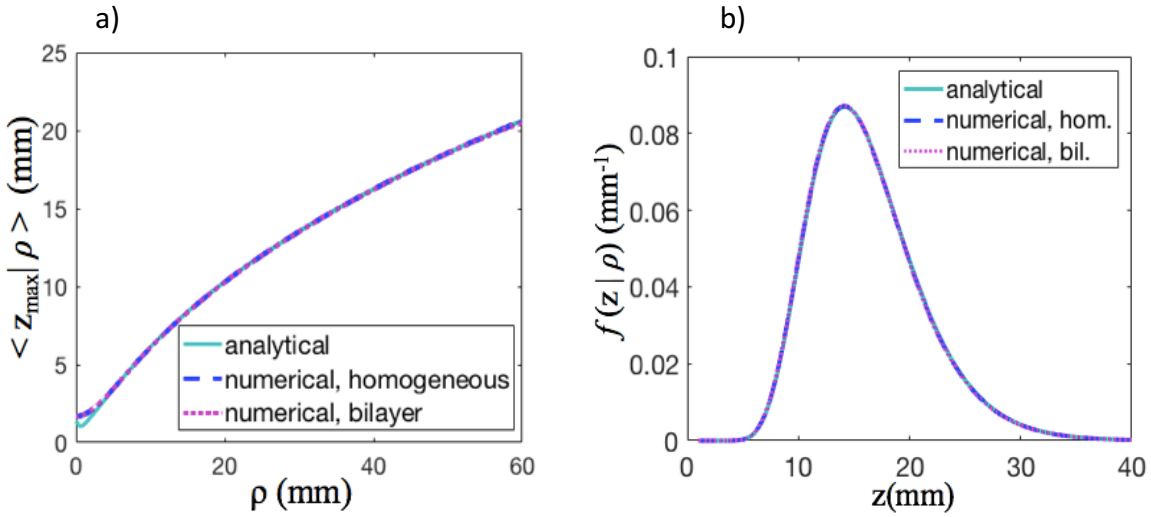

Figure 3.9: $f(z \mid \rho)$ and $\langle z_{max} \mid \rho \rangle$ for a homogeneous slab of thickness 40 mm, with μ'_s =10 cm^{-1}, $n_{int}=n_{out}=1.4$, μ_a =0.1 cm^{-1}. The numerical solutions are calculated using only the homogeneous DE solution (simulated, homogeneous) or considering also bilayer DE solution (simulated, bilayer) and in both cases the agreement with the analytical solution is very good since the curves are superimposed. Panel a) reports $\langle z_{max} \mid \rho \rangle$ as a function of ρ. Panel b) reports $f(z \mid \rho)$ as a function of z for ρ=40 mm.

In conclusion, for both TD and CW domain the developed numerical method works well. In next chapters we will analyze some bilayer configurations of interest in tissue optics and try to understand the behavior of the statistical functions when we vary the optical parameters of the two layers for both TD and CW domain.

Bibliography Chapter 3

[1] T. Zonios, "Investigation of reflectance sampling depth in biological tissues for various co mmon illumination/collection configurations", Journal of Biomedical Optics 19(9), 097001 (2014).

[2] F. Martelli, T. Binzoni, A. Pifferi, L. Spinelli, A. Farina, and A.Torricelli, "There's plenty of light at the bottom: statistics of photon penetration depth in random media", Scientific Reports 6:27057 (2016).

[3] F. Martelli, S. Del Bianco, A. Ismaelli, and G. Zaccanti, "Light Propagation through Biological Tissue and Other Diffusive Media: Theory, Solutions and Software", SPIE Press (2010), Chapter 4 (pag. 58, 74-75) and Chapter 3 (pag. 57-58).

[4] R. C. Haskell, L. O. Svaasand, T. T. Tsay, T. C. Feng, M. McAdams, and B. J. Tromberg, ‘‘Boundary conditions for the diffusion equation in radiative transfer,’’ J. Opt. Soc. Am. A 11, 2727 – 2741 (1994).

[5] A. Kienle and M. S. Patterson, “Improved solution of the steady-state and the time-resolved diffusion equations for reflectance from a semi-infinite turbid medium,” J. Opt. Soc. Am. A 14, 246–524 (1997).

[6] A. Liemert and A. Kienle, "Light diffusion in a turbid cylinder. II. Layered case." Opt. Express 18, 9266–9279 (2010).

CHAPTER 4

Bilayer geometry simulations in TD

The aim of this chapter is to apply the numerical method developed and validated in the previous chapter in order to make a picture of the dependence of the TD probability density function and of the TD mean maximum penetration depth on the physical parameters that characterize a bilayer slab. Since until now literature about photon penetration depth in time domain takes into account only the case of homogeneous slab geometry [1, 2, 3, 4], an important issue is to understand how the bilayer geometry affects the statistics.
One possible application of this study is Neurophotonics. In particular, optical methods like fast optical signal (FOS) [5], diffuse correlation spectroscopy (DCS) [6] and functional near infrared spectroscopy (fNIRS) [7] use red and near infrared light (e.g. 600-900 nm) to noninvasively investigate brain structures and brain functions, and prove to be complementary to existing neuroimaging techniques like electroencephalography, functional magnetic resonance imaging or positron emission tomography. For this reason, we take into account the typical values of optical parameters in human head tissues which are reported in the work by Farina et al. [8].
The chapter is divided into five sections which describe the dependence of photon penetration depth on each parameter of interest, i.e., absorption coefficient, reduced scattering coefficient, interfiber distance, thickness and refractive index. Each section reports simulations done varying only the specified parameter of interest in order to have a clear view about how it affects f and $\langle z_{max} \rangle$.

4.1 Simulations varying the absorption coefficient

In this paragraph the dependence of the probability density function and of the mean maximum penetration depth on the absorption coefficient is inspected.
Before dealing with bilayer simulations it is worth remembering some important concepts about the rule of absorption and scattering coefficients in light propagation through diffusive media. In the model of photon migration, light-matter interaction consists in elastic scattering and absorption. Scattering interaction deflects photons along new directions of propagation while absorption interaction causes the disappearance of photons [9]. In this model the quantity $(\mu_s')^{-1}$ is the transport mean free path, i.e., the mean distance travelled by photons between two consecutive scattering events [9], while $(\mu_a)^{-1}$ is the probability of photon absorption per unit pathlength inside the medium. So μ_a does not affect the mean free path but only the number of photons detected. In this framework the independence of $\langle z_{max} \mid t \rangle$ on μ_a in the homogeneous geometry can be explained as follow. If we take into account two possible photon paths of the same length inside a homogeneous slab (Fig 4.1), the two correspondent photons have the same probability to be absorbed even if they experience a different z_{max}. This means that μ_a does not affect the probability of a photon to have a certain z_{max} and $f(z|t)$ and $\langle z_{max} \mid t \rangle$ do not depend on μ_a.
In the following we will see how this property changes in case of a bilayer slab geometry.

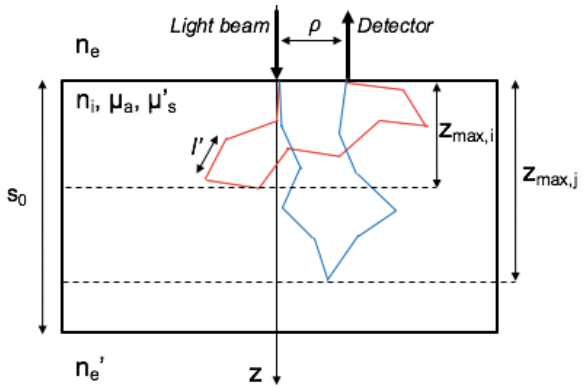

Figure 4.1: Two possible photon path inside a homogeneous slab of thickness s_0 are displayed (red and blue lines). $z_{max,i}$ and $z_{max,j}$ are the respective maximum depth of the two photons. $l'=(\mu_s')^{-1}$ is the mean free path inside the medium.

The geometry of the bilayer structure is represented in Fig. 4.2 together with the parameters used in all the simulations. Varying parameters μ_{a1} and μ_{a2} in the simulations we can highlight their effects on the statistics of photon penetration depth. For each simulation the reduced scattering coefficients of both layers is fixed at 10 cm^{-1}. This value guarantees the validity of the diffusion approximation in our simulations ($\mu_s' \gg \mu_a$) [9] and it is inside the typical range of values found in biological tissues[8]. No refractive index mismatch is taken into account between the outside and the inside of the medium and also between the two layers. The interfiber distance is fixed at 20 mm while the thicknesses s_1 and s_2 are both equal to 20 mm. The ballistic time is $t_0 \cong 100$ ps, so we put to zero the first ten points of reflectance curves and we do not consider them in our analysis.

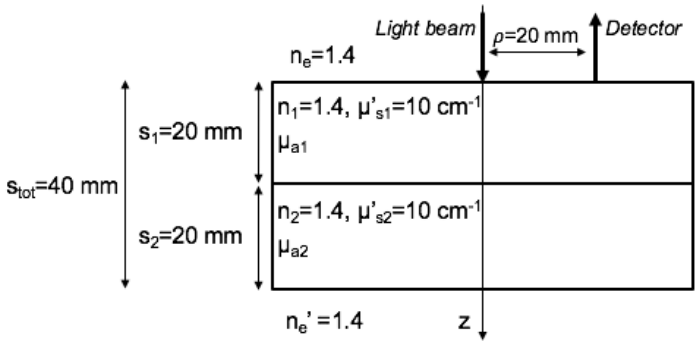

Figure 4.2: Bilayer geometry used in the simulations. Parameters are reported with their corresponding values.

4.1.1 Variation of μ_{a1}

In the first series of simulations we make μ_{a1} vary in the interval [0.05, 0.25] cm^{-1} with a step of 0.05 cm^{-1}, while μ_{a2} is fixed at 0.15 cm^{-1}. This range of values is typical of biological tissue in the near-infrared spectrum [8] which is the most used part of the spectrum for biomedical application. In Fig. 4.3 and 4.4 the numerical evaluated $\langle z_{max} \mid t \rangle$ and $f(z|t)$ are reported. We can see immediately that varying μ_{a1} the profile of $\langle z_{max} \mid t \rangle$ changes a lot. In particular, for t > 2000ps the curves split up with the curve relative to μ_{a1}=0.25 cm^{-1} being the highest and the curve relative to μ_{a1}=0.05 cm^{-1} being the lowest. Indeed, photons penetrate more in the medium as μ_{a1} increases. This behavior can be understood looking at the probability density function at different times. At early times (t<1000 ps) almost all photons detected have their path entirely in the first layer, so $f(z|t)$ does not depend on μ_{a1} as in the homogeneous case (Fig. 4.4a). Increasing the detection time, pathlengths become longer and photons can reach the second layer. In Fig. 4.4 (b and c) we can see that $f(z|t)$ moves toward a greater z as μ_{a1} increases.

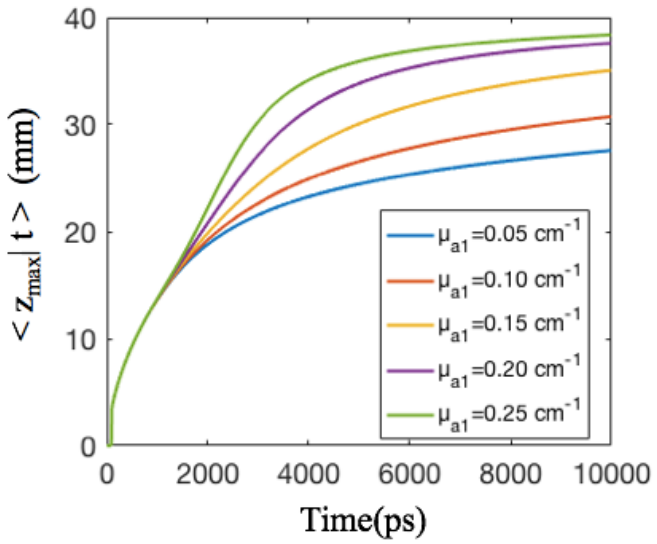

Figure 4.3: $\langle z_{max} \mid t \rangle$ for different values of μ_{a1}. μ_{a2} is fixed at 0.15 cm^{-1} in all five simulations.

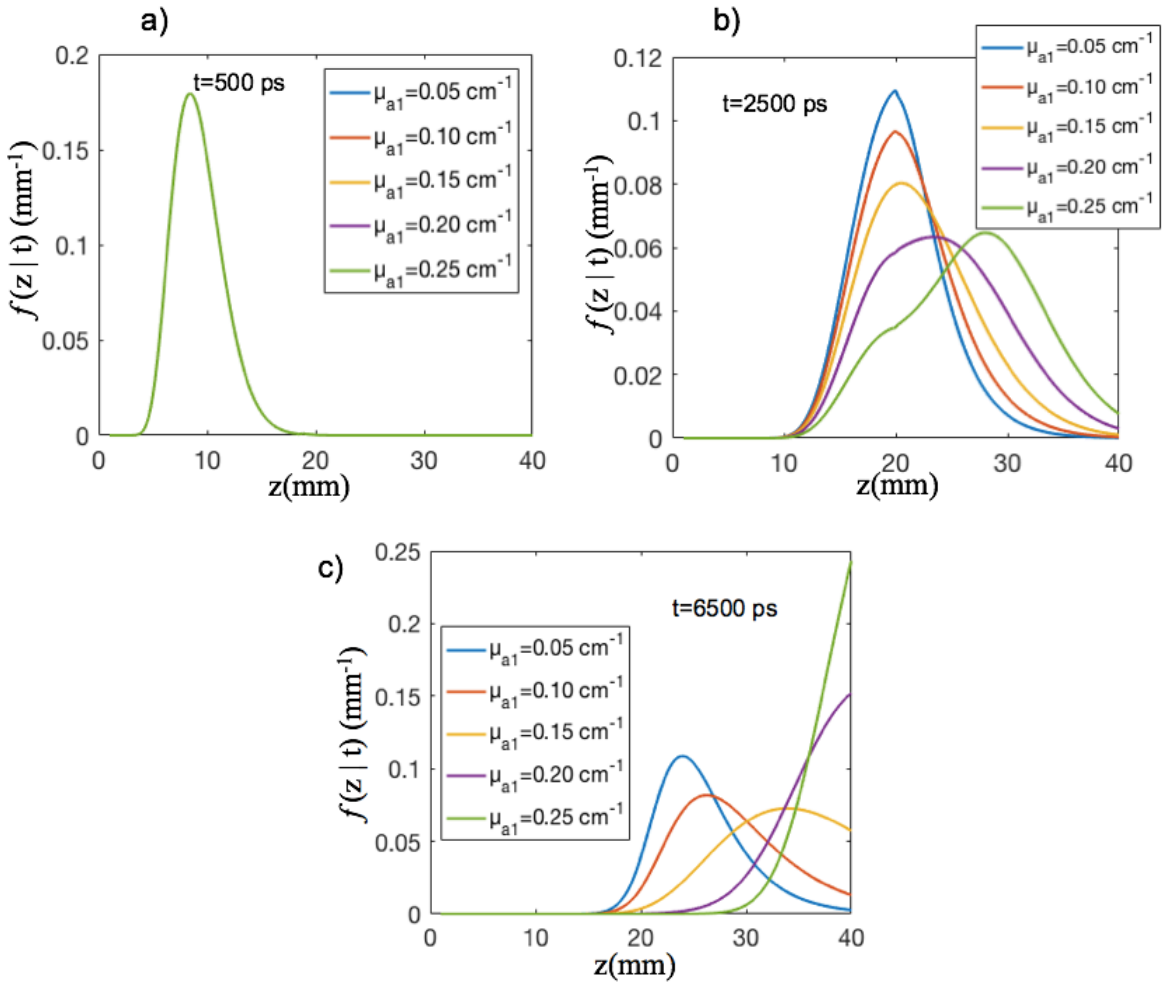

Figure 4.4: f(z|t) relative to different μ_{a1} are reported as a function of z. In panel a) time t=500 ps (early time) and the curves are superimposed. In panel b) and c) detection time is respectively 2500 ps and 6500 ps and the curves split up.

This behavior can be explained within the framework of photon migration model. Fixing the detection time t, all photon paths have the same length $l=vt$ (v is the velocity of light in the medium). Photons which travel a longer distance inside the less absorbing layer have less probability of being absorbed, so they have a higher probability of being detected. If $\mu_{a1} > \mu_{a2}$, photons with longer path inside the the second layer (with a greater z_{max}) are favorite. The corresponding $f(z|t)$ and $\langle z_{max} \mid t \rangle$ move toward a deeper z with respect to the homogeneous case ($\mu_{a1} = \mu_{a2}$). This is the case of μ_{a1}=0.20 cm^{-1} and μ_{a1}=0.25 cm^{-1}. Vice versa, when $\mu_{a2} > \mu_{a1}$, $f(z|t)$ and $\langle z_{max} \mid t \rangle$ move toward a lower z with respect to the homogeneous case. This is the case of μ_{a1}=0.05 cm^{-1} or μ_{a1}=0.10 cm^{-1}. In the intermediate case, μ_{a1}=0.15 cm^{-1}, $f(z|t)$ and $\langle z_{max} \mid t \rangle$ are obviously equal to that of a homogeneous slab of thickness 40 mm and μ_s'=10 cm^{-1}.

4.1.2 Variation of μ_{a2}

In the second series of simulations we make μ_{a2} vary in the interval [0.05, 0.25] cm^{-1} with a step of 0.05 cm^{-1}, while μ_{a1} is fixed at 0.15 cm^{-1}. In Fig. 4.5 the numerical evaluated $\langle z_{max} \mid t \rangle$ and $f(z|t)$ are reported. The results are symmetrical with respect to first series of

simulation. Indeed, when μ_{a2}=0.05 cm^{-1} and μ_{a2}=0.10 cm^{-1}, $f(z|t)$ and $\langle z_{max} \mid t \rangle$ move toward a deeper z with respect to the homogeneous case since $\mu_{a1} > \mu_{a2}$. Vice versa, $f(z|t)$ and $\langle z_{max}|t \rangle$ move toward a lower z in case of μ_{a2}=0.20 cm^{-1} or μ_{a2}=0.25 cm^{-1}, since $\mu_{a2} > \mu_{a1}$. It is worth noting that the results obtained varying μ_{a2} are identical to the results of previous paragraph if $\Delta\mu_a = \mu_{a1} - \mu_{a2}$ is the same. For example, the case with μ_{a2}=0.25 cm^{-1} is equal to the case μ_{a1}=0.05 cm^{-1} in previous paragraph since in both cases we have $\Delta\mu_a$=10 cm^{-1}. This means that the functions $f(z|t)$ and $\langle z_{max} \mid t \rangle$ depend only on $\Delta\mu_a$ and not on the absolute value of μ_a. Indeed, the statistics of photon penetration depth does not change if we add a bias μ_a' in both layers since it increases the absorption of all photons, without any preferences for specific paths.

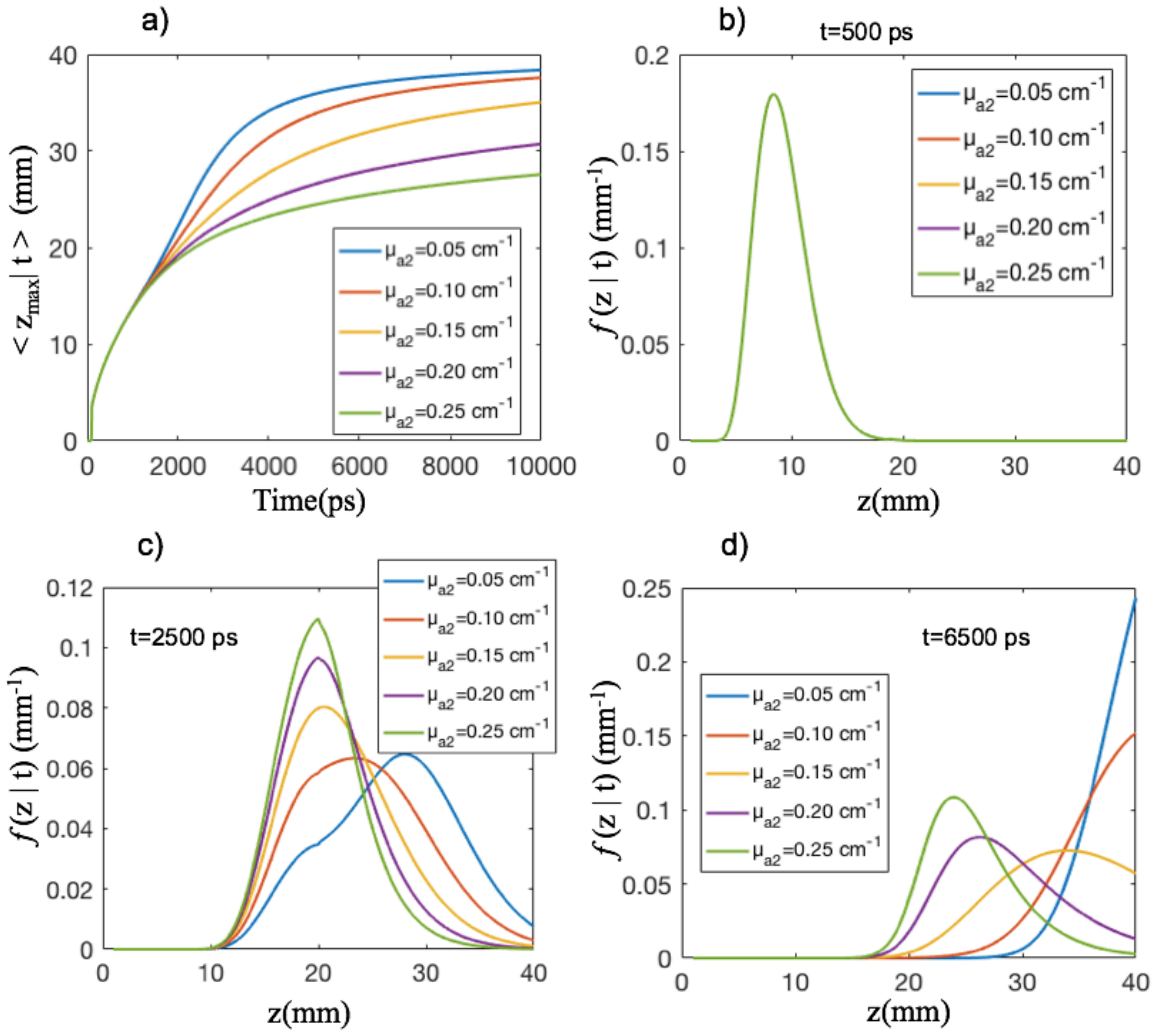

Figure 4.5: $\langle z_{max} \mid t \rangle$ and f(z|t) for different values of μ_{a2}. μ_{a1} is fixed at 0.15 cm^{-1} in all five simulations. In panel a) $\langle z_{max} \mid t \rangle$ is reported. In panels b), c) and d) f(z|t) relative to different μ_{a2} are reported as a function of z. In panel b) detection time t=500 ps (early time) and the curves are superimposed. In panel c) and d) detection time is respectively 2500 ps and 6500 ps and the curves split up.

The effect of a mismatch in the absorption coefficients between the two layers can be better visualized with Fig. 4.6. The two possible photon paths drawn have a different probability of being absorbed since only the blue path goes inside the second layer. If $\mu_{a1} > \mu_{a2}$, the blue path with $z_{max,j} > z_{max,i}$ is favorite and vice versa.

In conclusion, in the bilayer geometry absorption coefficient mismatch between the two layers changes the statistics of photon penetration depth with respect to the homogeneous case since it selectively favors photon path with different z_{max}.

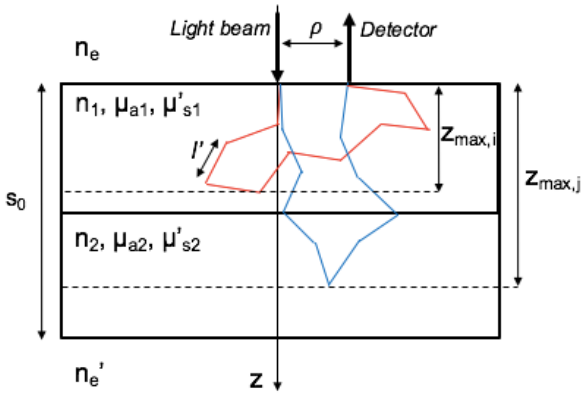

Figure 4.6: Two possible photon path inside a bilayer slab of thickness s_0 are displayed (red and blue lines). $z_{max,i}$ and $z_{max,j}$ are the respective maximum depths of the two photons. $l'=(\mu_s')^{-1}$ is the mean free path inside the medium.

4.1.3 Extreme cases

The effect of $\Delta\mu_a$ on the probability density function can be better understood with the following two extreme cases. The former has μ_{a1}=1 cm^{-1} and μ_{a2}=0 cm^{-1} while the latter has μ_{a1}=0 cm^{-1} and μ_{a2}=1 cm^{-1}. These values of absorption coefficient are obviously unreal for biological tissues but they show us what is the behavior of $f(z|t)$ and $\langle z_{max} \mid t \rangle$ with large $\Delta\mu_a$. All the other parameters have the same values of the previous simulations and they are reported in Fig. 4.2. The behavior of $\langle z_{max} \mid t \rangle$ is in accordance with the previous results as we can see in Fig. 4.7e. When μ_{a1}=1 cm^{-1} and μ_{a2}=0 cm^{-1} photons which have a great pathlength in the second layer are statistically favorites, so $\langle z_{max} \mid t \rangle$ moves toward deeper z. The exact contrary happens in the case μ_{a1}=0 cm^{-1} and μ_{a2}=1 cm^{-1} in which only photons travelling in the first layer can be detected since the others have a great probability to be absorbed. The profile of $f(z|t)$ in these two cases has interesting features. In the former case (Fig. 4.7a) we can see that $f(z|t)$ moves rapidly toward a deeper z since photons are not absorbed in the second layer. At t=1000 ps the profile of the probability density function has two peaks. The first peak is due to photons which stay only in the first layer (z<20 mm), so their statistics is equal to a homogeneous slab. This can be seen in Fig. 4.7c which highlights that the profile of $f(z|t)$ for z<20 mm is equal to that of a homogeneous slab except for a multiplication factor due to normalization. The second peak is inside the second layer and its position is a tradeoff between two factors. On the one hand the absorption probability wants $f(z|t)$ peaked at a deeper z since photons which travel a great path in the second layer are statistically favorites. On the other hand, when time is fixed also pathlength is fixed so z_{max} cannot be too large. This also explain why the second peak moves toward a deeper z as time increases while the first peak disappears since no photon has z_{max}<20 mm. In the latter case (μ_{a1}=0 cm^{-1} and μ_{a2}=1 cm^{-1}) $f(z|t)$ rapidly decreases at z=s_1=20 mm since photons prefers to remain in the first layer as we can see in Fig. 4.7b. As time increases $f(z|t)$ is more and more peaked at the boundary between the two layer.

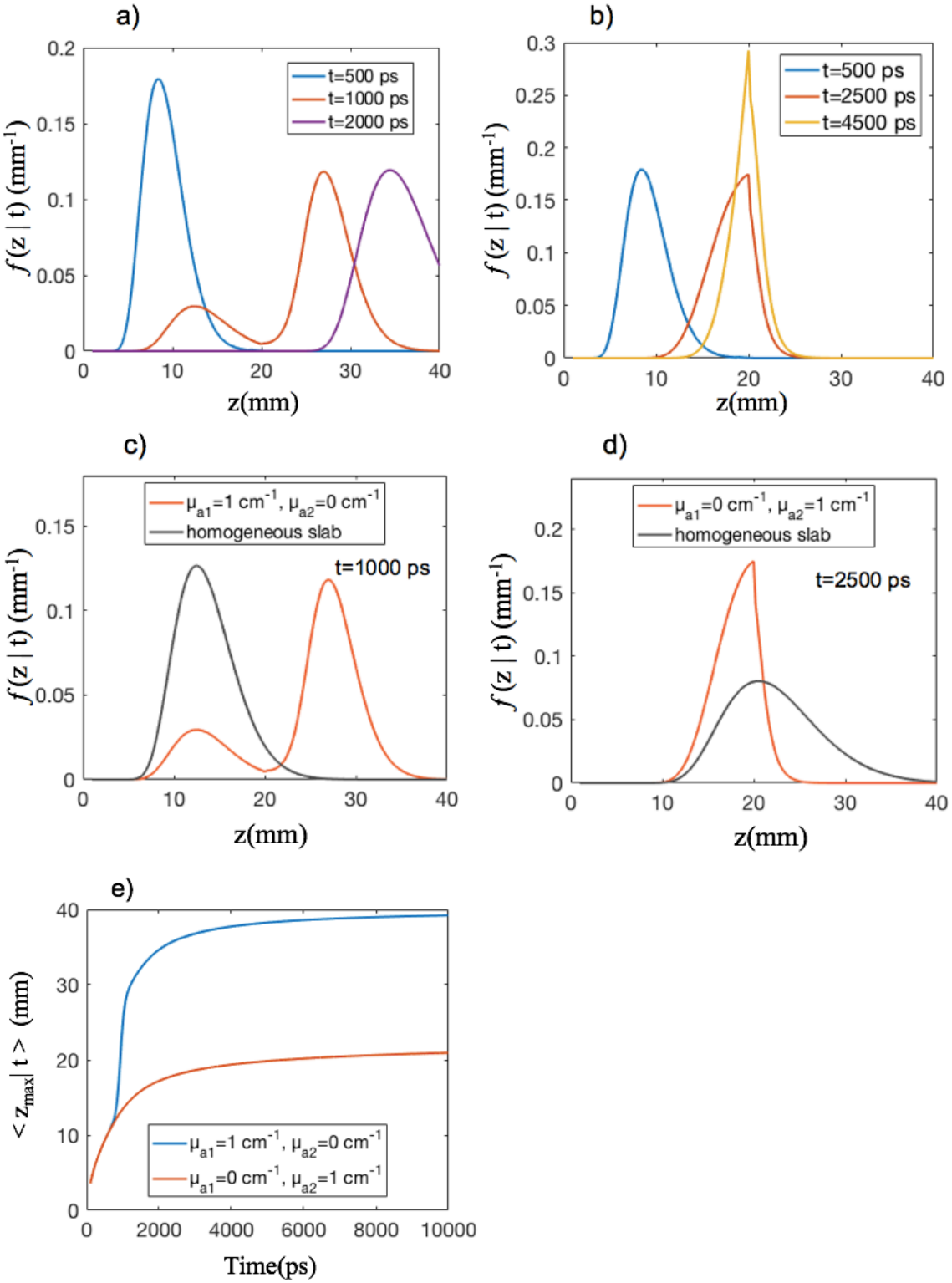

Figure 4.7: f(z|t) and ⟨z_{max} | t⟩ calculated in the two extreme situation. Panels a) and c) refers to the case with μ_{a1}=1 cm^{-1} while panels b) and c) refers to the case with μ_{a2}=1 cm^{-1}. In panels c) and d) a comparison with the homogeneous case is reported. In panel e) ⟨z_{max} | t⟩ for both cases is reported.

This means that photons penetrate little in the second layer and ⟨z_{max} | t⟩ is more or less equal to 20 mm at great time (Fig. 4.7e). Also in this case for z<20 mm *f(z|t)* is equal to the homogeneous case except for a multiplication factor due to normalization (Fig. 4.7d).

Finally, these two configuration can be very interesting for applications. Indeed, in a multilayer geometry the inspection of one specific layer can be done by inducing a much greater absorption coefficient on the others.

4.2 Simulations varying the reduced scattering coefficient

In this paragraph we highlight the effect of the reduced scattering coefficients on the statistics of photon penetration depth.
Before starting our simulations on the bilayer geometry we study the case of the homogeneous slab geometry since the effect of μ'_s has never been inspected in previous works [1, 2, 3, 4]. We calculate $\langle z_{max} \mid t \rangle$ and $f(z|t)$ for different values of μ'_s between 6 cm^{-1} and 14 cm^{-1} (Fig. 4.8). Fixed time t we note that $f(z|t)$ moves toward deeper values of z and its FWHM increases as μ'_s decreases. As a result, $\langle z_{max} \mid t \rangle$ increases.

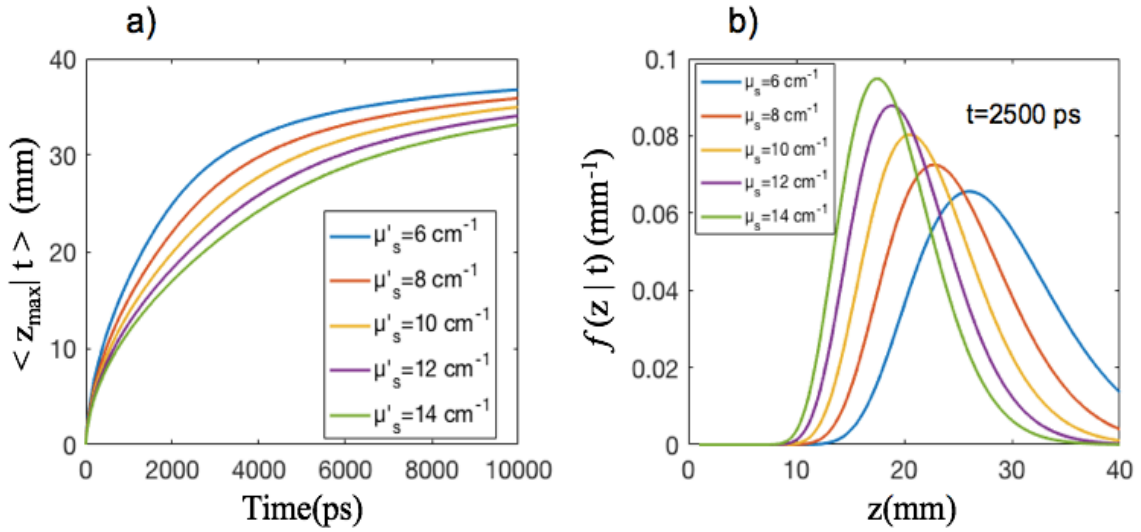

Figure 4.8: $\langle z_{max} \mid t \rangle$ and $f(z|t)$, in panel a) and b) respectively, calculated for a homogeneous slab of thickness 40 mm, $n_{int}=n_{out}=1.4$. The reduced scattering coefficient μ'_s varies between 6 cm^{-1} and 14 cm^{-1}.

The results behavior can be understood remembering that a variation in μ'_s induces a variation on the mean free path $l'=(\mu'_s)^{-1}$. As we can see in Fig. 4.9 if μ'_s decreases the distance between two consecutive scattering events increases and photons are more likely to reach a greater depth. In order to explain this behavior, we can think to the random walk model, which is often used to describe photon movement inside a diffusive media [1, 2, 3] and it produces results really similar to the diffusion model. In this model we have that [1]:

$$< r^2(t) > \propto (l')^2 t/T \qquad (4.1)$$

where r is the distance of the photon from the origin (point *O* in Fig. 4.9) and T is the mean time interval between two scattering events. Thus, if l' increases, photon paths reach great distances from the origin and also a great z_{max} on average.

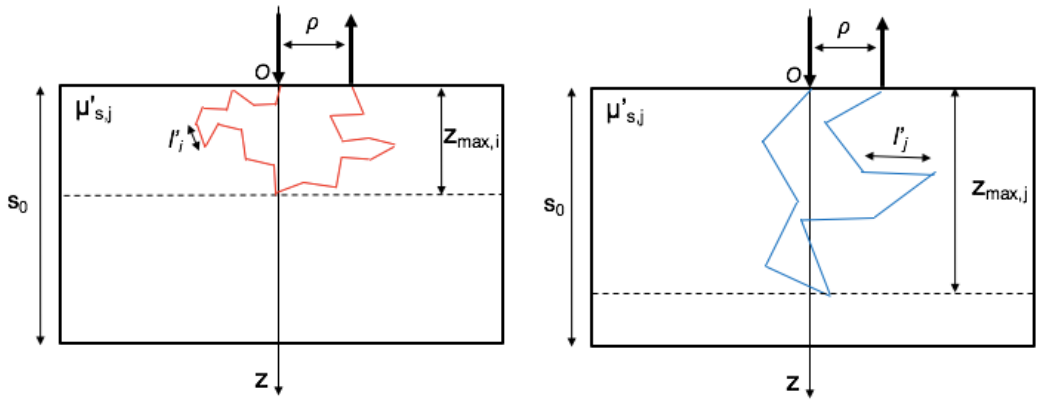

Figure 4.9: Two homogeneous slabs with reduced scattering coefficient $\mu'_{s,i}$ and $\mu'_{s,j}$ are displayed together with two possible photon path inside them (red and blue lines). $z_{max,i}$ and $z_{max,j}$ are the respective maximum depth of the two photons. $l'_i < l'_j$ since $\mu'_{s,i} > \mu'_{s,j}$.

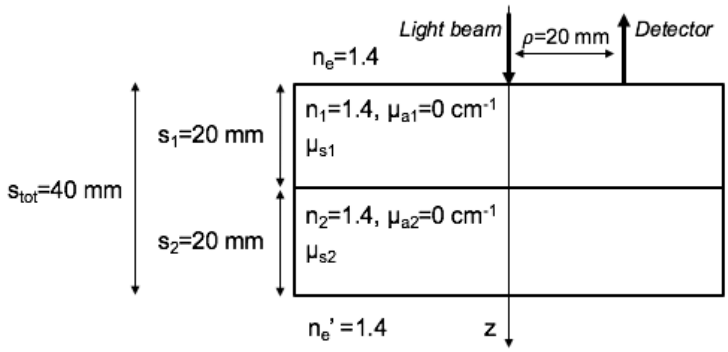

Figure 4.10: Bilayer geometry used in the simulations. Parameters are reported with their corresponding values.

Then, we can consider the usual bilayer geometry with the same parameters used in previous simulations, but now the absorption coefficients are set to zero and the reduced scattering coefficients vary (Fig. 4.10).

4.2.1 Variation of μ'_{s1}

In the first series of simulations we make μ'_{s1} vary in the interval [6, 14] cm^{-1} with a step of 2 cm^{-1}, while μ'_{s2} is fixed at 10 cm^{-1}. These are the typical values of reduced scattering coefficients of head tissues that are reported on the work by Farina et al. [8].
First of all, the behavior of the mean maximum penetration depth is really similar to the homogeneous case. Indeed, $\langle z_{max}|t \rangle$ decreases as μ'_{s1} increases (Fig. 4.11d). The variation of μ'_{s1} affects the statistics at every time since all photons have to travel some distance in the first layer. Furthermore, the profile of the probability density function presents very interesting features. At early times we see a marked jump in $f(z|t)$ at the boundary between the two layers. When $\mu'_{s1} < \mu'_{s2}$, $f(z|t)$ increases at z=20 *mm* and the jump is bigger if $\Delta\mu'_s$ is bigger (Fig. 4.11a). For z<20 *mm* the statistics is equal to a homogeneous slab since photons do not enter in the second layer. But at z=20 mm the mean free path abruptly decreases and photons penetrate with more difficulty in the second layer with respect to the first layer. For this reason, photon paths in second layer remain more confined in the first millimeters. On the other hand, when $\mu'_{s1} > \mu'_{s2}$, $f(z|t)$ decreases at z=20 mm and the jump

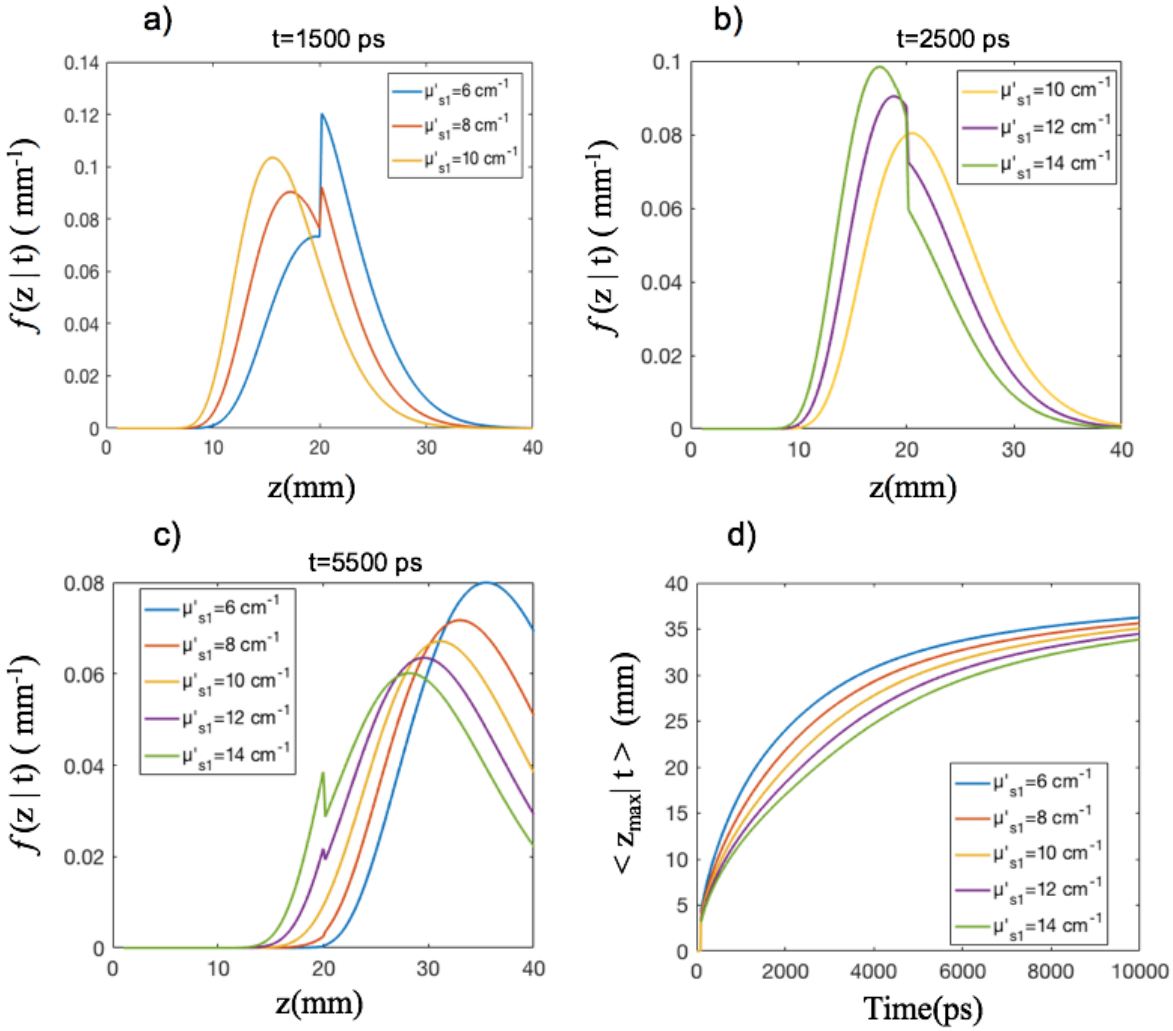

Figure 4.11: f(z|t) and ⟨z_{max} | t⟩ are reported for different values of μ'_{s1}. In panel a), f(z|t) for t=1500 ps in the cases where $\mu'_{s1} < \mu'_{s2}$. In panel b), f(z|t) for t=2500ps in the cases where $\mu'_{s1} > \mu'_{s2}$. In panel c), f(z|t) for t=5500ps for all values of μ'_{s1} tested. In panel d) ⟨z_{max} | t⟩ is reported.

is bigger if $\Delta\mu'_s$ is bigger (Fig. 4.11b). In this case the mean free path abruptly increases at z=20 mm and photons spread more easily in the second layer. Finally, at t=5500 ps almost all photons enter in the second layer as we can see in Fig 4.11c. However, as μ'_{s1} increases photons need more time to arrive at the second layer and they stay less time inside it. Thus, *f(z|t)* goes toward a lower z as μ'_{s1} increases.
These features can be better understood in the next series of simulations in which μ'_{s2} varies.

4.2.2 Variation of μ'_{s2}

In the second series of simulations we make μ'_{s2} varies in the interval [6, 14] cm^{-1} with a step of 2 cm^{-1}, while μ'_{s1} is fixed at 10 cm^{-1}. In Fig. 4.12 the main results are reported.
At t=2500 ps we see the same discontinuity in the probability density function observed also in previous simulations (Fig. 4.12 a and b). *f(z|t)* abruptly decreases at z=20 mm when $\mu'_{s2} < \mu'_{s1}$, while it increases when $\mu'_{s2} > \mu'_{s1}$.

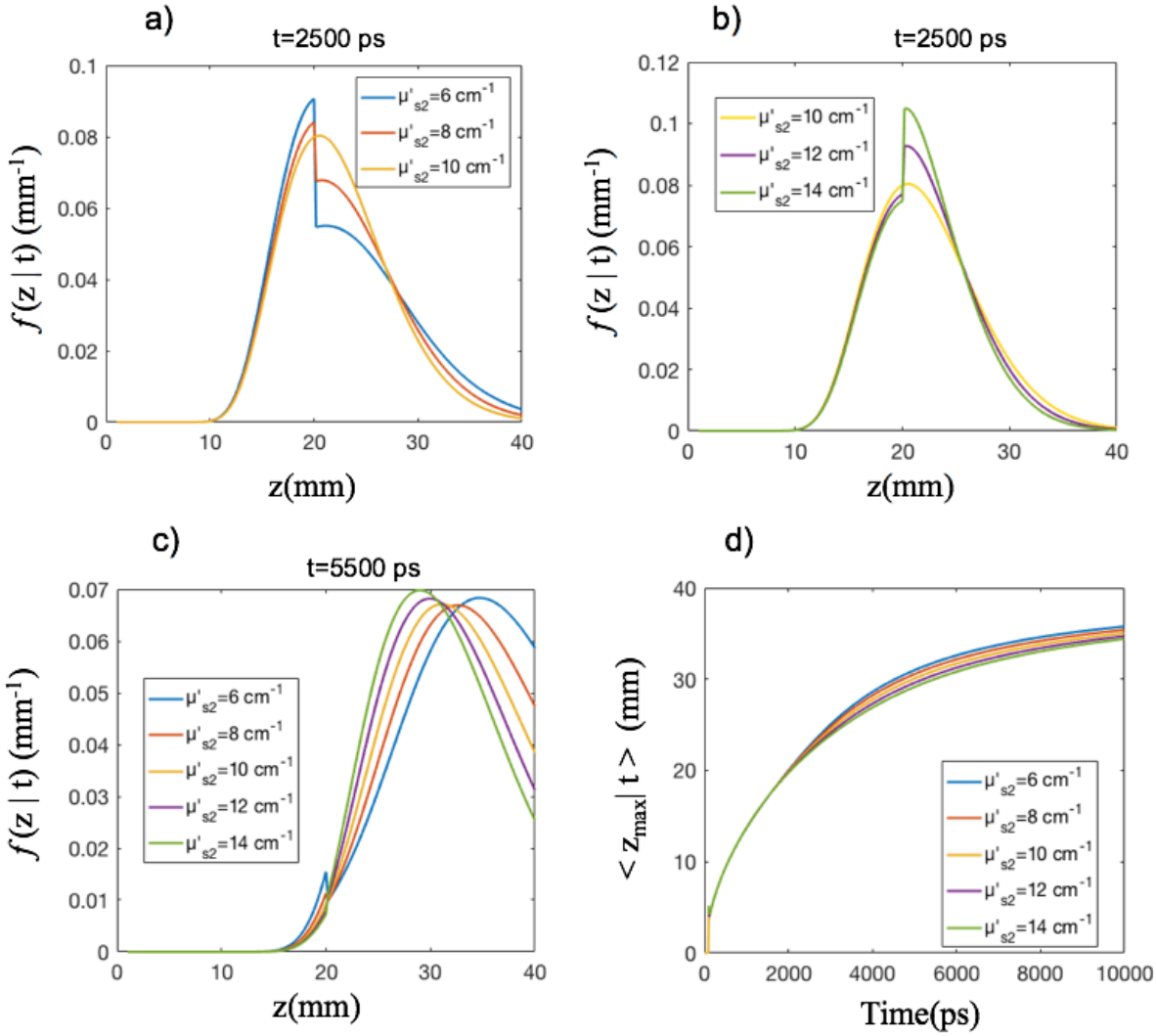

Figure 4.12: f(z|t) and ⟨z_{max} | t⟩ are reported for different values of μ'$_{s2}$. In panel a), f(z|t) for t=2500 ps in the cases where μ'$_{s1}$> μ'$_{s2}$. In panel b), f(z|t) for t=2500 ps in the cases where μ'$_{s1}$< μ'$_{s2}$. In panel c), f(z|t) for t=5500 ps for all values of μ'$_{s1}$ tested. In panel d) ⟨z_{max} | t⟩ is reported.

Figures 4.12a and 4.12b highlight also an interesting comparison with the homogeneous slab with μ'_s=10 cm^{-1} (yellow curve). If $\mu'_{s2}<\mu'_{s1}$=10 cm^{-1} photons make less scattering events in the second layer and they spread more easily in deeper z, so *f(z|t)* is lower than the homogeneous curve in the first millimeters of the second layer but it decreases less rapidly. On the other hand, if $\mu'_{s2}>\mu'_{s1}$=10 cm^{-1} photons make more scattering events in the second layer and they penetrate less deeply, so *f(z|t)* is higher than the homogeneous curve in the first millimeters of the second layer but it decreases more rapidly. At higher times (Fig. 4.12c), when all photons enter in the second layer, *f(z|t)* goes toward deeper values of z as μ'_{s2} decreases. Finally, in Fig 4.12d we can see that the differences in ⟨z_{max}|*t*⟩ are less significant than in Fig. 4.11d and they start at z=20 mm, when photons begin to penetrate in the second layer.

4.2.3 Extreme cases

In the last series of simulations, we add two extreme configurations with high value for the reduced scattering coefficient of the second layer. The aim of these simulations is to understand if our explanations to previous results are solid. The two configurations tested in this section are: μ'_{s2}=100 cm^{-1} and μ'_{s2}=1000 cm^{-1}. μ'_{s1} is fixed to 10 cm^{-1}. In Fig. 4.13 and 4.14 the results for $f(z|t)$ and $\langle z_{max}|t\rangle$ are reported together with the solutions to the homogeneous slab with μ'_s=10 cm^{-1} (blu curves).

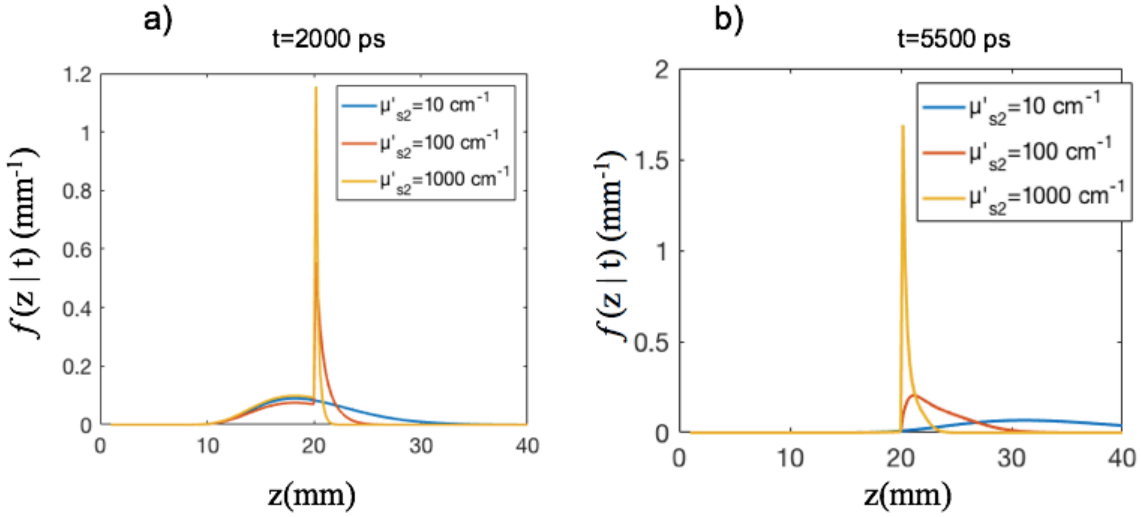

Figure 4.13: $f(z|t)$ calculated for μ'_{s2}=10 cm^{-1}, μ'_{s2}=100 cm^{-1} and μ'_{s2}=1000 cm^{-1} while μ'_{s1} is fixed to 10 cm^{-1}. In panel a) t=2000 ps, in panel b) t=5500 ps.

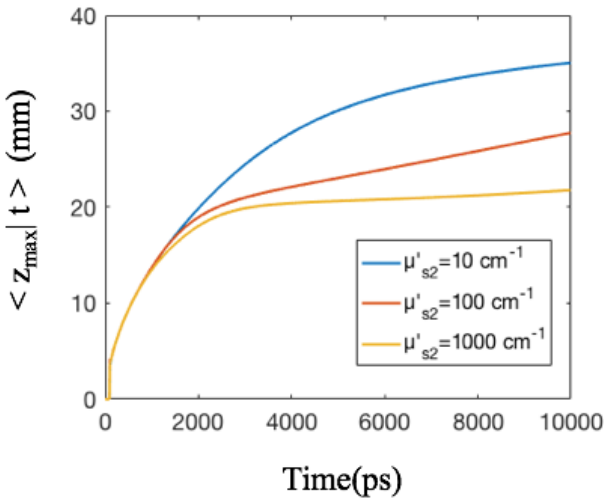

Figure 4.14: $\langle z_{max} \mid t\rangle$ calculated for μ'_{s2}=10 cm^{-1}, μ'_{s2}=100 cm^{-1} and μ'_{s2}=1000 cm^{-1} while μ'_{s1} is fixed to 10 cm^{-1}.

In Fig. 4.13a we can note that the profile of the probability density functions at t=2000 ps is identical to the homogeneous case for z<20 mm but it differs a lot for z>20 mm. Indeed, in these two extreme cases $f(z|t)$ is highly peaked in the first millimeters of the second layer. Also at t=5500 ps, when all photons enter in the second layer, the value of $f(z|t)$ is high only in the first millimeters of the second layer (Fig. 4.13b). As a result, $\langle z_{max}|t\rangle$ decreases its slope after 2000 ps, when it reaches the value of 20 mm (Fig. 4.14). This is in accordance with what has been already said. When μ'_{s2} is very high, photons that enter in the second

layer undergo a very high number of scattering events and they do not penetrate in depth. Thus, a high value of reduced scattering coefficient makes photon penetration really difficult. For this reason, the probability density function is peaked in the first millimeters of the high scattering medium. It is worth noting that there is not a "mirror effect" at the boundary between the two layer since photons penetrate in the second layer without any reflections.

4.3 Simulations varying the interfiber distance

In this section simulations are done varying the interfiber distance ρ. We test three values of interfiber distance: $\rho = 10\,mm$, $\rho = 20\,mm$ and $\rho = 30\,mm$. The geometry used is showed in Fig. 4.15 together with its parameters. Reduced scattering coefficients and absorption coefficients are picked inside the typical range of values of head tissues [8]. As usual, we do not consider time values lower than the ballistic time $t_0 = \rho/v$ [9]. Moreover, refractive index mismatches are not considered. Thus, no reflections occur at the interfaces with the external medium and between the two layers.

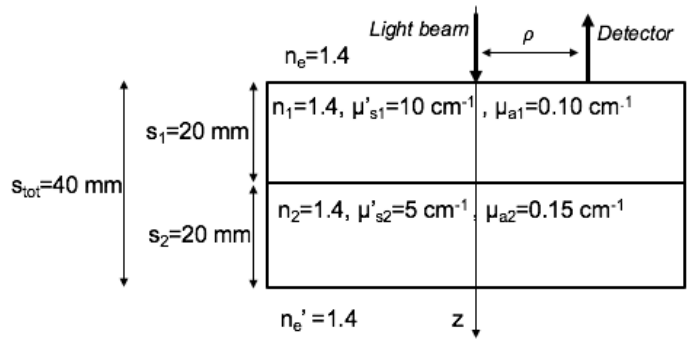

Figure 4.15: Bilayer geometry used in the simulations. Parameters are reported with their corresponding values.

The numerically evaluated curves of $f(z|t)$ and $\langle z_{max}|t\rangle$ can be seen in in Fig. 4.16 and 4.17. It must be noted that there are not significant differences between the curves calculated with different values of ρ. Thus, the statistics of photon penetration depth is not influenced by the interfiber distance. Contrary to the homogeneous slab geometry this is not a property valid in general but it holds for the sets of parameters used.

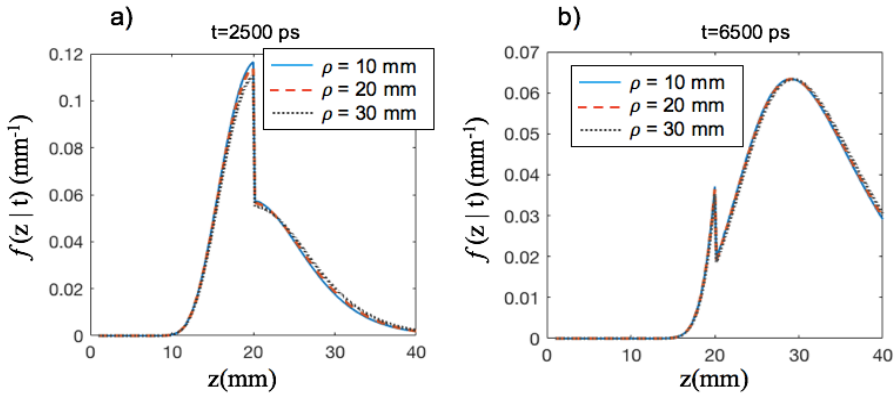

Figure 4.16: f(z|t) for the considered geometry (Fig.4.15) with ρ=10 mm, ρ =20 mm and ρ =30 mm. In panel a) t=2500 ps, in panel b) t=6500 ps.

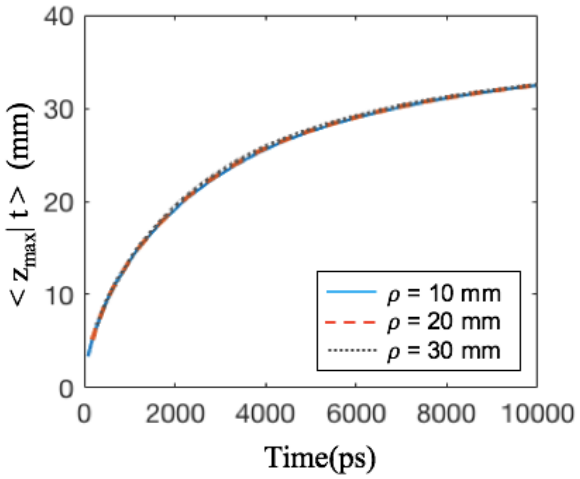

Figure 4.17: $\langle z_{max} \mid t \rangle$ for the considered geometry (Fig.4.15) with ρ=1 0 mm, ρ =20 mm and ρ =30 mm.

4.4 Simulations varying the thicknesses

In this section we study the effects induced by changing the thicknesses of the first and the second layer, s_1 and s_2 respectively. Since biological tissue layers do not have a fixed thickness, it would be interesting to know how a variation of this quantity affects the statistics of photon penetration depth.
In all the simulations we test a bilayer slab of total thickness s_{tot}=40 mm and we vary s_1 in the interval [5, 35] mm with a step of 5 mm (with s_2= s_{tot}-s_1, see Fig. 4.18). In order to better understand these effects, we divide this paragraph in two subsections. In the former we consider a reduced scattering coefficient mismatch between the two layers while in the latter we have an absorption coefficient mismatch.

4.4.1 Simulations with reduced scattering coefficient mismatch

In these simulations we fixed absorption coefficients at 0.10 cm^{-1} while we consider a reduced scattering coefficient mismatch. In the first group of simulations we use μ'_{s1}=5 cm^{-1} and μ'_{s2}=10 cm^{-1}. In the second group of simulations we have the opposite situation, i.e., μ'_{s1}=10 cm^{-1} and μ'_{s2}=5 cm^{-1}. All the parameters used are reported in Fig. 4.18. We start dealing with the first group of simulations whose results can be seen in Fig. 4.19. For each configuration we report three curves of the probability density function relative to different times. $f(z|t)$ moves toward a greater z as time increases. We note that $f(z|t)$ always increases at the interface between the two layers since $\mu'_{s2}>\mu'_{s1}$. The early time curve is peaked at about 8 mm, the middle time curve is peaked at about 20 mm and the late time curve is peaked at about 30 mm. Thus, as s_1 increases the curves pass from being centered in the second layer to being centered in the first layer. Moreover, the curves become wider and centered at a greater z when they pass in the first layer since it is less scattering. For example, the bell shape curve relative to t=1500 ps is entirely positioned in

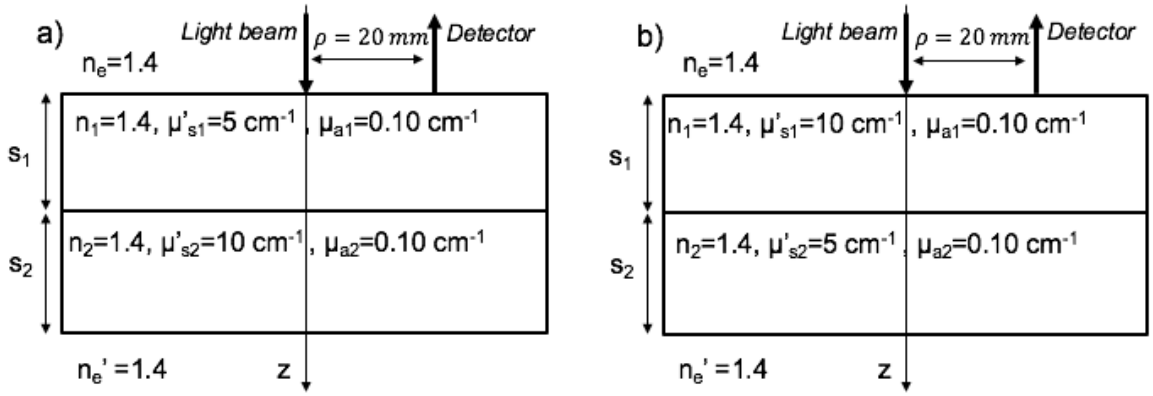

Figure 4.18: Bilayer geometry used in the simulations. Parameters are reported with their corresponding values while s_1 and s_2 changes in the simulations. Panel a) refers to the first group of simulations, while panel b) refers to the second group of simulations.

the second layer when s_1=5 mm (Fig.4.19a) while it is positioned in the first layer when s_1=35 mm (Fig.4.19g). Its peak position passes from z=17.5 mm to z=21 mm.

In Fig. 4.19h we can see the mean maximum penetration depth calculated for all seven cases. The figure highlights that z_{max} of photons increases as s_1 increases. This is in accordance with the model already used to explain previous simulations. Indeed, when s_1 increases photons travels a greater distance in the less scattering layer and they penetrate more easily in the medium. As a consequence, $\langle z_{max}|t\rangle$ increases.

In the second group of simulations the reduced scattering coefficients are exchanged. Results for *f(z|t)* and $\langle z_{max}|t\rangle$ can be seen in Fig. 4.20. *f(z|t)* is plotted at three different times as a function of z. Contrary to the first group *f(z|t)* always decreases at the interface between the two layers since $\mu'_{s1}>\mu'_{s2}$. The variation of s_1 produces an effect opposite to the previous case. Thus, the curves become narrower and centered at a lower z when they pass in the first layer since it is more scattering. For example, the peak position of the curve relative to t=1500 ps passes from z=19 mm to z=16 mm and its FWHM decreases. In Fig. 4.20h we can see the mean maximum penetration depth calculated for all seven cases. In this case we have that $\langle z_{max}|t\rangle$ decreases as s_1 increases. Indeed, when the thickness of the first layer increases photons travels a greater distance in the more scattering layer and their penetration inside the medium is favored.

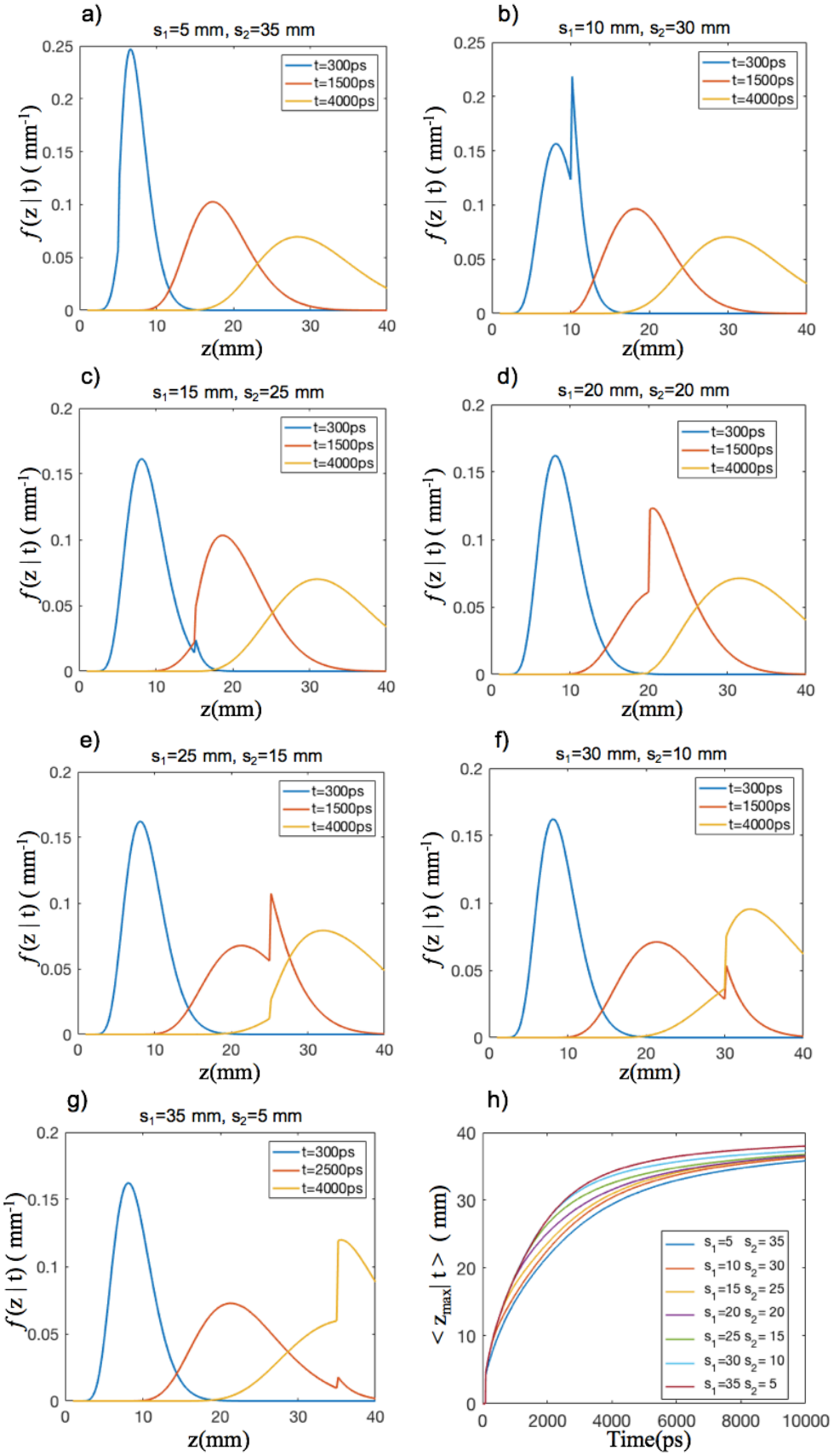

Figure 4.19: f(z|t) and ⟨z_{max} | t⟩ are reported for different values of s_1, with μ'_{s1}=5 cm^{-1} μ'_{s2}=10 cm^{-1} and μ_{a1}=μ_{a2}=0.10 cm^{-1}. From panel a) to panel g) the functions f(z|t) are reported for t=300ps, t=1500 ps and t=4000 ps. In panel h) ⟨z_{max} | t⟩ is reported for all thicknesses tested and the values in its legend are expressed in millimeters.

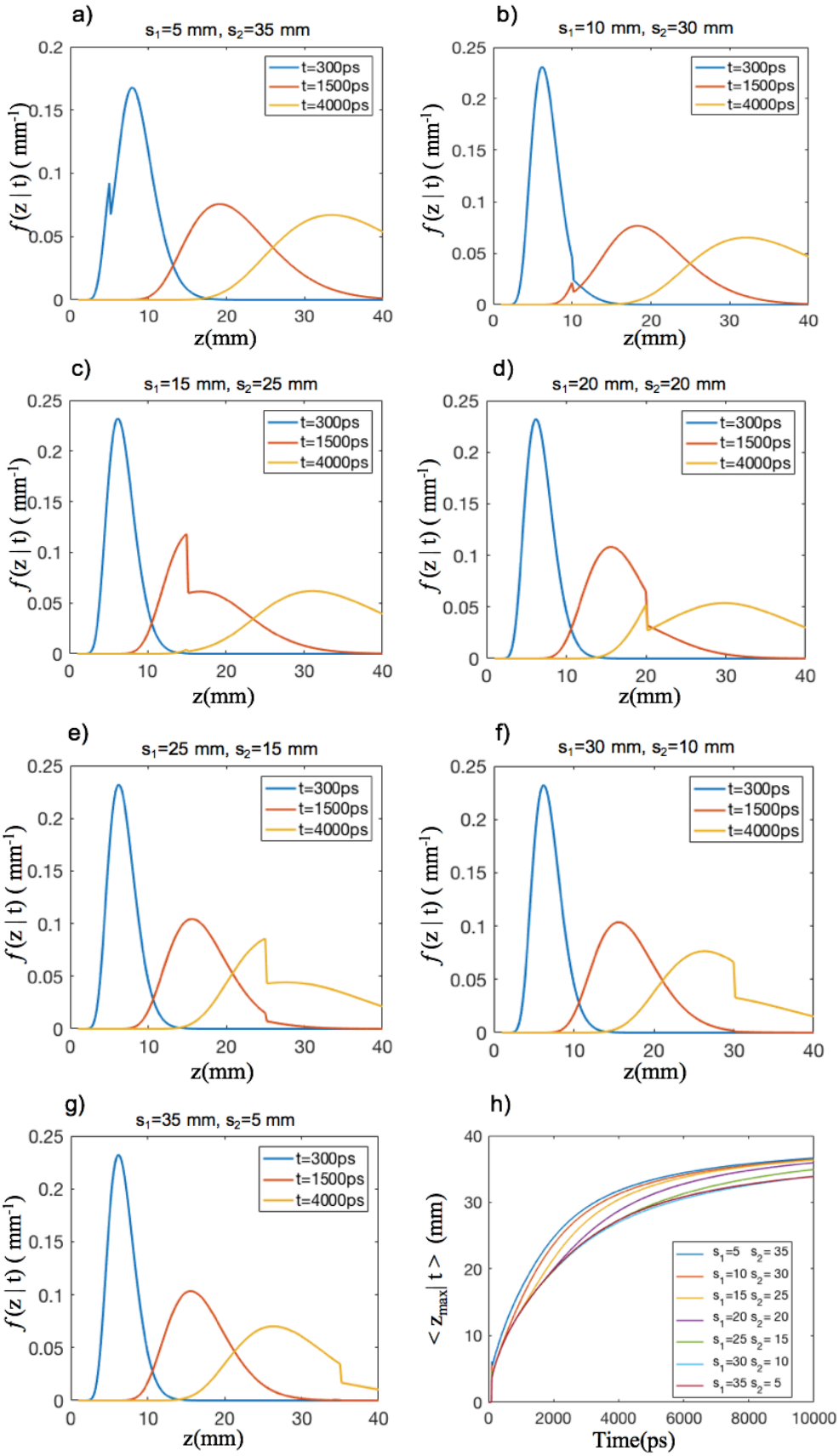

Figure 4.20: f(z|t) and ⟨z_{max} | t⟩ are reported for different values of s_1, with μ'_{s1}=10 cm^{-1} μ'_{s2}=5 cm^{-1} and $\mu_{a1}=\mu_{a2}$=0.10 cm^{-1}. From panel a) to panel g) the functions f(z|t) are reported for t=300 ps, t=1500 ps and t=4000 ps. In panel h) ⟨z_{max} | t⟩ is reported for all thicknesses tested and the values in its legend are expressed in millimeters.

4.4.1 Simulations with absorption coefficient mismatch

In these simulations we fixed reduced scattering coefficients, $\mu'_{s1}= \mu'_{s2}$=10 cm^{-1}, while we consider a reduced scattering coefficient mismatch. In the first group of simulations we use μ_{a1}=0.10 cm^{-1} and μ_{a2}=0.20 cm^{-1}. In the second group of simulations we have the opposite configuration, i.e., μ_{a1}=0.20 cm^{-1} and μ_{a2}=0.10 cm^{-1}. All the parameters used are reported in Fig. 4.21.

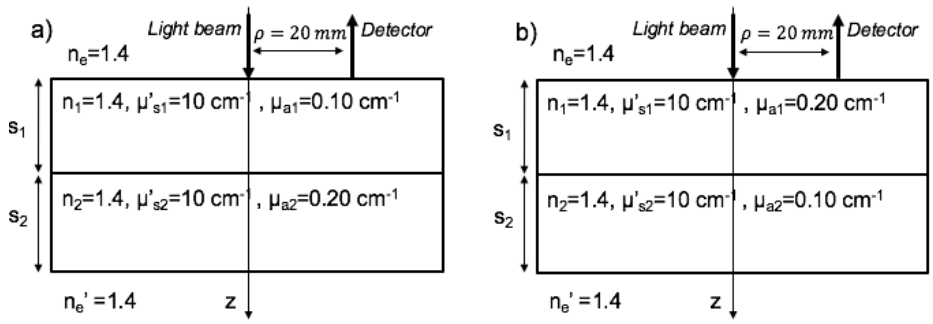

Figure 4.21: Bilayer geometry used in the simulations. Parameters are reported with their corresponding values while s_1 and s_2 changes in the simulations. Panel a) refers to the first group of simulations, while panel b) refers to the second group of simulations.

The results relative to the first group of simulations are reported in Fig. 4.22. It must be highlighted that the case with s_1=5 mm is similar to the case with s_1=35 mm. All the other intermediate cases have a lower $\langle z_{max}|t\rangle$ (Fig.4.22a). Indeed, the two extreme cases are similar to a homogeneous slab with μ'_s=*10 cm*$^{-1}$ since photons stay almost always in the second layer when s_1=5 mm and they stay only in the first layer when s_1=35 mm. This is confirmed by the behavior of the probability density function (Fig. 4.22b). The profile of *f(z|t)* for the two extreme cases is similar to the homogeneous case while if we take into account the case with s_1=15 mm we have that *f(z|t)* is peaked on a lower z. The reason for this is that photons which travels a greater distance in the less absorbing layer (first layer) are statistically favorite. Obviously, these photons have a lower z_{max} on average since they travel less in the deeper layer.

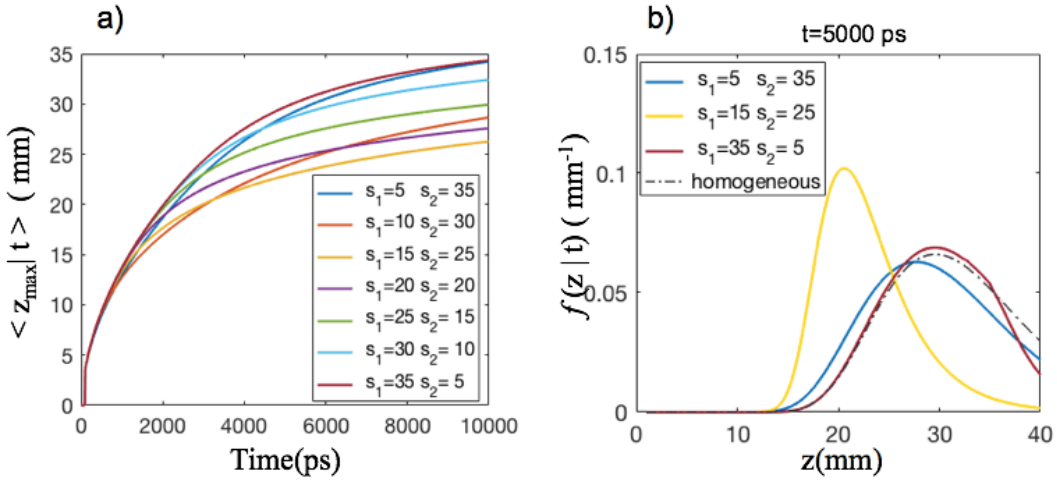

Figure 4.22: f(z|t) and $\langle z_{max} | t\rangle$ are reported for different values of s_1, with μ_{a1}=0.1 cm^{-1} μ_{a2}=0.2 cm^{-1} and $\mu'_{s1}=\mu'_{s2}$=10 cm^{-1}. In panel a) $\langle z_{max} | t\rangle$ is reported for all thicknesses tested. In panel b) f(z|t) at t=5000 ps is reported for three thicknesses tested and also in the homogeneous case. The values in legends are expressed in millimeters.

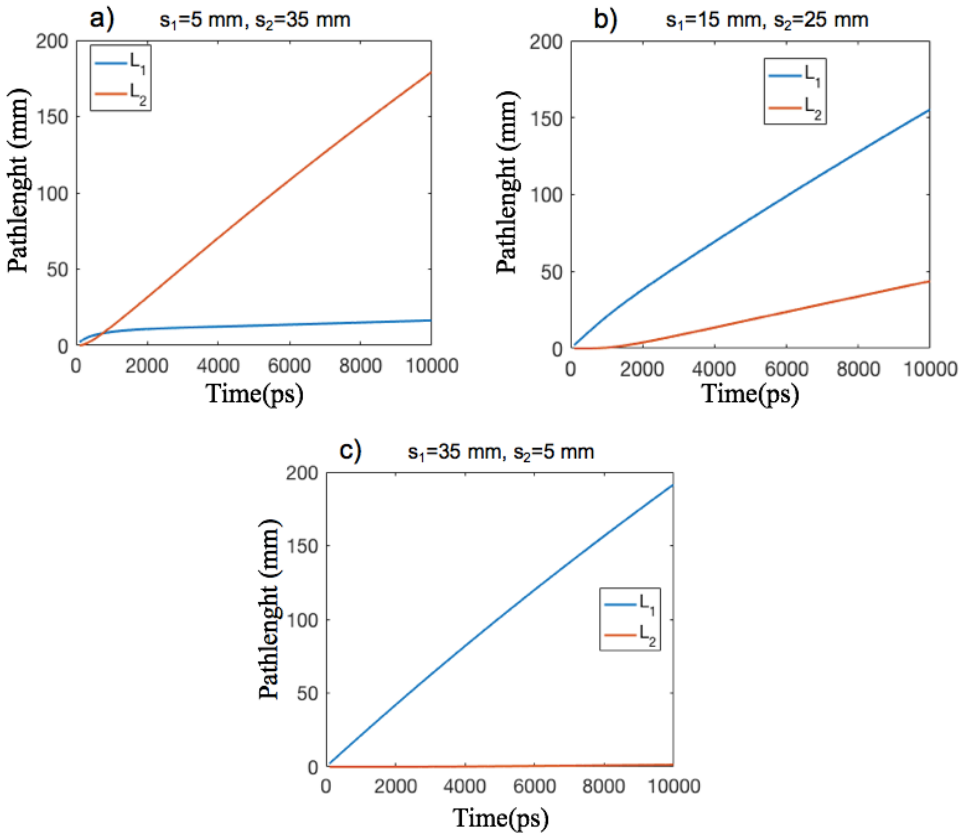

Figure 4.23: Time-dependent mean partial pathlength are reported for layer 1 (L_1) and layer 2 (L_2). The case with s_1=5 mm is in panel a), the case with s_1=15 mm is in panel b) and the case with s_1=35 mm is in panel c).

We can justify this way of thinking looking at the time-dependent mean partial pathlength, $L_j(t)$, i.e., the pathlength traveled in layer j by photons detected at time t. $L_j(t)$ can be written in the following way [10]:

$$L_j(t) = -\frac{1}{R_0(t)}\frac{\partial R_0(t)}{\partial \mu_{a,j}} \tag{4.1}$$

where $R_0(t)$ is the total reflectance curve of the bilayer slab and $\mu_{a,j}$ is the absorption coefficient of layer j. Implementing this formula on Matlab we can find the pathlength travelled in the first and in the second layer by all photons detected, i.e., $L_1(t)$ and $L_2(t)$ respectively. In Fig. 4.23 we can see $L_1(t)$ and $L_2(t)$ for three configurations. When s_1=5 mm the mean partial pathlength in layer 1 is very low so all photons enter in layer 2. On the other hand, when s_1=35 mm the mean partial pathlength in layer 2 is equal to zero so photons do not enter in layer 2. As a result, in these two extreme cases the statistics of photon penetration depth is similar to that of a homogeneous slab. In the intermediate cases the pathlength in each layer is not negligible. Indeed, increasing the thickness of the first layer, $L_1(t)$ increases while $L_2(t)$ decreases. In these cases the statistics is affected by the variation of the absorption coefficient as already said.

The results relative to the second group of simulations are reported in Fig. 4.24. As in the previous simulations, the case with s_1=5 mm is similar to the case with s_1=35 mm. However, this time all the other intermediate cases have a greater $\langle z_{max}|t\rangle$ (Fig.4.24a). The

profile of $f(z|t)$ for the two extreme cases is similar to the homogeneous case while if we take into account the case with s_1=15 mm we have that $f(z|t)$ is peaked on a greater z.

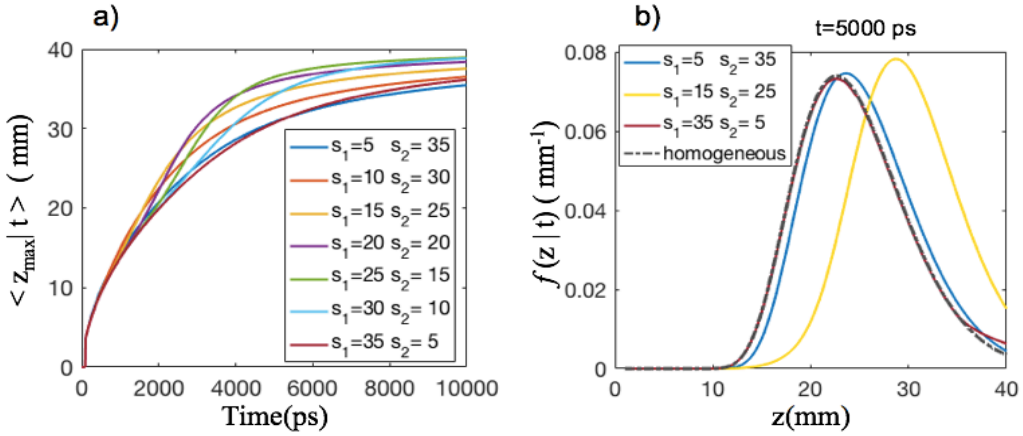

Figure 4.24: $f(z|t)$ and $\langle z_{max} | t \rangle$ are reported for different values of s_1, with μ_{a1}=0.2 cm^{-1} μ_{a2}=0.1 cm^{-1} and $\mu'_{s1}=\mu'_{s2}$=10 cm^{-1}. In panel a) $\langle z_{max} | t \rangle$ is reported for all thicknesses tested. In panel b) $f(z|t)$ at t=5000 ps is reported for three thicknesses tested and also in the homogeneous case. The values in legends are expressed in millimeters.

In Fig. 4.25 we can see $L_1(t)$ and $L_2(t)$ for three different configurations. The considerations presented for the first group of simulations holds also for the second group. However, if we compare Fig. 4.23b and Fig. 4.25b we note that $L_2(t)$ increases more rapidly in the latter. This is in accordance with our interpretation of the results. Since $\mu_{a1}>\mu_{a2}$, photons with longer pathlength in the second layer are statistically favorite. This is the contrary of what happens in the first group and this can be clearly seen in Fig. 4.26 in which we can note that $L_1(t)$ is much lower in the second case when $\mu_{a1}>\mu_{a2}$.

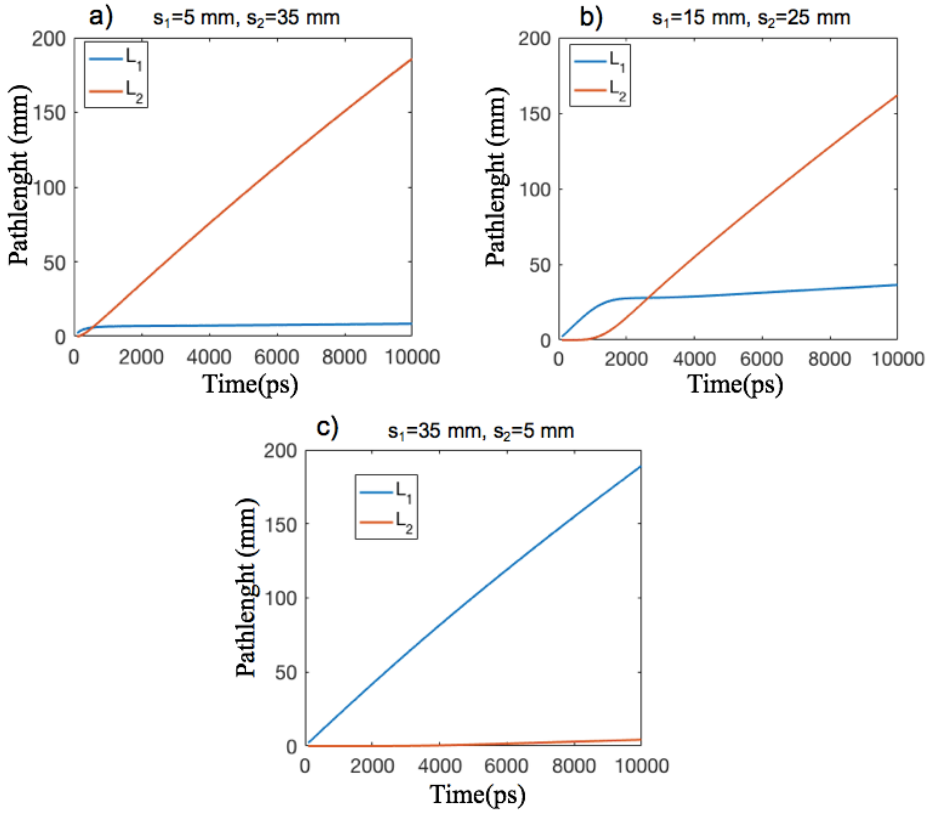

Figure 4.25: Time-dependent mean partial pathlength are reported for layer 1 (L_1) and layer 2 (L_2). In panel a) the case with s_1=5 mm. In panel b) the case with s_1=15 mm. In panel c) the case with s_1=35 mm.

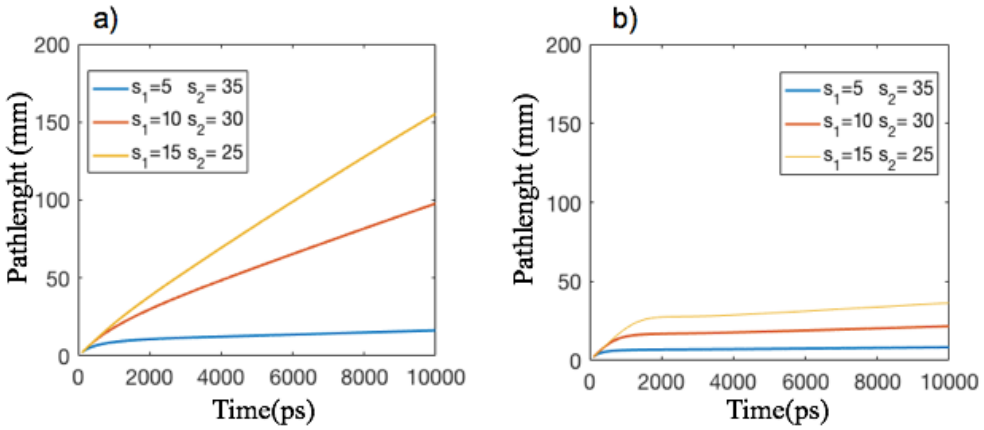

Figure 4.26: Time-dependent mean partial pathlength of layer 1 are reported for s_1=5 mm, s_1=10 mm and s_1=15 mm. The case with μ_{a1}=0.1 cm^{-1} μ_{a2}=0.2 cm^{-1}is reported in panel a) while the case with μ_{a1}=0.2 cm^{-1} μ_{a2}=0.1 cm^{-1} is reported in panel b).

In conclusion, all simulations done varying s_1 and s_2 are very useful for the comprehension of the photon penetration depth in real cases in which thicknesses are not always fixed. In the next paragraph we will introduce a refractive index mismatch in order to consider some real configurations.

4.5 Simulations varying the refractive indexes

Different types of biological tissue show different values of refractive index n, for instance 1.39 (muscle) and 1.45 (normal adipose tissue) [11]. The refractive index mismatches on a macroscopic scale, e.g., between fat and muscle or between skin and skull, determine reflection of light. These differences of the refractive index of different tissue types are usually neglected and n is then considered for most tissues a constant value around 1.4, which is the typical value for biological tissue [11]. In this section we consider the effect of refractive index mismatches. The configuration taken into account in the following simulations is reported in Fig. 4.27. The upward external refractive index, n_e, is fixed to 1.0 since in the applications there is air over the slab. The downward external refractive index, n_e', is chosen equal to n_2 since in many applications the bilayer geometry is considered inside a real biological tissue which is thick more than 40 mm. With this choice we are not considering reflection at the bottom of the slab.

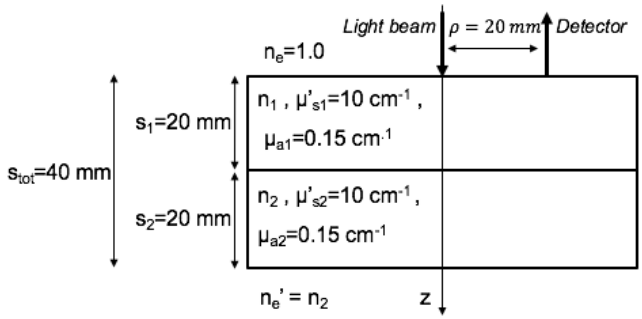

Figure 4.27: Bilayer geometry used in the simulations. Parameters are reported with their corresponding values while n_1 and n_2 changes between the simulations.

4.5.1 Simulations with small refractive index mismatch

We begin with some simulations considering the typical refractive index mismatches found in tissue optics which are on the order of $\Delta n = n_2 - n_1 = 0.01$ [11].
The first two simulations implement a positive mismatch, $\Delta n > 0$. Results are reported in Fig. 4.28. The profile of the probability density functions for the cases with $\Delta n = 0.1$ and $\Delta n = 0.2$ is similar to the case with no refractive index mismatch, except for a huge peak at the interface between the two layers (z=20 mm). We can interpret this peak as a consequence of the reflection. Indeed, some photons are reflected at the interface between the two layers and they turn around toward the surface. This is why photons have a high probability of having z_{max}=20 mm. However, this peak does not affect the statistics since it is really narrow. For this reason, the mean maximum penetration depths are equal to the case with no refractive index mismatch (Fig. 4.28a).

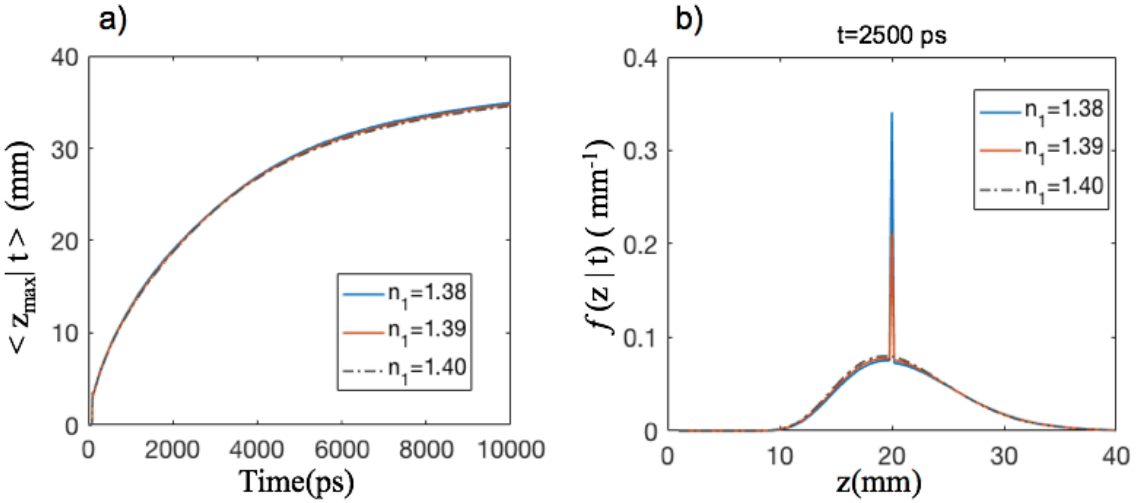

Figure 4.28: f(z|t) and ⟨z_{max} | t⟩ calculated for the bilayer slab geometry of Fig. 4.27 with n_2=1.40. In panel a) ⟨z_{max} | t⟩ is reported for three different values for n_1. In panel b) f(z|t) at t=2500 ps is reported for three different values for n_1.

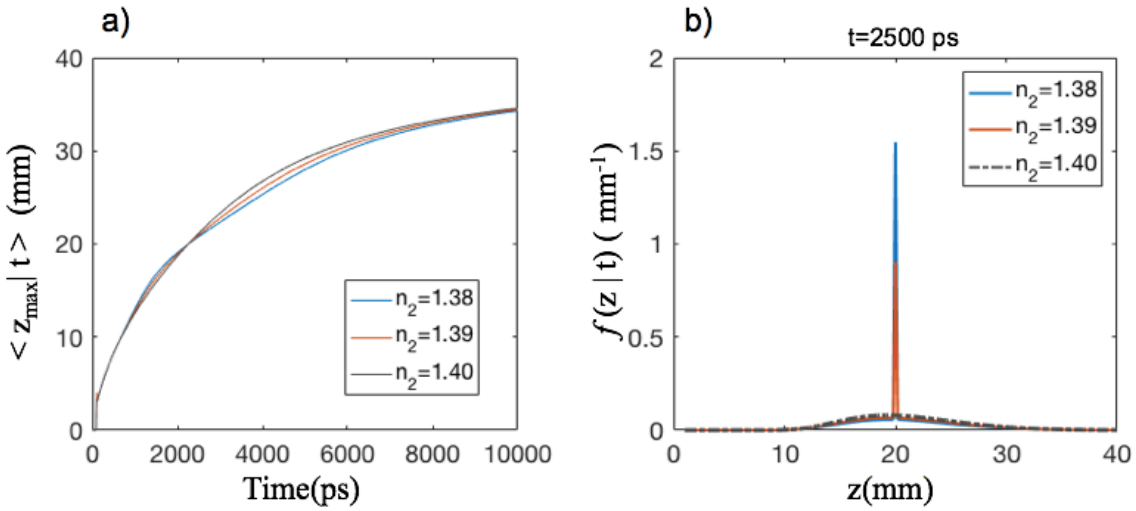

Figure 4.29: f(z|t) and ⟨z_{max} | t⟩ calculated for the bilayer slab geometry of Fig. 4.27 with n_1=1.40. In panel a) ⟨z_{max} | t⟩ is reported for three different values for n_2. In panel b) f(z|t) at t=2500 ps is reported for three different values for n_2.

Then, we take into account a negative mismatch, $\Delta n < 0$. In Fig. 4.29 the results are reported for the cases with $\Delta n = -0.1$ and $\Delta n = -0.2$. It must be noted that the peaks of *f(z|t)* are higher than the previous ones. Indeed, the probability of reflection for a photon is higher in this case since above the critical angle of incidence we have total reflection. The critical angle in this two cases is about 80° and also in this case the peak of *f(z|t)* does not affect significantly $\langle z_{max}|t\rangle$ as we can see in Fig. 4.29a.

4.5.2 Simulations with large refractive index mismatch

In the second series of simulations we try a large refractive index mismatch between the two layer, i.e., $\Delta n = \pm 0.1$. The results are reported in Fig. 4.30 and 4.31 for the different configurations tested. Now the critical angle is about 68° so many photons are in the regime of total internal reflection when $\Delta n < 0$. This is highlighted in Fig. 4.30 in which we can see that the peak of *f(z|t)* is much higher in the case with $\Delta n < 0$. This affects a lot $\langle z_{max}|t\rangle$ that is bent toward lower depths when it approaches 20 mm (Fig.4.31).

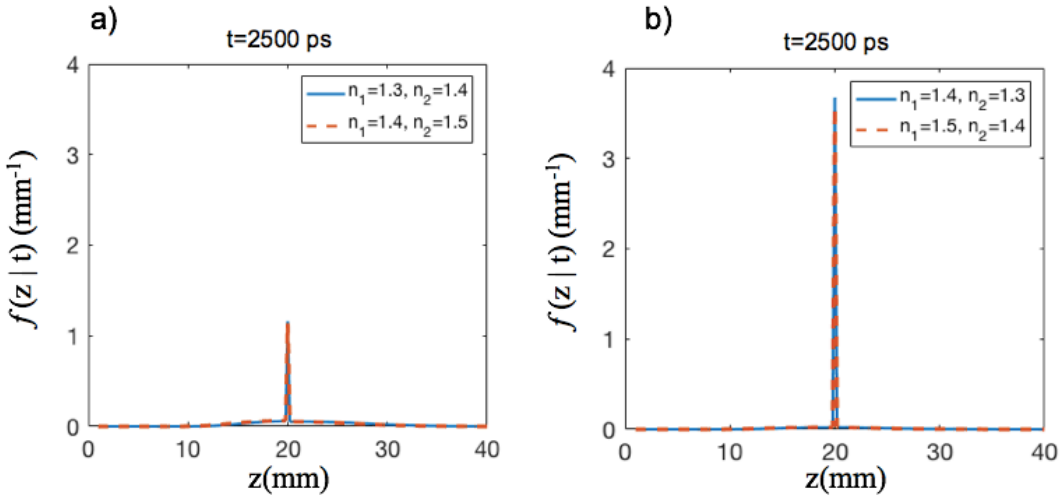

Figure 4.30: f(z|t) calculated for the bilayer slab geometry of Fig. 4.27 with large refractive index mismatch. In panel a) f(z|t) is reported in the cases in which $n_2 > n_1$. In panel b) f(z|t) is reported in the cases in which $n_2 < n_1$.

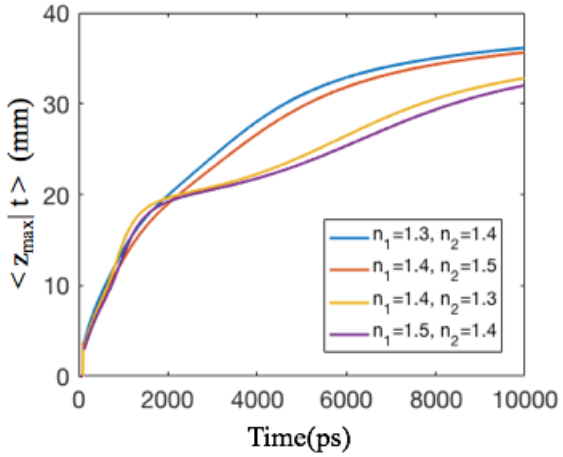

Figure 4.31: $\langle z_{max} \mid t\rangle$ calculated for the bilayer slab geometry of Fig. 4.27 with large refractive index mismatch.

In conclusion, values of refractive index mismatches that are present in biological media do not change significantly the statistics of photon penetration and they can be neglected. However, if there is a high refractive index mismatch due to external causes, it must be taken into account.

In this chapter we have studied how the physical parameters of a bilayer slab affects the statistics of photon penetration depth in time domain. In the next chapter the CW domain will be inspected.

Bibliography Chapter 4

[1] R.F.Bonner, R.Nossal, S.Havlin, and G.H.Weiss, “Model for photon migration in turbid biological media,”J.Opt.Soc. Am. A 4, 423-432 (1987).

[2] G. Weiss, “Statistical Properties of the Penetration of Photons into a Semi-Infinite Turbid Medium: A Random-Walk Analysis,” Appl. Opt. 37, 3558-3563 (1998).

[3] G. Weiss, J. Porrà, and J. Masoliver, “Statistics of the depth probed by cw measurements of photons in a turbid medium,” Phys. Rev. E 58, 6431-6439 (1998).

[4] F. Martelli, T. Binzoni, A. Pifferi, L. Spinelli, A. Farina, and A.Torricelli, "There's plenty of light at the bottom: statistics of photon penetration depth in random media", Scientific Reports 6:27057 (2016).

[5] B. Sun, L. Zhang, H. Gong, J. Sun, and Q. Luo, “Detection of optical neuronal signals in the visual cortex using continuous wave near-infrared spectroscopy,” Neuroimage 87, 190–198 (2014).

[6] T. Durduran and A. G. Yodh, “Diffuse correlation spectroscopy for non-invasive, micro-vascular cerebral blood flow measurement,” Neuroimage 85, 5163 (2014).

[7] A. Torricelli, D. Contini, A. Pifferi, M. Caffini, R. Re, L. Zucchelli, and L. Spinelli, “Time domain functional NIRS imaging for human brain mapping,” Neuroimage 85, 28–50 (2014).

[8] A. Farina, A. Torricelli, I. Bargigia, L. Spinelli, R. Cubeddu, F. Foschum, M. Jager, E. Simon, O.Fugger, A. Kienle, F. Martelli, P. Di Ninni, G. Zaccanti, D. Milej, P. Sawosz, M. Kacprzak, A. Liebert, and A. Pifferi, " In-vivo multilaboratory investigation of the optical properties of the human head", Optical society of America (2015).

[9] F. Martelli, S. Del Bianco, A. Ismaelli, and G. Zaccanti, "Light Propagation through Biological Tissue and Other Diffusive Media: Theory, Solutions and Software*",* SPIE Press, Washington, USA (2010), Chap. 2 (pag. 9,19), Chap. 3 (pag. 38-39), Chap. 4 (pag. 57-58),

[10] L. Zucchelli,1, D. Contini,1 R. Re, A. Torricelli and L. Spinelli, "Method for the discrimination of superficial and deep absorption variations by time domain fNIRS", Biomed Opt Express. 20; 4(12):2893-910 (2013).

[11] F. Martelli, S. Del Bianco, and G. Zaccanti, “Effect of the refractive index mismatch on light propagation through diffusive layered media,” *Phys. Rev. E.* 70, 011907 (2004).

CHAPTER 5

Bilayer geometry simulations in CW

In many applications of biomedical optics, light with a constant intensity is used to non-invasively investigate tissue structures and functions. This modality of measurement is called steady state or continuous wave (CW) and it offers a good signal to noise-ratio and a low cost instrumentation that can be miniaturized to the extent of a wireless instrument. For this reason, several commercial versions are available. Unfortunately, CW methods have a series of disadvantages such as the possibility to extrapolate only the relative values of the hemodynamic parameters with measurements at one wavelength [1], the impossibility in discriminating between the surface and deeper contributions and the sensitivity to the motion artefact.

The CW photon penetration depth has been studied by several research groups. The pioneering work by Bonner et al. [2] used a simple random walk model of light propagation to provide expressions for the mean maximum penetration depth in the homogeneous slab geometry and it was validated with MC simulation. In the work by Martelli et al. [3] analytical formula for $f(z|t)$ and $\langle z_{max} \mid t \rangle$ are reported for the homogeneous slab geometry. A preliminary study of penetration depth in a layered medium was done in the work by Nossal et al. [4] but it was not validated with MC simulations.

The aim of this chapter is to study photon penetration depth for a bilayer slab geometry in the CW domain. Numerical simulations are done using the method developed and validated in Chapter 3. The chapter is divided into two sections which describe the dependence of photon penetration depth on absorption coefficient and reduced scattering coefficient.

5.1 Simulations varying the absorption coefficient

In this paragraph we study the dependence of the CW mean maximum penetration depth for photon detected at a given source-detector distance $\langle z_{max} \mid \rho \rangle$ on the absorption coefficients of our bilayer slab geometry.

We have already seen in Chapter 3 that in CW domain $\langle z_{max} \mid \rho \rangle$ is strongly dependent on μ_a. In Fig. 5.1 we report $\langle z_{max} \mid \rho \rangle$ and $f(z \mid \rho)$ calculated for a homogenous slab for different values of μ_a. The probability density function moves toward lower values of z when μ_a increases. As a consequence, $\langle z_{max} \mid \rho \rangle$ decreases. This behavior can be understood in the following way. Since in a CW measurement photons with different pathlength are mixed together and summed up, when μ_a increases, photons with a small pathlength are statistically favorite. These photons are likely to have a small z_{max}, so $\langle z_{max} \mid \rho \rangle$ decreases. It must be also noted that $\langle z_{max} \mid \rho \rangle$ is an increasing function of ρ. This fact has been already verified in previous work [2, 6]. Indeed, when ρ increases, it is progressively probed a greater portion of medium and photons increase their z_{max} on average.

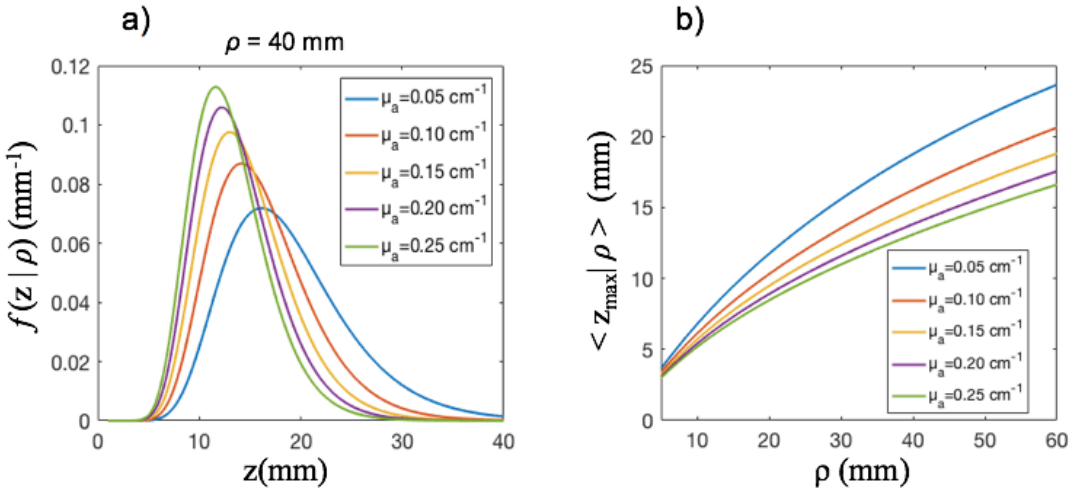

Figure 5.1: $f(z|\rho)$ and $\langle z_{max} \mid \rho \rangle$ in panel a) and b) respectively, calculated for a homogeneous slab of thickness 40 mm, $n_{int}=n_{out}=1.4$. The reduced scattering coefficient μ'_s is fixed at 10 cm^{-1} while μ_a varies between 0.05 cm^{-1} and 0.25 cm^{-1}.

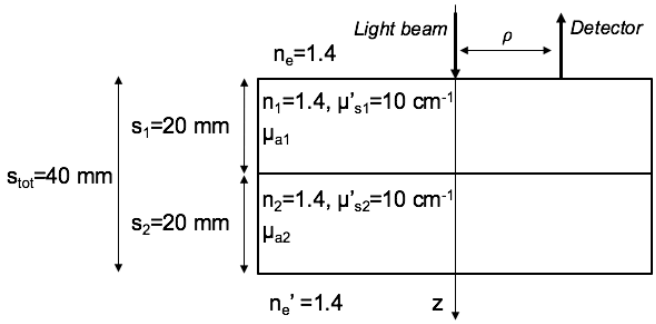

Figure 5.2: Bilayer geometry used in the simulations. Parameters are reported with their corresponding values.

The bilayer slab geometry used in the simulations is represented in Fig. 5.2. For each simulation the reduced scattering coefficients of both layers is fixed at 10 cm^{-1} while the absorption coefficients of the two layers vary. The bilayer slab parameters follow the same

pattern used in TD simulations (see Chapter 4.1). No refractive index mismatch is taken into account between the outside and the inside of the medium and also between the two layers. The interfiber distance varies between 0 mm and 60 mm but the first 5 mm are not considered since in this range the diffusion approximation does not hold anymore (see Chapter 3.4) [5].

5.1.1 Variation of μ_{a1}

In the first series of simulations we make μ_{a1} vary in the interval [0.05, 0.25] cm^{-1} with a step of 0.05 cm^{-1}, while μ_{a2} is fixed at 0.15 cm^{-1}. In Fig. 5.3 the numerical evaluated $\langle z_{max} \mid \rho \rangle$ and $f(z \mid \rho)$ are reported. First of all, we notice that $f(z \mid \rho)$ moves toward a deeper z as ρ increases, as we expected (Fig. 5.3a, 5.3b and 5.3c). Moreover, fixed the interfiber distance, the probability density function moves toward a lower z if μ_{a1} increases. For small values of ρ the behavior of the mean maximum penetration depths (Fig. 5.3d) is similar to the homogeneous cases (Fig. 5.1.b) since detected photons probe only the first layer. However, for large values of ρ (ρ>50 mm), the differences decreases between the $\langle z_{max} \mid \rho \rangle$ relative to different μ_{a1} since more and more photons reach the second layer with μ_{a2}=0.15 cm^{-1} in all simulations.

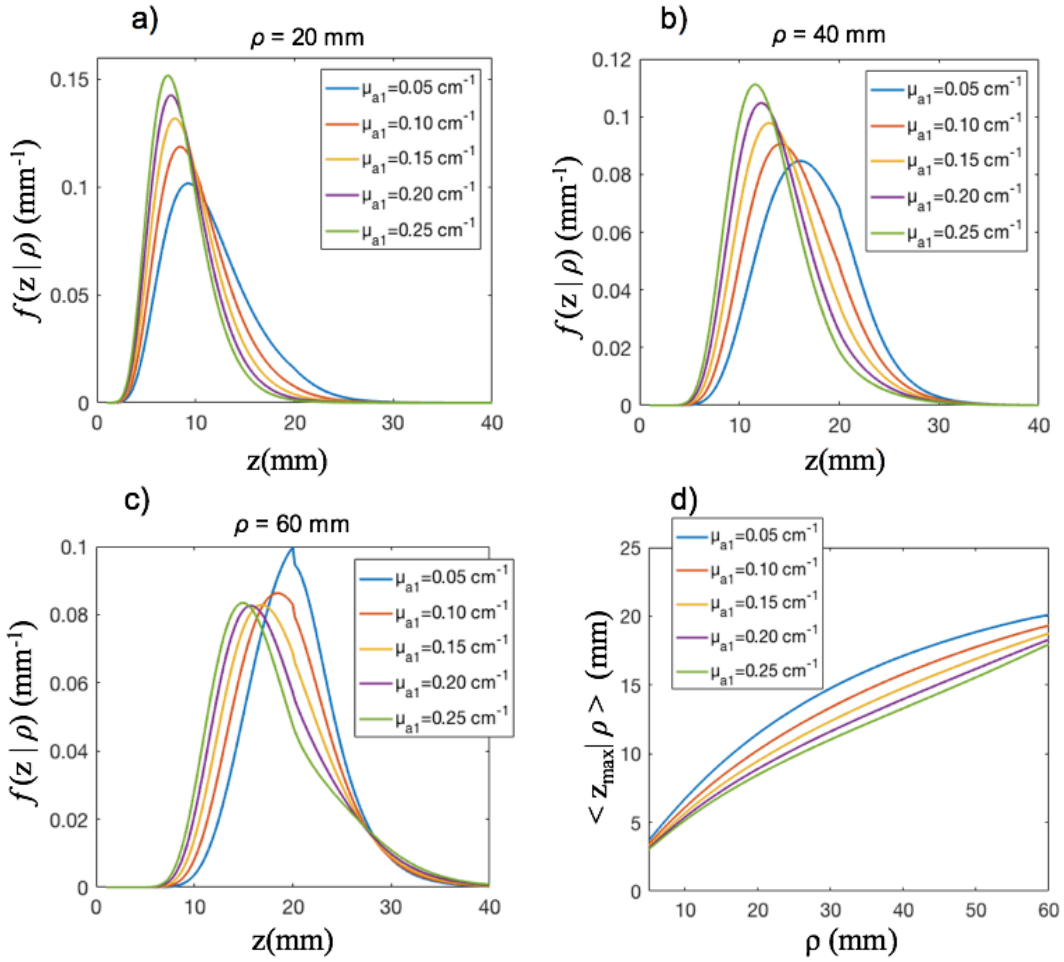

Figure 5.3: $f(z|\rho)$ and $\langle z_{max} \mid \rho \rangle$ are reported for different values of μ_{a1}, μ_{a2} is fixed at 0.15 cm^{-1}. In panel a), $f(z|\rho)$ for ρ =20 mm. In panel b), $f(z|\rho)$ for ρ =40 mm. In panel c), $f(z|\rho)$ for ρ =60 mm. In panel d) $\langle z_{max} \mid \rho \rangle$ is reported.

5.1.2 Variation of μ_{a2}

In the second series of simulations we make μ_{a2} vary in the interval [0.05, 0.25] cm^{-1} with a step of 0.05 cm^{-1}, while μ_{a1} is fixed at 0.15 cm^{-1}. In Fig. 5.4 the numerical evaluated $\langle z_{max} \mid \rho \rangle$ and $f(z \mid \rho)$ are reported. For small values of interfiber distance $f(z \mid \rho)$ is equal in all five simulations since detected photons probe only the first layer with μ_{a1}=0.15 cm^{-1} (Fig. 5.4a). As ρ increases, the probability density functions relative to different μ_{a2} begin to split up (Fig. 5.4b). For large values of ρ many photons enter in the second layer and $f(z \mid \rho)$ increases in the interval z > 20 mm as μ_{a2} decreases (Fig. 5.4c). Indeed, photons which travel in the second layer become more and more favorite if $\mu_{a2} < \mu_{a1}$. The behavior of the mean maximum penetration depths is in accordance with that of $f(z \mid \rho)$. Thus, the curves of $\langle z_{max} \mid \rho \rangle$ are superimposed for small interfiber distances. However, for ρ>30 mm, the curves split up and $\langle z_{max} \mid \rho \rangle$ increases as μ_{a2} decreases (Fig. 5.4d).
In conclusion, an increase in the absorption coefficient of one layer makes photons with pathlength in that layer reach a lower z_{max}. When μ_{a1} varies, this behavior affects all photons. However, when μ_{a2} varies, only photons which reach the second layer change their statistics.

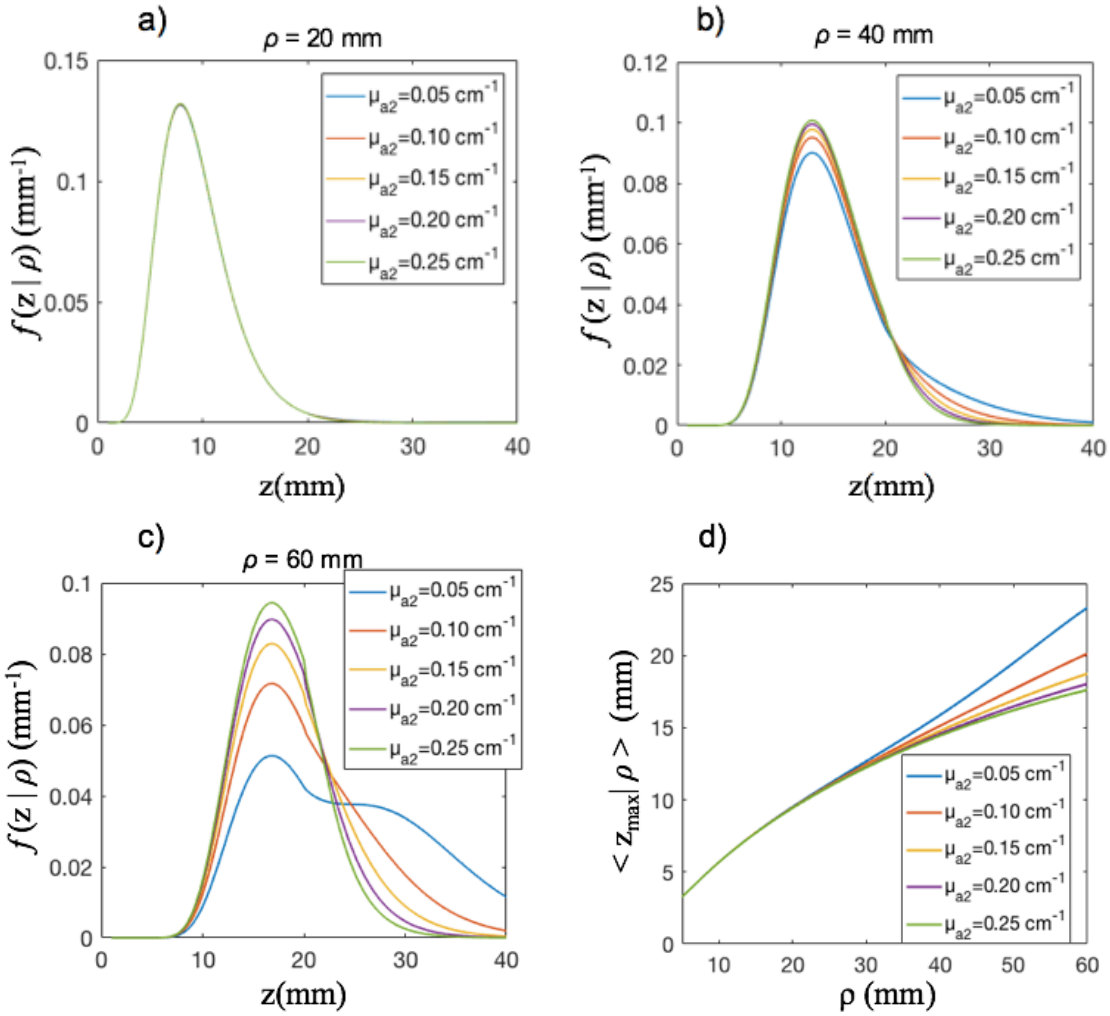

Figure 5.4: $f(z|\rho)$ and $\langle z_{max} \mid \rho \rangle$ are reported for different values of μ_{a2}, μ_{a1} is fixed at 0.15 cm^{-1}. In panel a), $f(z|\rho)$ for ρ =20 mm. In panel b), $f(z|\rho)$ for ρ =40 mm. In panel c), $f(z|\rho)$ for ρ =60 mm. In panel d) $\langle z_{max} \mid \rho \rangle$ is reported.

5.1.3 Extreme cases

Two extreme simulations are reported for CW domain as we did in TD. The former has μ_{a1}=0.5 cm^{-1} and μ_{a2}=0 cm^{-1} while the latter has μ_{a1}=0 cm^{-1} and μ_{a2}=1 cm^{-1}. All the other parameters have the same values of the previous simulations and they are reported in Fig. 5.2. The profile of $f(z|\rho)$ in these two cases has interesting features. In the former case (Fig. 5.5a) we can see that $f(z|\rho)$ moves toward a deeper z as ρ increases. For ρ=50 mm $f(z|\rho)$ has a minimum at about z=20 mm an a successive increase for z>20 mm due to the fact that photons are not absorbed in the second layer. The mean maximum penetration depth is equal to that of a homogeneous slab with $\mu_a=\mu_{a1}$=0.5 cm^{-1} for ρ<30 mm. Then, as soon as photons begin to reach the second layer, $\langle z_{max} \mid \rho \rangle$ significantly increases with respect to the homogenous case (Fig. 5.5c). On the other hand, in the case with μ_{a1}=0 cm^{-1} and μ_{a2}=1 cm^{-1}, $f(z|\rho)$ rapidly decreases at $z=s_1$=20 mm since photons prefer to remain in the first layer as we can see in Fig. 5.5b. Indeed, photons entering the second layer are almost all absorbed. As a result, $\langle z_{max} \mid \rho \rangle$ remains under 20 mm for all interfiber distances and it is significantly lower than in the homogeneous case with $\mu_a=\mu_{a1}$=0cm^{-1} (Fig. 5.5d).

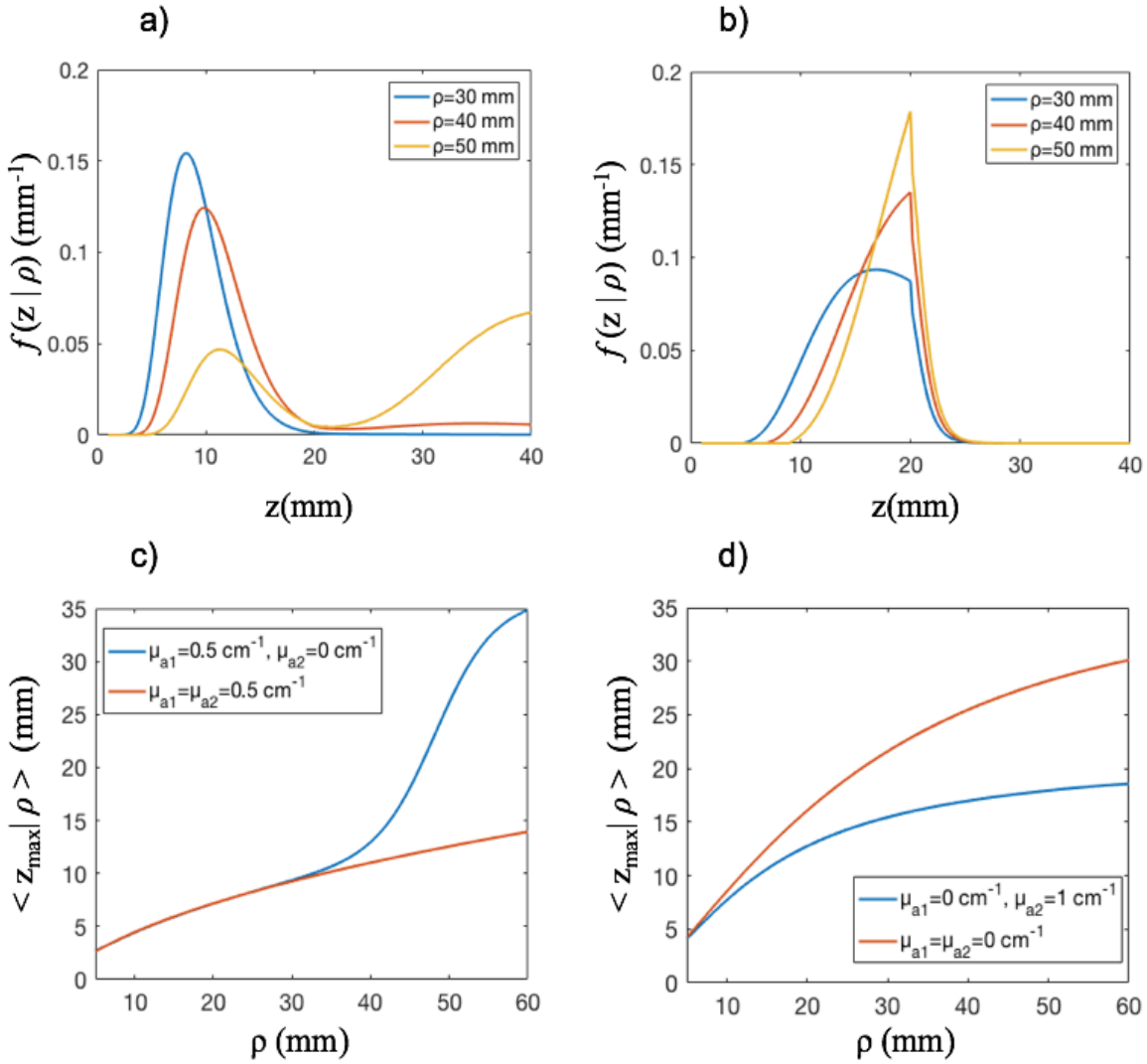

Figure 5.5: $f(z|\rho)$ and $\langle z_{max} \mid \rho \rangle$ calculated in the two extreme situation. Panels a) and c) refers to the case with μ_{a1}=0.5 cm^{-1} and μ_{a2}=0 cm^{-1} while panels b) and c) refers to the case with μ_{a1}=0 cm^{-1} and μ_{a2}=1 cm^{-1}.

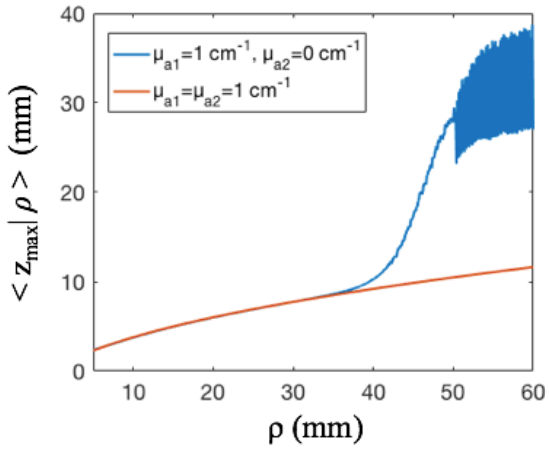

Figure 5.6: f(z| ρ) and ⟨zmax | ρ ⟩ calculated in the case with μ_{a1}=1 cm^{-1} and μ_{a2}=0 cm^{-1}.

The case with μ_{a1}=1 cm^{-1} and μ_{a2}=0 cm^{-1} is not taken into account in the following analysis since some computational errors occur in the corresponding simulation for great interfiber distances due to really low values of the corresponding reflectance curves (see Fig. 5.6). This concludes the study of the absorption coefficient effects. In the following paragraph we will talk about the reduced scattering coefficient effects.

5.2 Simulations varying the reduced scattering coefficient

In this paragraph we highlight the effect of the reduced scattering coefficients on the statistics of photon penetration depth.

Before starting our simulations on the bilayer geometry we study the case of the homogeneous slab geometry. We calculate ⟨zmax | ρ ⟩ and *f(z| ρ)* for different values of μ'_s between 6 cm^{-1} and 14 cm^{-1}, while μ_a=0 cm^{-1} (Fig. 5.7). We can see that the effect of a variation of μ'_s is negligible for both ⟨zmax | ρ⟩ and *f(z| ρ)*. Indeed, in CW domain photons with different pathlength are mixed together and the way of thinking used in TD does not hold anymore since time is not fixed here (see Chapter 4.2).

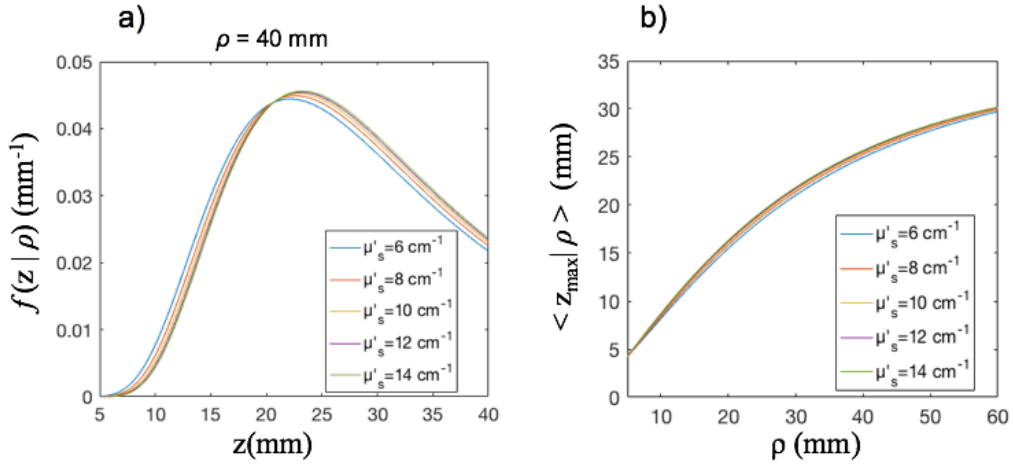

Figure 5.7: f(z| ρ) and ⟨zmax | ρ ⟩ in panel a) and b) respectively, calculated for a homogeneous slab of thickness 40 mm, n_{int}=n_{out}=1.4, μ_a=0 cm^{-1}.The reduced scattering coefficient μ'_s varies between 6 cm^{-1} and 14 cm^{-1}.

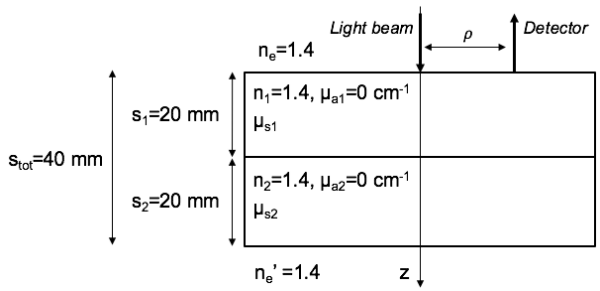

Figure 5.8: Bilayer geometry used in the simulations. Parameters are reported with their corresponding values.

Then we consider the bilayer slab geometry with the same parameters used in previous simulations, but now the absorption coefficients are set to zero and the reduced scattering coefficients vary (Fig. 5.8).

5.2.1 Variation of μ'_{s1}

In the first series of simulations we make μ'_{s1} vary in the interval [6, 14] cm^{-1} with a step of 2 cm^{-1}, while μ'_{s2} is fixed at 10 cm^{-1}. As in the homogeneous case, the mean maximum penetration depth does not show significant differences between the five cases (Fig. 5.9). Only for ρ >40 mm the curves are separated with the curve relative to μ'_{s1}=6 cm^{-1} being the lowest and the curve relative to μ'_{s1}=14 cm^{-1} being the highest. However, the variation between the different curves is on the order of few millimeters, so the effect of μ'_{s1} on $\langle z_{max} \mid \rho \rangle$ is negligible. If we take into account the calculated $f(z \mid \rho)$ we see the same jump found in TD at the boundary between the two layers. When $\mu'_{s1} < \mu'_{s2}$, $f(z \mid \rho)$ increases at z=20 mm and the jump is bigger if $\Delta\mu'_s$ is bigger (Fig. 5.10a, 5.10c and 5.10e). On the other hand, when $\mu'_{s1} > \mu'_{s2}$, $f(z \mid \rho)$ decreases at z=20 mm and the jump is bigger if $\Delta\mu'_s$ is bigger (Fig. 5.10b, 5.10d and 5.10f). Thus, also in CW domain, a mismatch in the reduced scattering coefficient produced a discontinuity in $f(z \mid \rho)$ at the boundary between the two layer where mean free path of photons abruptly changes.

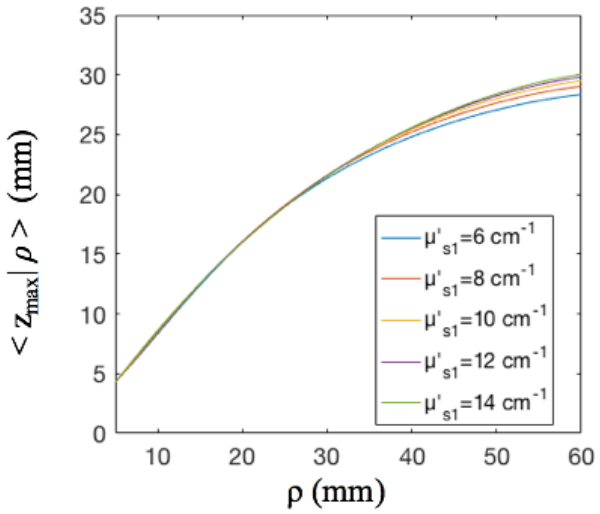

Figure 5.9: $\langle z_{max} \mid \rho \rangle$ are reported for different values of μ'_{s1}, μ'_{s2}=10 cm^{-1}.

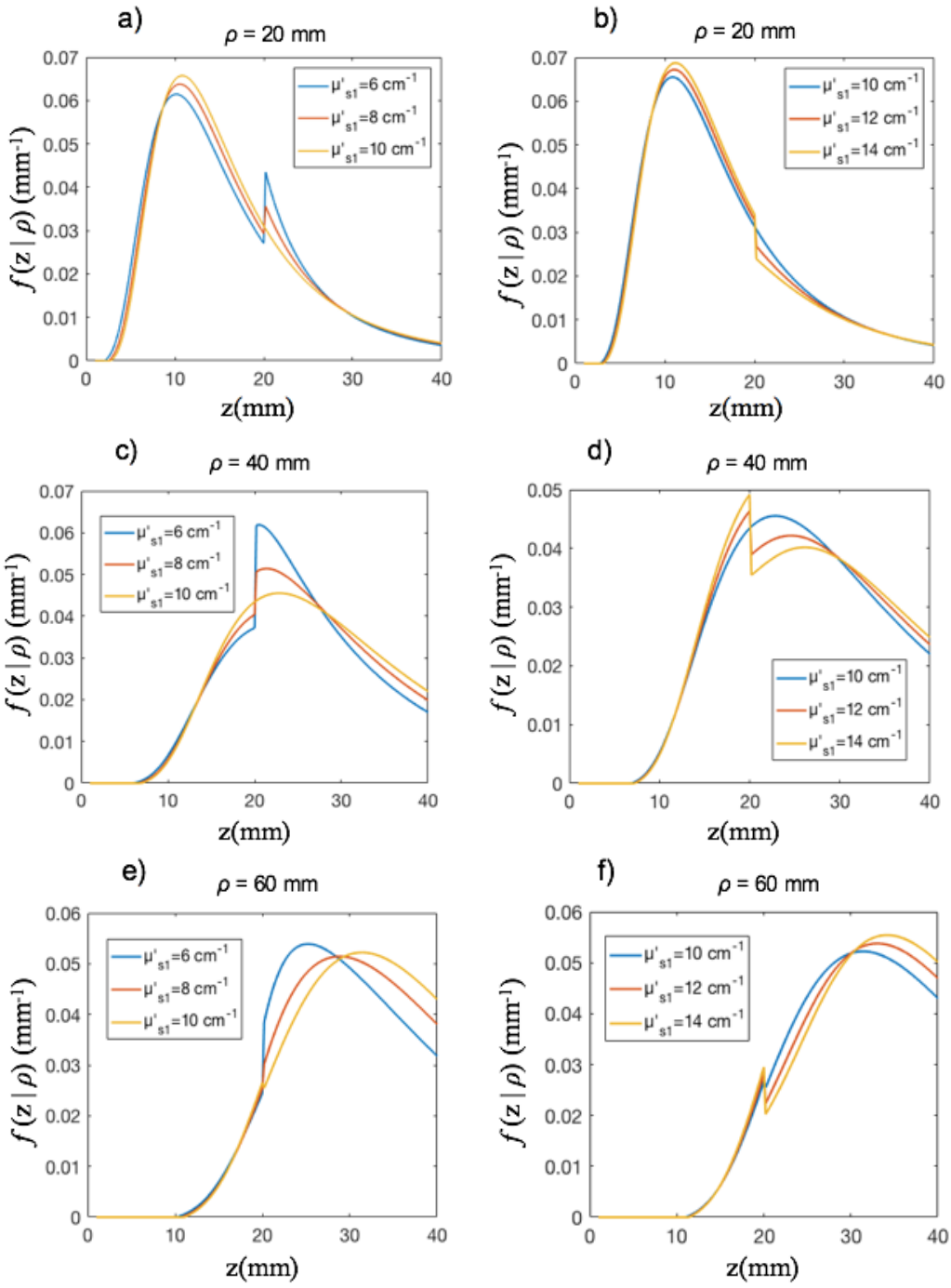

Figure 5.10: f(z| ρ) reported for different values of μ'_{s1}, μ'_{s2}=10 cm^{-1}. f(z| ρ) for ρ =20 mm in the cases where $\mu'_{s1} < \mu'_{s2}$ and $\mu'_{s2} < \mu'_{s1}$ is reported in panel a) and b) respectively. f(z| ρ) for ρ =40 mm is reported in panel c) and d). f(z| ρ) for ρ =60 mm is reported in panel e) and f).

5.2.2 Variation of μ'_{s2}

In the second series of simulations we make μ'_{s2} vary in the interval [6, 14] cm^{-1} with a step of 2 cm^{-1}, while μ'_{s1} is fixed at 10 cm^{-1}. In Fig. 5.11 and Fig. 5.12 the main results are reported. As in the previous series of simulations, the mean maximum penetration depth does not show significant differences between the five cases (see Fig. 5.12). So the effect of μ'_{s2} on $\langle z_{max} \mid \rho \rangle$ is negligible. In Fig. 5.11 we can see we see the same discontinuity in

the probability density function observed also in previous simulations. When $\mu'_{s1} < \mu'_{s2}$, $f(z|\ \rho)$ increases at z=20 mm. On the other hand, when $\mu'_{s1} > \mu'_{s2}$, $f(z|\ \rho)$ decreases at z = 20 mm.

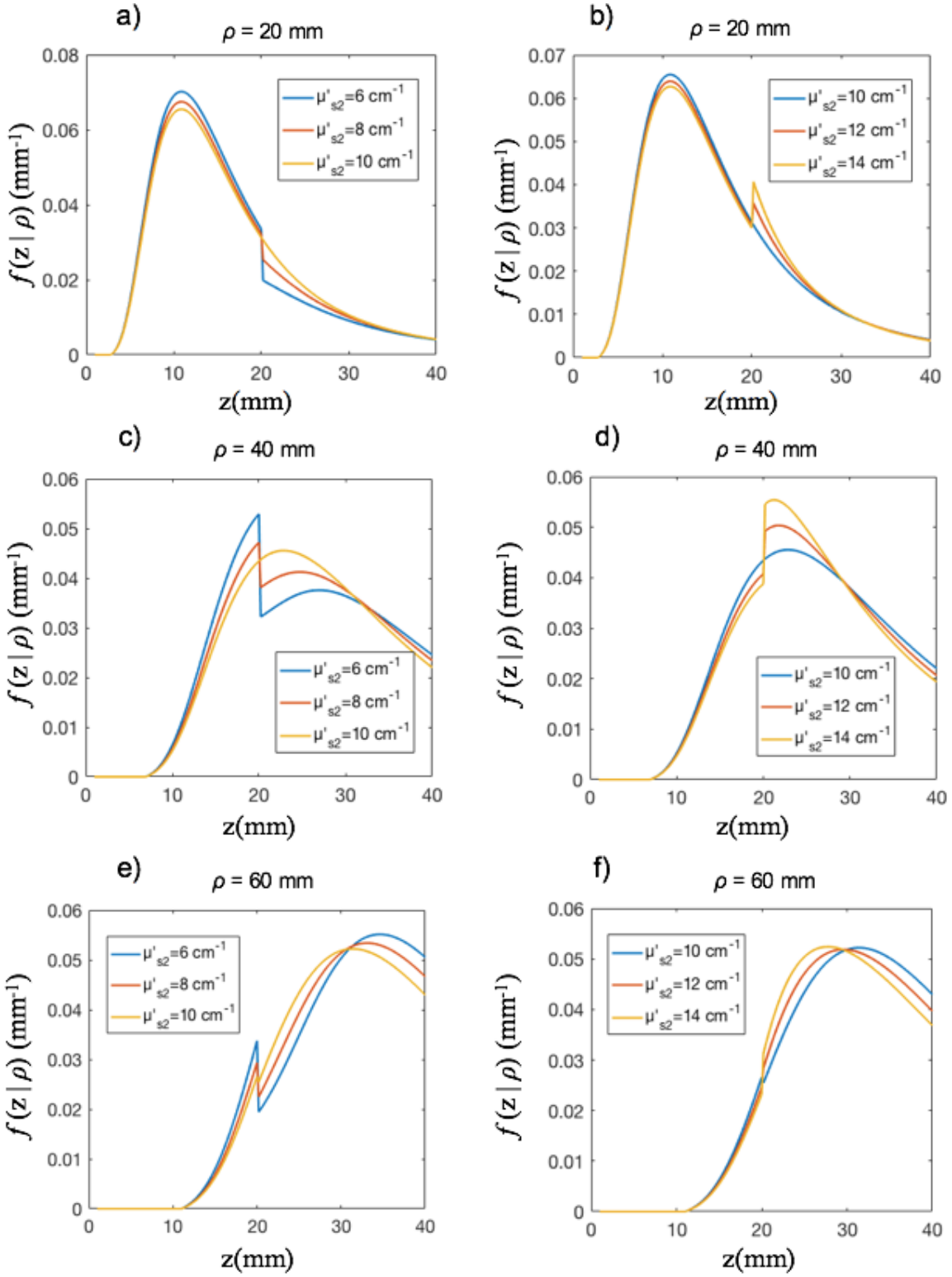

Figure 5.11: $f(z|\ \rho)$ reported for different values of μ'_{s2}, $\mu'_{s1}=10\ cm^{-1}$. $f(z|\ \rho)$ for ρ =20 mm in the cases where $\mu'_{s2} < \mu'_{s1}$ and $\mu'_{s1} < \mu'_{s2}$ is reported in panel a) and b) respectively. $f(z|\ \rho)$ for ρ =40 mm is reported in panel c) and d) respectively. $f(z|\ \rho)$ for ρ =60 mm is reported in panel e) and f) respectively.

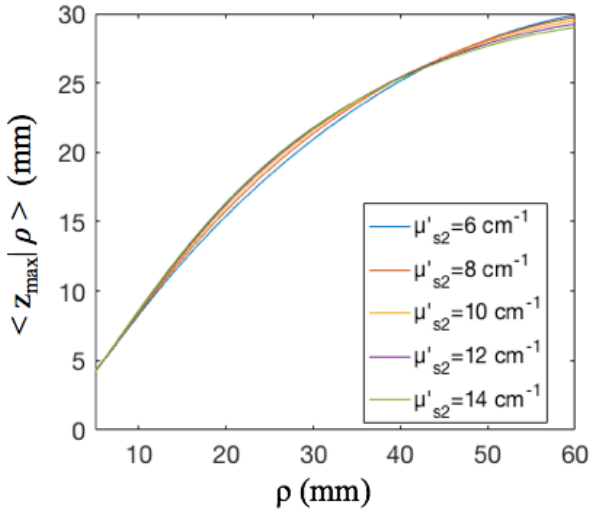

Figure 5.12: ⟨z_{max} | ρ⟩ are reported for different values of μ'_{s2}, μ'_{s1}=10 cm^{-1}.

In conclusion, we remark that reduced scattering coefficient variations inside the typical range of biological tissues do not significantly affect photon penetration depth. However, in this paragraph we have considered a slab with no absorption. In CW domain, the interplay between μ'_s and μ_a can be determinant. Thus, in order to test a more realistic configuration in the next two sections we repeat the same simulations with an absorption coefficient different from zero.

5.2.3 Variation of μ'_{s1} with μ_a=0.15 cm^{-1}

In this series of simulations, we repeat the pattern used in section 5.2.1 but with $\mu_{a1}=\mu_{a2}$=0.15 cm^{-1}. In Fig. 5.13a the ⟨z_{max} | ρ⟩ obtained varying μ'_{s1} are reported. We can immediately see that the penetration depth of photons is decreased with respect to the case with no absorption (Fig.5.13b). For example, at ρ=60 mm ⟨z_{max} | ρ⟩ is about 18 mm in the case with absorption while it is about 28 mm in the case with no absorption. This effect induced by an increase in the absorption coefficient has been already shown in Par. 5.1.

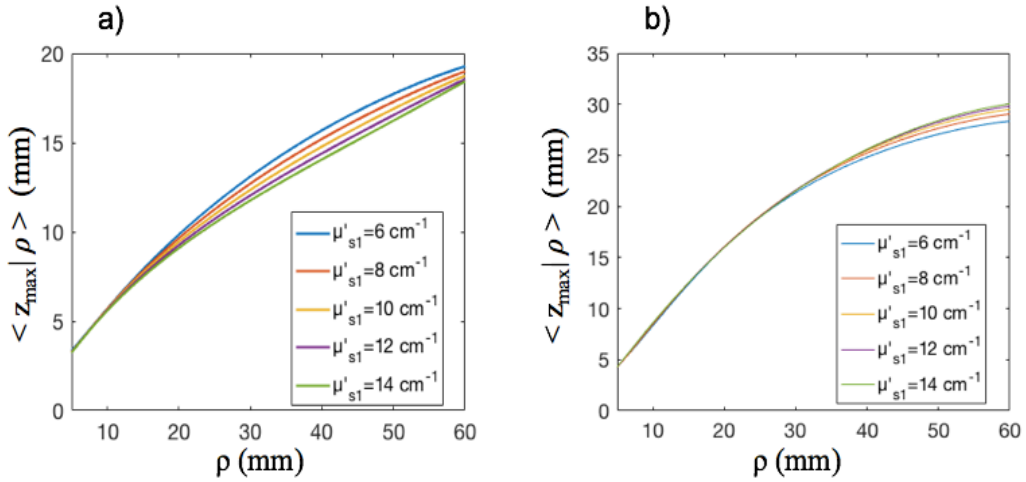

Figure 5.13: ⟨z_{max} | ρ⟩ are reported for different values of μ'_{s1}, μ'_{s2}=10 cm^{-1}. In panel a) $\mu_{a1}=\mu_{a2}$=0.15 cm^{-1} while in panel b) $\mu_{a1}=\mu_{a2}$=0 cm^{-1}.

Moreover, the effect of a variation in μ'_{s1} is larger in the case with $\mu_{a1}=\mu_{a2}=0.15\ cm^{-1}$ and the curves in Fig. 5.13a are splitted up also at lower interfiber distances than in Fig. 5.13b. The numerical evaluated $f(z|\ \rho)$ present the discontinuity that we expected at z=20 mm (Fig. 5.14).

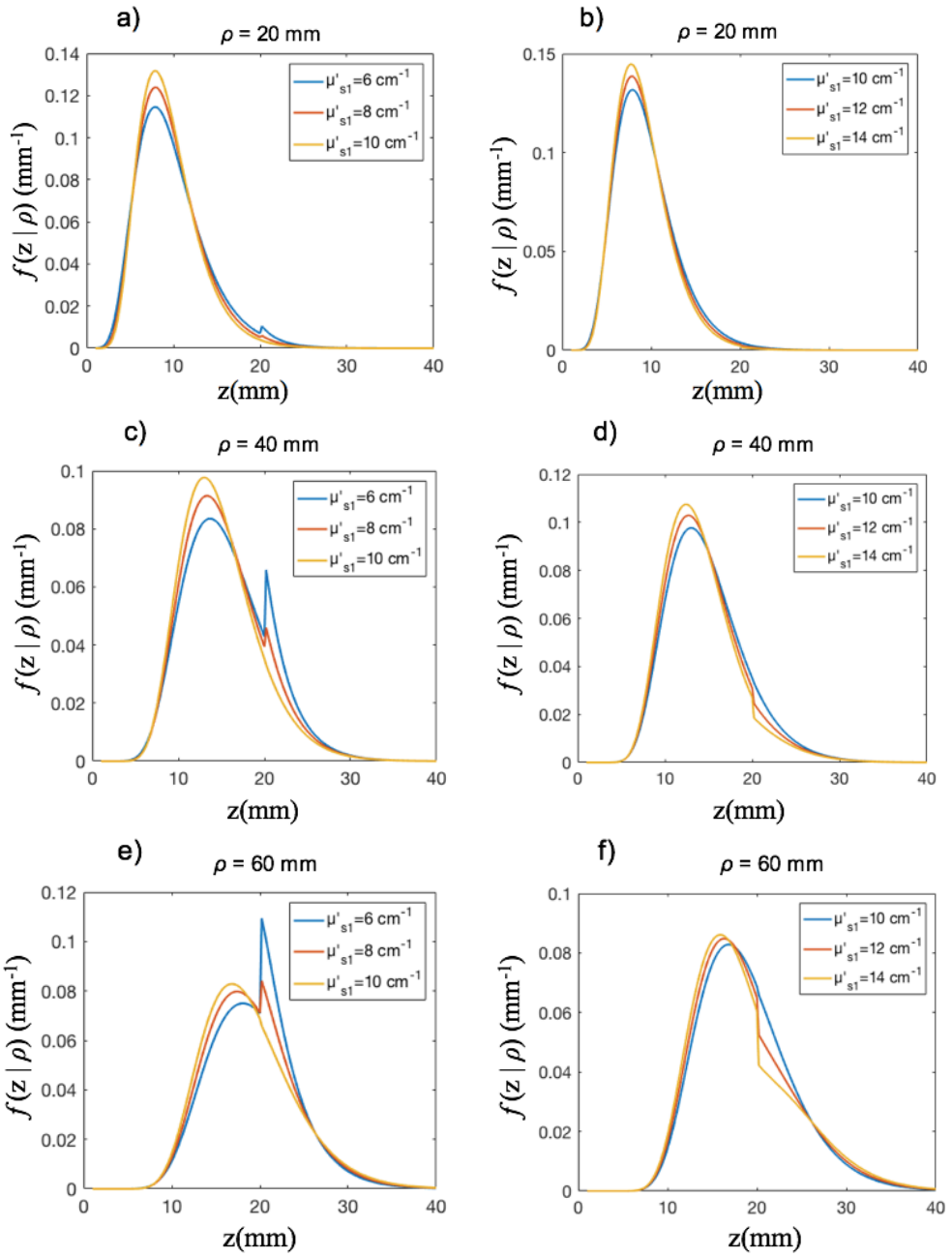

Figure 5.14: $f(z|\ \rho)$ reported for different values of μ'_{s1}, $\mu'_{s2}=10\ cm^{-1}$, $\mu_{a1}=\mu_{a2}=0.15\ cm^{-1}$. $f(z|\ \rho)$ for ρ =20 mm in the cases where $\mu'_{s1}<\mu'_{s2}$ and $\mu'_{s2}<\mu'_{s1}$ is reported in panel a) and b) respectively. $f(z|\ \rho)$ for ρ =40 mm is reported in panel c) and d). $f(z|\ \rho)$ for ρ =60 mm is reported in panel e) and f).

5.2.4 Variation of μ'_{s2} with $\mu_a=0.15\ cm^{-1}$

In this series of simulations, we repeat the pattern used in section 5.2.2 but with $\mu_{a1}=\mu_{a2}=0.15\ cm^{-1}$. The variation of μ'_{s2} is not negligible for ρ>45 mm when the $\langle z_{max}\,|\,\rho\rangle$ split up as we can see in Fig. 5.16. The maximum $\langle z_{max}\,|\,\rho\rangle$ is reached in the configuration

with the lowest μ'_{s2}. It is worth noting that also in this case the penetration depth of photons is decreased with respect to the case with no absorption (Fig.5.16b). If we take into account the calculated $f(z|\ \rho)$ (Fig. 5.15) we see the usual jump at the boundary between the two layers. Moreover, no differences in $f(z|\ \rho)$ are present for ρ=20 mm since photons do not penetrate in the second layer in this configuration and the variation of μ'_{s2} has no effects.

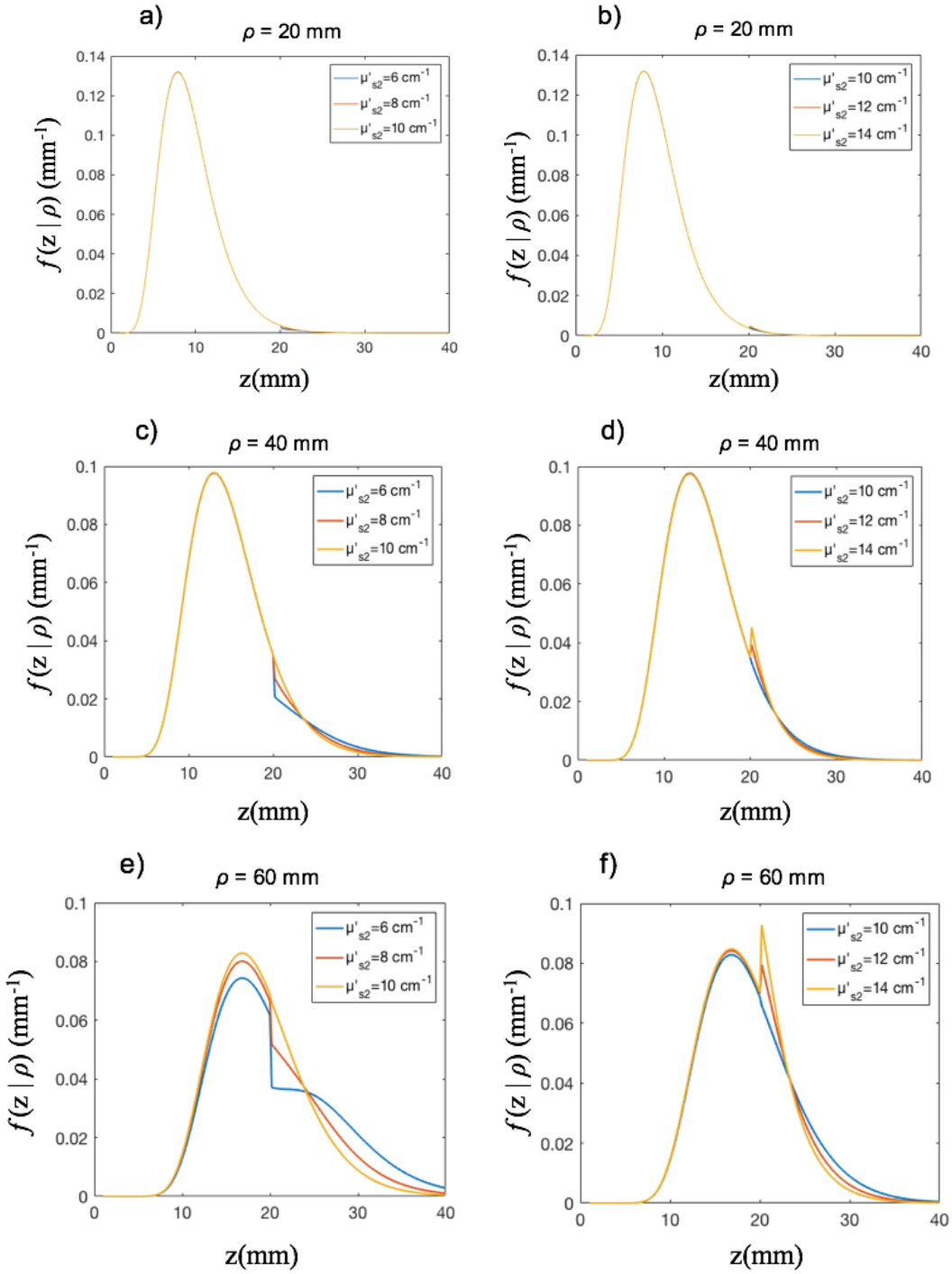

Figure 5.15: $f(z|\ \rho)$ reported for different values of μ'_{s2}, μ'_{s1}=10 cm^{-1}. $f(z|\ \rho)$ for ρ =20 mm in the cases where $\mu'_{s2} < \mu'_{s1}$ and $\mu'_{s1} < \mu'_{s2}$ is reported in panel a) and b) respectively. $f(z|\ \rho)$ for ρ =40 mm is reported in panel c) and d) respectively. $f(z|\ \rho)$ for ρ =60 mm is reported in panel e) and f) respectively.

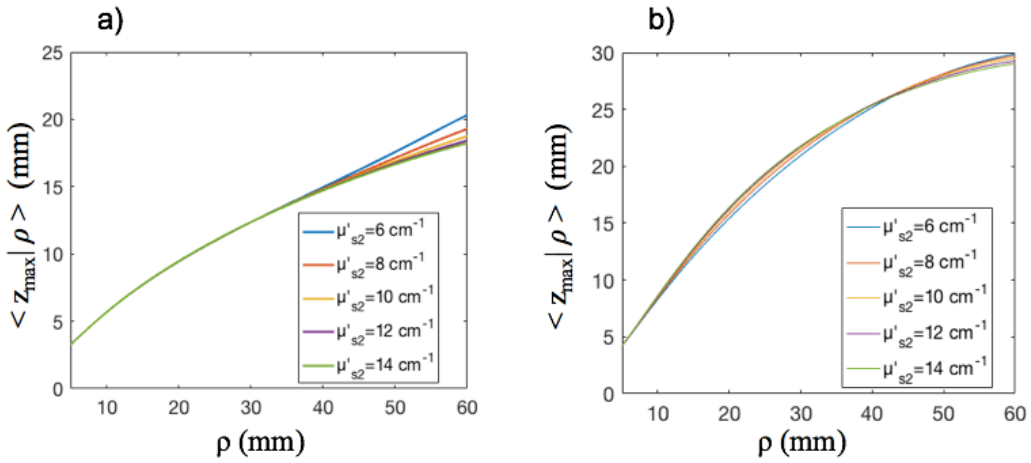

Figure 5.16: $\langle z_{max} \mid \rho \rangle$ are reported for different values of μ'_{s2}, μ'_{s1}=10 cm^{-1}. In panel a) μ_{a1}= μ_{a2}=0.15 cm^{-1} while in panel b) μ_{a1}= μ_{a2}=0 cm^{-1}.

In conclusion, it must be remarked that there are significant differences in the statistics of photon penetration depth between the case with no absorption and the case with absorption. Thus, the interaction between absorption and scattering coefficients plays a relevant role in CW domain. For this reason, it is difficult to separate the effect of μ'_s from the effect of μ_a.

5.2.5 Extreme cases

In the last series of simulations we take into account two extreme configurations, i.e., μ'_{s2}=100 cm^{-1} and μ'_{s2}=1000 cm^{-1}. In both cases μ'_{s1} is fixed to 10 cm^{-1} and μ_a=0 cm^{-1} as we did in TD. In Fig. 5.17 and 5.18 the results for $f(z|\ \rho)$ and $\langle z_{max}|\ \rho\rangle$ are reported together with the solutions to the homogeneous slab geometry with μ'_s=10 cm^{-1} (blu curves). The profile of the probability density functions is identical to the homogeneous case for z<20 mm but it differs a lot for z>20 mm (Fig. 5.17). Indeed, in these two extreme cases $f(z|\ \rho)$ is highly peaked in the first millimeters of the second layer.

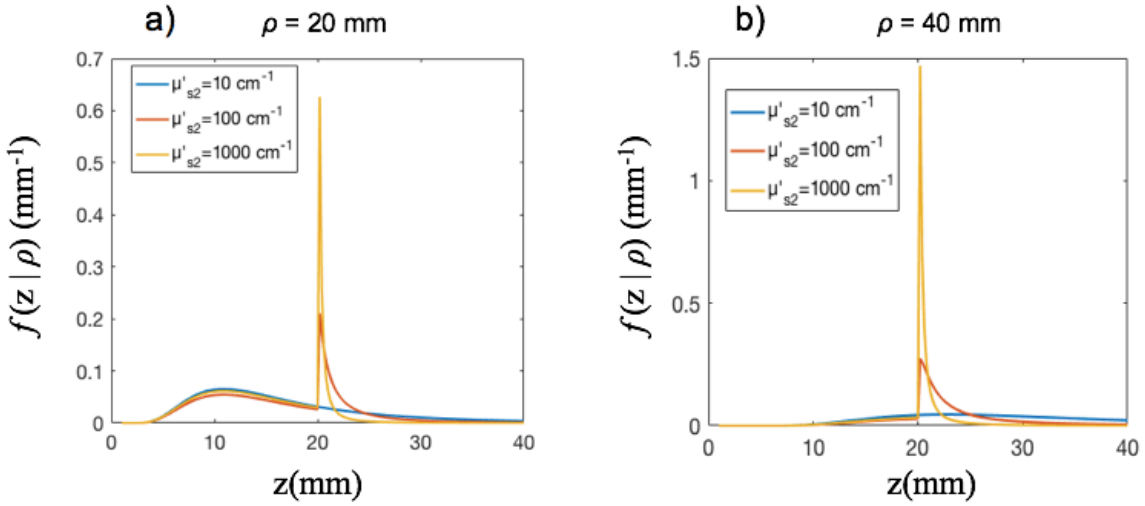

Figure 5.17: $f(z|\rho)$ calculated for μ'_{s2}=10 cm^{-1}, μ'_{s2}=100 cm^{-1} and μ'_{s2}=1000 cm^{-1} while μ'_{s1} is fixed to 10 cm^{-1}. In panel a) ρ=20 mm, in panel b) ρ=40 mm.

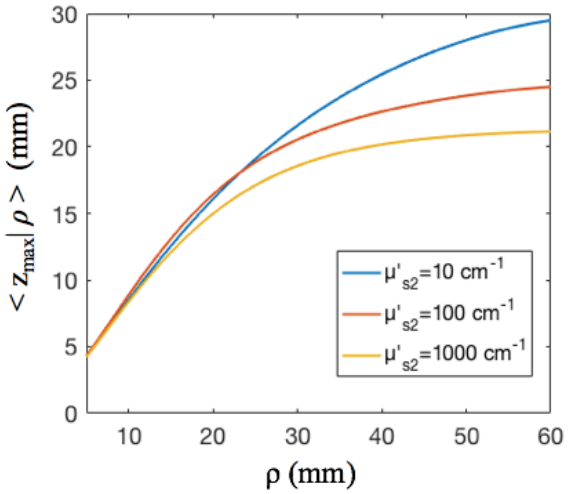

Figure 5.18: $\langle z_{max} \mid \rho \rangle$ calculated for μ'_{s2}=10 cm^{-1}, μ'_{s2}=100 cm^{-1} and μ'_{s2}=1000 cm^{-1} while μ'_{s1} is fixed to 10 cm^{-1}.

As a result, the mean maximum penetration depth in this two extreme cases is lower than in the homogeneous case since the high value of μ'_{s2} makes photon penetration really difficult in the second layer (see Fig. 5.18).

5.3 Conclusions

The method developed and validated in Chapter 3 promises to be a useful instrument in order to study particular bilayer configurations. This study reveals some features which can be interesting for many research applications such as functional near infrared spectroscopy in order to improve the technique and the data analysis. One possible application of the method is it to understand which tissue layers are probed by photons during a reflectance measurement.

In TD we proposed a way of looking at results which enable us to retrieve some important conclusions. The mean maximum penetration depth increases if the absorption coefficient of the deeper layer is lower than that of the superficial layer. Indeed, photons which travel a longer distance inside the less absorbing layer have a higher probability of being detected. This can be very interesting for applications. For example, in a multilayer geometry the inspection of one specific layer can be done by inducing a much greater absorption coefficient on the others. A reduced scattering coefficients mismatch affects the statistics as well. In particular, when the reduced scattering coefficient of the first layer changes, the effect on $\langle z_{max} \rangle$ is large. For low values of the reduced scattering coefficient, $\langle z_{max} \rangle$ increases since photons are more likely to reach a greater depth. On the other hand, for high values of the reduced scattering coefficient, $\langle z_{max} \rangle$ decreases. Moreover, we found that the interfiber distance does not affect the mean maximum penetration depth as in the homogeneous case. Also simulations done varying s_1 and s_2 are very useful for the comprehension of the photon penetration depth in real cases in which thicknesses are not always fixed. Furthermore, a refractive index mismatch in the typical range for biological tissues does not change the statistics of photon penetration depth.

In CW the results are quite different from TD. The absorption coefficient significantly affects the statistics. In particular, the effect of a variation of μ_{a1} is greater than the effect of μ_{a2}. On the other hand, a variation of reduced scattering coefficients significantly influences photon penetration depth only in the case with an absorption coefficient different from zero. In the ideal case with μ_a=0 cm^{-1}, no significant differences are obtained. This means that interaction between absorption and scattering coefficients plays an important role in the statistics of photon penetration depth in CW domain. In the future it can be interesting to study in a more detailed way this interaction in both TD and CW domain.
Finally, a method similar to that developed in this thesis can be also applied to a multilayer geometry in order to better analyze biological media with more than two layers.

Bibliography Chapter 5

[1] S. R. Arridge and W. R. B. Lionheart, "Nonuniqueness in diffusion-based optical tomography", Opt. Lett., 23:882, (1998).

[2] R.F.Bonner, R.Nossal, S.Havlin, and G.H.Weiss, "Model for photon migration in turbid biological media,"J.Opt.Soc. Am. A 4, 423-432 (1987).

[3] F. Martelli, T. Binzoni, A. Pifferi, L. Spinelli, A. Farina, and A.Torricelli, "There's plenty of light at the bottom: statistics of photon penetration depth in random media", Scientific Reports 6:27057 (2016).

[4] R. Nossal et al., "Photon migration in layered media", J. Mod. Opt. 27, 3382–3391 (1988).

[5] F. Martelli, S. Del Bianco, A. Ismaelli, and G. Zaccanti, "Light Propagation through Biological Tissue and Other Diffusive Media: Theory, Solutions and Software", SPIE Press (2010), Chap. 3.

[6] Weiss, G. H., Nossal, R. & Bonner, R. F. Statistics of Penetration Depth of Photons Re-emitted from Irradiated Tissue. *J. Mod. Opt.* **36,** 349–359 (1989).